A Study on Coastal Winds and Wind Waves UsingHigh-Resolution SAR Images

著者	島田　照久
学位授与機関	Tohoku University
学位授与番号	2084
URL	http://hdl.handle.net/10097/45677

A Study on Coastal Winds and Wind Waves Using High-Resolution SAR Images

by

Teruhisa Shimada

Ocean Environment Group
Center for Atmospheric and Oceanic Studies
Graduate School of Science,
Tohoku University
Aoba-ku, Sendai, 980-8578, Japan

December 2003

Abstract

The coastal zone is formed by ether side of the coastline, i.e., the coastal land and the coastal sea. The majority of world's population is located in the coastal land region. As well as world population growth, the coastal population and their activities in the coastal zone increase, which accelerates wide spreading environmental stress to the world coastal seas. In order to ensure efficient and safe human activities and to preserve healthy marine environments in the coastal sea, sophisticated observing systems for the ocean environment monitoring are desired.

Surface winds are the most important parameter as a driving force of meteorological and oceanographic phenomena in the coastal zones. There exist some factors inherent in the coastal zone, which produce local variations of the coastal winds. These factors do not exist in the open oceans. The thermal contrast between the land and the sea creates the land-sea breeze. A lateral, orographic boundary can accelerate or block the wind flow. The surface wind crossing the coastline is modified by different surface roughness of land and sea.

In turn, the variable surface winds have direct impacts on oceanographic phenomena in the coastal sea. Generation and development of wind waves are controlled by the surface winds. They drive currents in the sea surface layer. Latent and sensible heat, and water vapor fluxes at the sea surface are forced by the surface winds. The surface wind observations are indispensable to study meteorology and oceanography in the coastal sea. In order to capture the coastal winds and to understand oceanic responses to them, high-resolution surface wind observations are necessary.

Synthetic Aperture Radar (SAR) will be an excellent candidate for filling the meteorological and oceanic observational gaps between the present systems and the above-mentioned needs in the coastal sea. SAR is an active microwave instrument which has an imaging capability of normalized radar cross section (NRCS) of earth surfaces with high-spatial resolution (< 30m). The SAR images can be converted into the high-resolution wind-speed maps by applying a geophysical model function (GMF), which relates the NRSC of sea surface and the surface vector wind. Because only SAR can provide high-resolution surface wind fields, it is considered that SAR-derived winds will give new understandings on the surface wind and oceanic phenomena in the coastal sea. The purposes of present study are to improve the SAR wind retrieval methods and, using them, to understand features of the coastal surface winds and to study effects of the

coastal winds on wind-wave development.

In Chapter 1, backgrounds, purposes of this study and structure of this thesis are described. We discuss roles of the SAR observation in understanding coastal winds and phenomena associated with the air-sea-land interaction.

In Chapter 2, datasets used in this study are summarized. Japanese Earth Resources Satellite-1 (JERS-1) SAR and European Remote sensing Satellite-1/2 (ERS-1/2) SAR are mainly used. Surface vector winds over land and sea observed by scatterometers and in situ wind measurements are used. Significant wave heights and wind speeds are obtained by satellite altimeters.

In Chapter 3, we examine relationships between L-band microwave backscattering at the sea surface and the surface wind speed and direction using JERS-1 SAR data, which results in the first L-band GMF. It enables us to retrieve high-resolution surface winds from the JERS-1 SAR images. We quantitatively evaluate two problems peculiar to JERS-1 SAR, which are the system noise in range direction and excessive ambiguities due to JERS-1 SAR operation troubles. It has been known that the ambiguity, which is inherent to radar systems, is especially large in the JERS-1 SAR images.

In the first half of this chapter, we develop the L-band GMF. It is found that the system noise has a feature common in all the SAR images and that the azimuth-averaged profile of noise can be expressed as a parabolic function of range. By subtracting the estimated noise from the SAR images, we obtain the relatively calibrated ocean signals. Next, using the noise-removed SAR data and surface vector wind data from NSCAT and buoys operated by Japan Meteorological Agency, we generate 7577 match-up data, which consists of the SAR NRCS, the SAR incidence angle, the surface wind speed and wind direction. A total of 2288 scenes of JERS-1 SAR in the open oceans are used because they are free from the ambiguity noise associated with coastal land signals. Then, we investigate the NRCS dependence on the incidence angle, the wind speed, and the wind direction. We cannot examine the incidence angle dependence because of narrow swath of JERS-1 SAR and the system noise in the range direction. For wind speeds below 8 m/s, the wind direction dependence is not significant. However, for higher wind speeds, the upwind-downwind asymmetry becomes very large, which are not seen in the Ku- and C-band GMFs. Finally, taking into account of these characteristics, we produce a new L-band GMF for the SAR wind retrieval using a third-order harmonics formula. Resultant estimates of the SAR-derived wind speed have a root mean square error of 2.09 m/s with a negligible bias against the truth wind speed.

In the latter half of this chapter, the surface wind retrieved from JERS-1 SAR using the L-band GMF in the coastal region is evaluated. We also used ERS-1 SAR images, which has no signifcant ambiguity noise. High-resolution wind-speed maps are derived from ERS-1 SAR images using the C-band GMF. First, focusing on the cases where wind blows from shore in Sagami Bay, we investigate relationships between wind speed and offshore distance along wind direction from the Hiratsuka Experiment Station (HES) using 41 scenes of ERS-1 SAR-derived wind fields. Consequently, the wind speed growth with offshore distance is well formulated as a function of the offshore distance and the wind speed at HES. This indicates development of the internal atmospheric boundary layer from over the land to over the sea. In contrast, JERS-1 SAR-derived wind speeds in the near-shore region are overestimated due to the excessive ambiguities. For observation time of each JERS-1 SAR scene capturing the case that wind blows from shore in Sagami Bay, the wind-speed profile along the wind direction is derived from the wind-speed growth formula and HES wind observation. Then, we convert the wind-speed profile into the NRCS profile by the L-band GMF. Finally, the profiles of JERS-1 SAR-observed and the estimated NRCSs are compared, and the excessive ambiguity is evaluated as the difference between them. As a result, the intensity of ambiguity within 20-km offshore distance is especially large. Moreover, higher order azimuth ambiguities and range ambiguity within 55-km offshore distance also may have a significant impact on the near-shore wind retrieval.

In Chapter 4, we present statistical features of the coastal winds using high-resolution SAR-derived wind speed maps.

We investigate the coastal wind-speed distribution in a Weibull parameter feature space. It has been known that the Weibull distributions give good fit to the distribution of wind-speed time series observed for a long time at land and open ocean stations. However, because we cannot obtain sufficient wind measurements at coastal stations, characteristics of the coastal sea surface winds are not known well. We used AMeDAS data for land surface winds, and in situ wind observations from three JMA buoys, a buoy in Mutsu Bay, and HES and QuikSCAT wind mearsurements for sea surface winds. For these data, we made year-around wind-speed distributions at the in situ stations and open-ocean grids, and obtained the Weibull parameters from the distributions.

A total of 6, 567 scenes of ERS-1/2 SAR around Japan are used. We average NRCS of

SAR images in every 1 × 1 km grid. Next, wind speed maps are derived from the 1-km grid NRCS by using the C-band GMF. In order to investigate statistical features of wind speed with the distance from the shore, the derived wind-speeds are resampled according to the offshore distance up to 100 km and assign them to the every 5-km bins perpendicular to the coast. The distribution of wind speed assigned to each bin is obtained for derivation of the Weibull parameters.

In the Weibull parameter feature space, the distributions in the coastal sea form a cluster different from clusters of land and open ocean. The distributions in the coastal sea have high frequencies in the lower wind-speed range and frequencies extending higher wind speeds. They can be reproduced by mixing the typical wind-speed distributions of land and open ocean at given rates.

Then, we investigate relationship between the standard deviation and skewness of SAR-derived wind speeds and the offshore distance. Subregions of 10-km square in the 1-km grid wind-speed map are used for calculation of the statistical parameters. Their wider distribution ranges are found in the near-coast seas and the ranges decrease with the offshore distance from the coast to 100 km offshore, which suggest that the offshore distance of 100 km can be a measure of a separation scale between the coastal sea and the open sea from the surface wind point of view.

In Chater 5, using high-resolution satellite observations, we present case studies to investigate surface winds and wind waves under the East Asian winter monsoon in the Pacific Ocean off Hokkaido and the Tohoku district. Under such conditions, steady strong winds blow from the Japanese archipelago to the Pacific Ocean and usually persist for periods longer than one day. Therefore, observation time differences among satellite sensors are unimportant to grasp representative views. Wind waves become dominant, and the fetch-limited, steady, and one-dimensional wind wave developments are satisfied.

The QuikSCAT surface wind vectors present wind jets and neighboring lower wind regions extending more than 600 km downwind from the Tsugaru Straits. The SAR-derived wind fields, which observe nearshore regions, reveal smaller-scale coasal jets and lower wind regions. The coastal wind jets extending from terrestrial gaps, i.e., Uchiura Bay and Mutsu Bay and the Tsugaru Straits are noticeable. The combind use of QuikSCAT and SAR allow us to capture the surface wind transition from the coastal region to the offshore ocean. Variations of significant wave height observed by T/P and ERS-2 altimeters are compared with wind speeds derived from QuikSCAT and SAR. As

a result, the positions of local maximum and minimum coincide with each other. This means that the wind waves are influenced by the orographically modified winds.

Chapter 6 summarizes the conclusions of this study.

The newly developed L-band GMF can be considered to contribute to development of the other L-band microwave sensors such as spaceborne and airborne SARs and oncoming sensors for sea surface salinity retrieval. It is found that the coastal high-resolution surface wind fields have smaller-scale two-dimensional structures, which is quite different from the surface winds over open ocean. This means that high-resolution observations are essential to capture the features of coastal surface winds. It is also shown that the coastal surface winds influence the offshore wind fields and the wind waves in the downstream open ocean. The accomplishments of present study may contribute to improvements of numerical model approaches for the surface winds, the wind waves and surface circulation in the coastal sea.

Contents

5 COASTAL WINDS AND WIND WAVES OBSERVED BY ACTIVE SATELLITE

1 Introduction

1.1 Global environmental problems and coastal monitoring

The majority of the polulation is located either directly along the coastlines or within the associated waterways, embayments, and estuaries. The more population is concentrated on such reigions. Today, there are over 5 billion people on earth, and about 38% of them live in the coastal zones within 100 km of the coastline at elevations less than 100 m [Small and Nicholls, 2003]. This is shown in Figure 1.1 from the viewpoint of global distributions of population density and city lights. They are cited from Small and Nicholls [2003]. Gridded population densities (Figure 1.1(a)) provide estimates of the spatial distribution of population while city lights (Figure 1.1(b)) provide higher resolution estimates of the spatial distribution of population centers and socioeconomic activity. Note that lighted settlements are heavily concentrated within 5 km of coastlines worldwide (Figure 1.1(a)).

An increasing number of people and their activities present the potential for widespread environmental stress to coastal zones. Coastal systems must fullfil more demands for supporting commerce, living resources, recreation, and living space and for receiving, processing, and diluting the effluents of human society. Expected sea-level rise due to the climate change is a critical problem for the coastal zone. The land-based pollutions are serious problems in the global coastal seas, e.g, increasing red-tide events, contaminants in sea foods, degradation of sea water quality. Natural hazards damage coastal environment. In order to cope with these problems, coastal environmental monitoring takes on a growing importance. Above all, the high-resolution ovserving systems of marine parameters are desired to improve the nowcast and forecast capability of oceanic phemomena in the coastal sea.

1.2 Air-Sea-Land Interaction and surface winds

Understanding the meteorology and physical oceanography in the coastal zones combines knowledge of the interaction of marine and land atmospheric boundary layers, air-sea interaction, large-scale atmospheric dynamics, and the circulation of the coastal ocean. The coastal zones are defined as extending areas to either side of the coastaline. Most coastal environments are modified by the adjacent ocean, the coastal topography and the land-sea thermal contrast. Complex feedbacks occur between the atmosphere, ocean and land. The thermal contrast between the land and sea creates the land-sea breeze and coastal atmospheric fronts. The convergence of marine air over the coastline can result in strong convection with heavy precipitation and runoff. A lateral, orographic boundary can accelerate or block the wind flow. Variations in the speed and direction of the wind depend on the exact nature of the orographic boundary. This results in highly variable temporal and spatial air-sea exchange processes that are dominated by scales of tens to hundreds of kilometers. A disciplinary of dealing with those described above falls into coastal meteorology [e.g., Hsu, 1988].

From a viewpoint of sea states and upper-layer ocean circulation in coastal seas, surface wind field is the most important factors. As mentioned above, the coastal surface winds are affected by the result of the land/sea contrasts in heating, orographic forcing, and surface friction. The resulting surface wind fields are categolozed into several types according to their thermo-dynamical formation mechanisms. The typical winds are summarized in Table 1.1. In turn, the winds have an impact on coastal seas. The wind stress at the surface generates and develops wind waves and turbulence in the surface layer. Associated heat fluxes drive the ocean circulation. For example, sea surface cooling causes thermal convection in the surface mixing layer of ocean. Accumulating wind forcing results in the wind-driven currents, which is affected by the Coriori force to be the Ekman flow. The coastline and bottom topography play important roles to generate coastal trapped phemomena and to decay them through the friction effects. A schematic picture of the coastal winds and the resulting phenomena aimed at in the present study is illustrated in Figure 1.2.

1.3 Synthetic Aperture Radar for air-sea-land interaction in coastal seas

1.3.1 Satellite remote sensing for ocean observations

Over the last decades, satellite remote sensing has proved to be a valuable tool for monitoring physical and biological ocean processes. It plays an increasingly important and indispensable role in the study even in the coastal zone because of rapid technological changes. In general, spatial resolutions of the space-based remote sensing sensors become finer. Temporal coverage is complement with wider sensor swaths and multi-sensors on satellites in the geostationary and polar orbits. Sensors with better precision and new functions are being developed and planned. Some missions are transitive to continual operations. The cost of satellite observation becomes cheaper. They enable us to monitoring coastal environment.

As well as the high-resolution capabilities of satellite sensors, usefulness of the synergetic utilization of multi-sensor has been emphasized through a number of experiments [e.g., Ufermann et al., 2001]. The satellite imagery has led researchers to new knowledge in oceanography and marine meteorology when used in combination with in situ data and numerical atmosphere/ocean models. Nowadays, we have reached the stage of studying and monitoring the coastal environment using longstanding satellite datasets with sufficient resolution.

As for observations of sea surface winds, microwave scatterometers have greatly contributed to weather and ocean-atmosphere interaction. Scatterometers are the only proven instruments that give us measurements of cean surface wind vectors. Progress in the scientific application of scatterometer is reviewed in Liu [2002]. Admitting that high-resolution (12.5 km) products are developed, it is still too coarse to resolve coastal wind variations. In the coastal seas, it is essential to resolve surface winds with high spatial resolution, as mentioned in Section 1.2. Therefore, comprehensive pictures of wind transitions and variations in the coastal zones have remained to be solved.

Especially, for coastal environmental monitoring, Synthetic Aperture Radar (SAR) will be an excellent candidate for filling the meteorological and oceanic observing needs over coastal seas. SAR is an active microwave instrument which has an imaging capability of the normalized radar cross section (NRCS) with quite a high spatial resolution. It is a side looking system measuring the slant range to the target. The main process of SAR imaging is a two-dimensional (i.e., range and azimuth directon) correlation of the SAR raw data with a refernce function [Henderson and Lewis, 1998]. SAR coordinate systems are shown in Figure 1.3.

Spaceborne SARs have been continuously operated for a long time since 1990 and their imagery has been distributed to researchers for basic studies and application developments. System parameters for main spaceborne civilian Earth observing SAR missions are summarized in Table 1.2. Especially, ERS-1/2 SAR and JERS-1 SAR had operated long time and acquired a great deal of images of the Earth surface. While most spaceborne SARs are single parameter sustems, recent SARs which have several operation modes such as high resolution, polarimetry, and scan mode have been operated and planned. Now SAR is one of the satellite sensors which play key roles in earth observations.

The high-resolution capability of SAR can resolve many meteorological and oceanic phenomena in the vicinity of sea surface, which can not be extracted from other remote sensing data. Oceanic phenomena that can be delineated on SAR images of the sea surface include ocean surface waves [e.g., Hasselmann and Hasselmann, 1991], internal waves [e.g., Alpers, 1985], eddies [e.g., DiGiacomo and Holt, 2001], oceanic fronts [e.g., Johannessen et al, 1996], underwater bottom topography [e.g., Alpers and Hennings, 1984], ship wakes [e.g., Lyden et al., 1988], oceanic and atmospheric wakes behind islands [e.g., Barton et al., 2000], oil slicks [e.g.,Lu, 2003], river plumes [e.g., Hessner and Rubino, 2001] and upwelling areas [e.g., Clemente-Colòn and Yan, 1999]; atmospheric phenomena include katabatic wind fields[e.g., Alpers et al.,1998], land-sea breeze, gap winds[e.g., Sandvik and Furevik, 2002], boundary layer rolls [e.g., Alpers and Brümmer, 1994], convective cells [e.g., Sikora et al., 1997], atmospheric gravity (or internal) waves[e.g., Vachon et al.,1994], vortex streets [e.g., Li et al., 2000], tropical storms [e.g., Li et al., 2002] and rain cells [e.g., Melsheimer et al., 1998].

1.3.2 SAR high-resolution wind retrieval

Recent improvements on the radar backscattering at the sea surface enable us to retrieve high-resolution wind-speed maps from the SAR images. They meet the demand of wind observations with high-spatial resolution.

NRCS at the sea surface is considered to relate with the radar frequency and polarization, incidence angle, surface wind speed and direction, and other geophysical parameters such as stability, SST, and sea states. Main modulator of sea surface roughness is the local wind. Changes in wind velocity cause changes in ocean surface roughness through the high-frequency components of wind wave. In turn, NRCS of the ocean is modified.

NRCS at the sea surface is usually prameterized as this:

$$\sigma^0 = \sigma^0(f, p, \theta, U, \phi) \tag{1.1}$$

where f and p are the frequency and polarization of the microwave, respectively. θ is the incidence angle, U is the wind speed, and ϕ is the relative wind direction defined as the angle between the radar looking direction (projected onto the horizontal plane) and the wind direction. To determine the dependecy of the radar returns on the relative wind direction, the harmonic formula for the cosine function is applied [Moore et al., 1978].

$$\sigma^0(f, p, \theta, U, \phi) = \sum_{n=0} A_n(f, p, \theta, U)\cos(n\phi) \tag{1.2}$$

This relationship is represented as a geophysical model function (GMF), which empirically and/or theoretically relates the scatterometer or SAR-derived NRCS with the radar frequency and polarization, incidence angle, wind speed and direction, and other parameters of the sea surface, is utilized in the wind retrieval. The inversion algorithm to convert the NRCS to wind speed is called SAR wind retieval.

In order to retrieve surface wind fields from SAR imagery, three conditions have to be satisfied. First, each pixel value of the SAR imagery, which is equivalent to NRCS, must be calibrated absolutely or relatively for wind-retrieval. Second, a GMF has to be established for the SAR microwave band. Third, we need to specify the wind direction through the other data sources because SAR has only one-look direction. In other words, the SAR provides only the wind speed with very high spatial resolution (10~100 m). Previous studies on the SAR wind retrieval have used the wind directions from satellite scatterometers, in situ ship/buoy measurements, and operational/non-operational meteorological model outputs.

1.3.3 C-band SAR wind retieval

At the present, C-band SARs of ERS-1/2 and RADARSAT have been most commonly used for SAR wind retrieval. Several C-band model functions have been established for ERS scatterometer [e.g., Stoffelen and Anderson, 1994; Quilfen et al., 1998]. They relate VV-pol NRCS with incidence angle, wind speed and wind direction. Some model functions are well validated and in operational use for scatterometer products. Many studies have revealed the efficiency of SAR-derived wind fields for interpreting various atmospheric and oceanic phenomena. Nowadays, ENVISAT SAR also becomes available to wind relating applicaitions. On the other hand, RADARSAT observes HH-pol NRCS. To use well-validated VV-pol model function, a porlarizarion ratio is developed by Thompson and Beal [2000]. The poralaization ration is a function of incidence angle and the paramter alpha.

For a discussion of the accuracy of wind retrieval from SAR images using the C-band scatterometer model funcitons, we can refer to the following papers. Validations of SAR wind retieval using CMOD4 and CMOD5 in [Vachon and Dobson, 1996] represente a wind speed extraction error of 1.5 m/s for the 3 to 12 m/s wind speed conditions. The improved calibration scheme is considered in Scoon et al. [1996]. A validation of SAR wind retieval is performed by comparing wind scatterometer of ERS during ERS tandem phase by Furevik and Korsbaken [2000]. In Monaldo et al. [2001], using a wide-swath RADARSAT SAR imagery, SAR-derived wind speeds are compared with model predictions and buoy measurement. It shows very good agreement, and the standard deviation is 1.76 m/s.

Some studies make an attempt to retrieve optimal wind direction as well as wind speed from SAR. Wackerman et al. [1996] developed an automated algorithm intended for estimateing wind speed and direction using ERS-1 SAR imagery. Portabella et al. [2002] investigated optimal inversion method for SAR wind retrieval. Fichaux and Ranchin [2002] developed a combined wind parameters extraction algorithm at a high spatial resolution from a single SAR image.

1.3.4 Coastal winds investigated by SAR-derived wind fields

SAR-derived wind fields have been verifed to contribute to understanding the wind speed modulation associated with various phenomena: atmodpheric lee waves [Vachon et al., 1994], atmospheric boundary layer rolls [Alpers and Brümmer, 1994; Müller and Brümmer, 1999], atmospheric gravity waves [Vachon et al., 1994], atmospheric nonlinear wave disturbance [Alpers and Stilke, 1996], Coastal lee waves [Zheng et al., 1998], Katabatic wind [Alpers et al. 1998], mesoscale wind fields [Lehner et al. 1998; Korsbakken et al., 1998], and a mesoscale coastal jet [Sandvik and Furevik, 2002] (See also Table 1.1).

A series of studies of SAR wind retieval has revealed a variety of coatal wind distributions. They show that coastal winds can vary with surprisingly smaller scale and have unexpectedly significant gradient. It is difficult to infer such wind variations in coastal zones from ship and scatterometer wind measurements. It is natural that coastal wind variations should be reflected by surface wave, SST, currents. In order to understand coastal environment, it is essential to investigate smaller-scale and drastic wind variations.

1.4 Scope of the present study

On the basis of considerations summarized above, our approach is designed with focus attention on the followings. First, we develop L-band GMF and establish L-band SAR wind retrieval. While C-band SAR wind retieval have now become a proven technorogy for research of the coastal wind fields and their involving phenomena, no L-band GMF exists for the surface wind retrieval. Next, we approach understanding of coastal winds from statistical point of view. As reviewed in Section 1.3.4, many studies has been carried out and verified that the SAR high-resolution wind maps have high research potential. Howerver, almost all of them are case studies. In that case, it can be hardly said that SAR is effectively utilized for monitoring the coastal wind field. Then, we promote synergetic use of the SAR observations and the other satellite datasets. In paticular, we clarify the actual variation of coastal wind using high-resolution SAR wind fields in combintion with the scatterometer surface vector winds and the altimeter wind speed and wave height.

This thesis is organized as follows. The datasets used in the present study are summarized in the following chapter. In Chapter 3, we study on L-band SAR wind retrieval using JERS-1 SAR. We first describe the developmet of an L-band GMF. Then, we validated the JERS-1 SAR-derived wind speeds and evaluated excessive ambiguities of JERS-1 SAR using the L-band GMF. In Chapter 4, we present statistics of surface wind speed distributions on land and sea, and characterize coastal winds by comparing them with winds over land and open ocean. In Chapter 5, we investigate evolution of the surface wind field from the coast to the offshore by a combined use of scatterometer and SAR. Then, we examine relationships between surface winds and wind waves under the fetch-limited condions using altimeter wave height observations. Chapter 6 summarizes the present study.

Table 1.1 List of main local winds and their studies. SAR is used in the references indicated with asterisk.

Local winds	Explanation	Reference
Downslope winds	Flow directed down a mountain slope and driven by cooling at the earth's surface: a component of the mountainvalley or mountainplains wind systems; same as katabatic wind.	Smith, 1987; Alpers et al.,1998*
Land/sea breeze	A coastal local wind that blows from sea to land, caused by the temperature difference when the sea surface is colder than the adjacent land.	Rotunno,1983
Gap winds	A strong, low-level wind through either a relatively level channel between two mountain ranges or a gap in a mountain barrier	Overland, 1984; Chelton et al.,2000a and 2000b; Sandvik and Furevik, 2002*
Wakes	The region of turbulence immediately to the rear of a solid body in motion relative to a fluid	Smith and Grubisic, 1993; Barton et al.,2000*
Barrier jets	A jet on the windward side of a mountain barrier, blowing parallel to the barrier. The jet is produced when stable synoptic flow at low levels approaches the barrier and is blocked for a significant fraction of a day or longer.	Pierrehumbert, 1984; Laing and Brenstrum,1996
Atmospheric internal boundary layer	The bottom layer of the troposphere that is in contact with the surface of the earth. It is often turbulent and is capped by a statically stable layer of air or temperature inversion.	Etling and Brown, 1993; Alpers and Brümmer,1994*
Internal boundary layer	The air that is modified by flow over a different surface heat flux and roughness surface.	Present study

Table 1.2. Main spaceborne SAR systems (1978-2004).

	Seasat	SIR-A	SIR-B	ALMAZ	ERS-1	JERS-1	SIR-C/X-SAR	ERS-2	RADARSAT	ENVISAT	PALSAR	RADARSAT2
Country	USA	USA	USA	USSR/Russia	Europe	Japan	USA,Germany and Italy	Europe	Canada	Europe	Japan	Canada
Agency	NASA	NASA	NASA	Glavkosmos	ESA	MITI/NASDA	NASA/DLR/DARA	ESA	CSA/USA	ESA	JAXA/JAROS	CSA/MDA
Spacecraft	Seasat	Shuttle	Shuttle	Salyyut	ERS-1	JERS-1	Shuttle	ERS-2	RADARSAT	ENVISAT	ALOS	RADARSAT2
Launch date	26.Jun.78	12.Nov.81	5.Oct.84	31.May.91	16.Jun.91	11.Feb.92	Apr'94,Oct '94	1995	Nov '95	1.Mar.02	2004	late 2005
Lifetme	3mos	2.5day	8days	1.5years	5years	6.5years	10days			5years		7years
Band[wavelength(cm)]	L[23.5]	L[23.5]	L[23.5]	S[10]	C[5.7]	L[23.5]	L,C;X	C[5.7]	C[5.7]	C[5.7]	L[23.5]	C[5.7]
Frequency(GHZ)	1.275	1.278	1.282	3.0	5.25	1.275	1.25,5.3,9.6	5.3	5.3	5.3	1.275	5.3
Polarization	HH	HH	HH	HH	VV	HH	quad-pol(L,C),VV(X)	VV	HH	VV+HH	quad-pol	quad-pol
Incidence angle(degrees)	23	50	15-64	30-60	23	39	15-55	23	20-50	20-50	8-60	20-50
Range resolution	25	40	25	15-30	26	18	10-30	26	10-100	~25	10-100	10-100
Azimuth reslution	25	40	58-17	15	28	18	30	28	9-100	~25	10-100	10-100
Looks	4	6	4	>4	6	3	4	6	1-8	~4	4	1-8
Swath width	100	50	10-60	20-45	100	75	15-60	100	10-500	100(500)	20-350	50-500

(a) **Population Density**

(b) **City Lights**

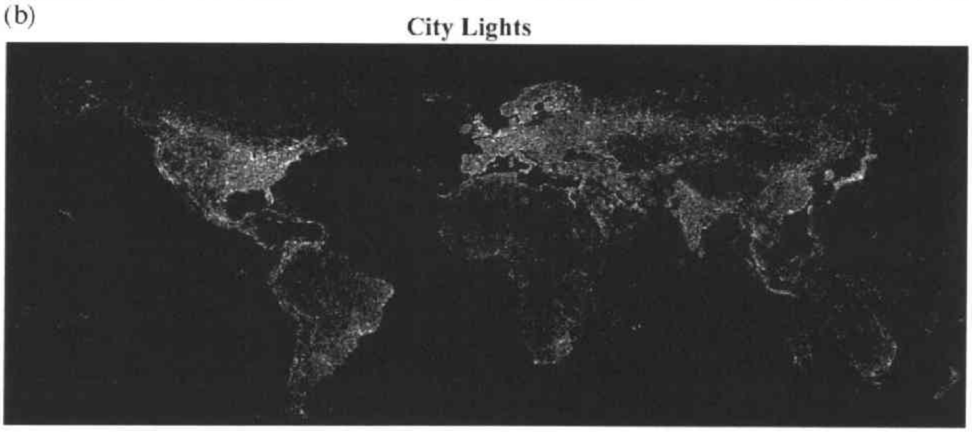

Figure 1.1 Global distributions of (a) population density and (b) city lights. Figures are cited from Small and Nicholls [2000]. 1990 population density, derived from the GPW2 census compilation, ranges from 1 person/sq.km (dark) to 1000 people/sq.km (white) on a logarithmic scale. Temporally stable lights (white) are derived from DMSP/OLS night time satellite imagery collected in 1994-1995.

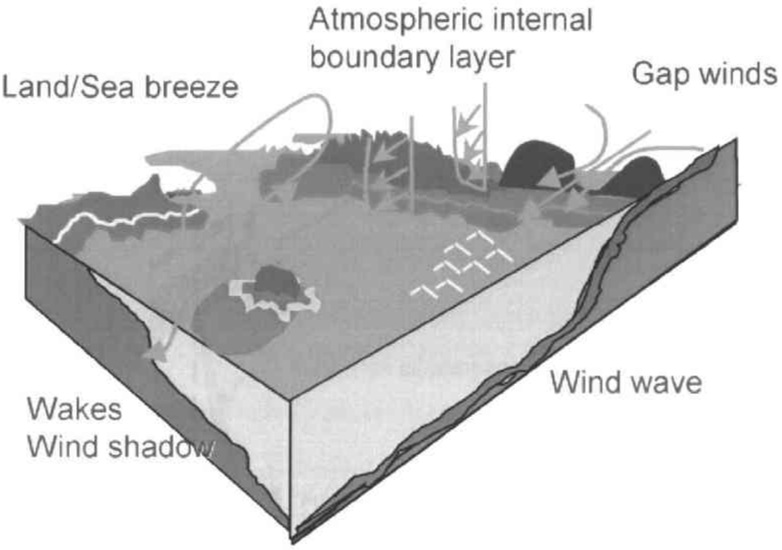

Figure 1.2 A schematic picture of modified coastal winds and the resulting phenomena in coastal seas. Blue arrows indicate scheme of wind streamlines.

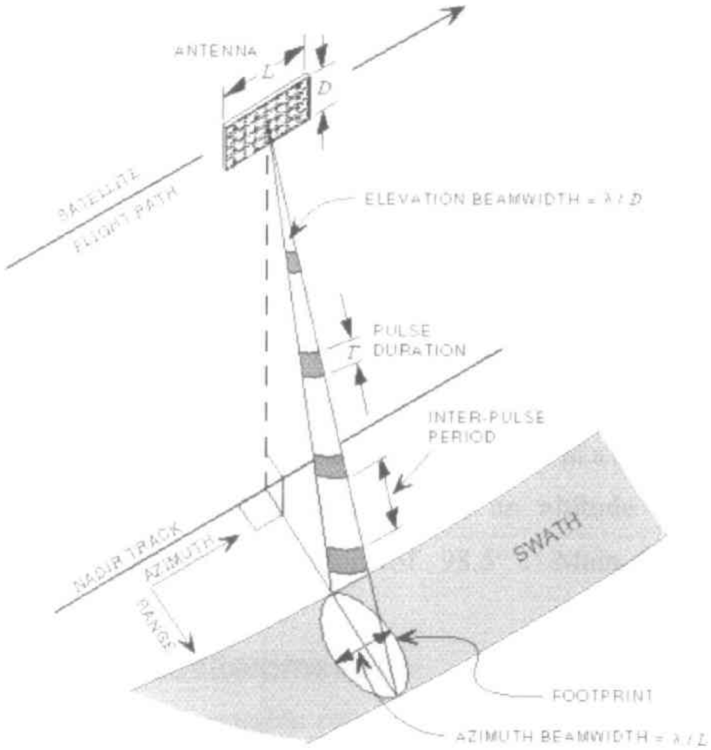

Figure 1.3 SAR coordinate systems. The figure is cited from http://www.cs.uaf.edu/public/rgps/reports/rsg_RGPSview_doc/1.html.

2 Data

In this chapter, descriptions of datasets utilized in the present study are given. They contain satellite datasets, in situ measurements, and reanalysis data. They are individually summarized in Table 2.1.

2.1 Satellite datasets

2.1.1 Systhetic Aperture Radar

JERS-1 was launched into a solar-synchronous sub-recurrent orbit at an altitude of 568 km with a recurrent period of 44 days on February 11, 1992 from NASDA (National Space Development Agency of Japan). An L-band and HH polarization SAR on board JERS-1 featured a high resolution of 18 m, a fixed off nadir angle of 35° and an imaging width of 75 km. Main characteristics are summarized in Table 2.2.

ERS-1/2, carrying AMI (Active Microwave Instruments), had been in operation since July 17, 1991 and April 21, 1995, respectively. The AMI has a function as C-band (5.3 GHz) SAR with VV-polarization, so called "image mode". The SARs aboard the two satellites have identical design. They operate over a fixed range of incidence angles of 20 – 27°, which results in the imaging width of 100 km. The nominal spatial resolution of the imagery is 30 m. The satellite has three modes of operation in a recurrent period of 35 days as standard, 3 days, and 176 days flying at an altitude of 780 km in a solar-synchronous orbit with an inclination of 98.5° . Main characteristics are summarized in Table 2.3.

2.1.2 Microwave scatterometers

Table 2.4 summarizes main comparable characteristics of scatterometers used in the present study. The Advanced Earth observing Satellite (ADEOS) was launched on August 17, 1996 and carried eight sensors including NSCAT until June 30, 1997. NSCAT is a dual-swath, Ku-band (13.995 GHz) scatterometer, which can measure vector winds over a swath of 600 km with a spatial resolution of 50/25 km. The NSCAT Ocean Data product used in this study is 25 km Selected Wind Vector (SWV). It contains the surface wind vectors selected along the satellite track with a spatial resolution of 25 km and flags.

The SeaWinds instrument on the QuikSCAT satellite, which is launched by NASA on June 19,1999, is a specialized radar that measures near-surface wind speed and direction at a 25-km resolution. SeaWinds uses a rotating dish antenna with two spot beams that sweep in a circular pattern. The antenna radiates microwave pulses at a frequency of 13.4 GHz across broad regions on Earth's surface. The instrument will collect data over ocean, land, and ice in a continuous, 1,800-kilometer-wide band, making approximately 400,000 measurements and covering 90% of Earth's surface in one day. SeaWinds data is obtained from NASA Physical Oceanography Deistributed Active Archive Center (PODAAC) at the Jet Propulsion Laboratory (JPL). In the present study, L2B puroduct is used.

2.1.3 Microwave altimeters

Table 2.5 summarizes main comparable characteristics of altimeters used in the present study. Topex/Poseidon is a joint NASA-CNES satellite altimeter, which has been operating since September 1992. It is the most accurate altimeter system yet flown with an absolute accuracy of about 4 cm. Significant wave height is retrieved from the leading edge slope of the altimeter waveform. The altimeter significant wave height has precision as buoys (~0.3 m). Its repeat period is 9.916 days, i.e.; the satellite passes over the same location, to within 1km, every ten days. We use the TOPEX/POSEIDON MGDR (Merged Geophysical Data Record), which contains global coverage altimeter data.

Radar altimeters on board ERS-1/2 are a Ku-band (13.8 GHz) nadir pointing active microwave sensor providing, along the satellite track, measurements of the echoes from ocean surface, from which wind speed, wave height and sea surface elevation can be retrieved using precision orbits derived from the onboard laser retro-reflector. We used ERS OPR, which provides swath data sets from the ERS radar altimeter.

2.2 In situ observation data

2.2.1 AMeDAS

JMA (Japan Meteorological Agency) routinely accumulated data from approximately 1,300 automatic observation facilities, called AMeDAS (Automated Meteorological Data Acquisition System). They are located at intervals of about 17 km around the nation to monitor precipitation. About eight hundred and forty stations at intervals of about 21 km observe all of the four key parameters: air temperature, wind direction and speed, precipitation and sunshine duration. Furthermore, automatic snow gauges are located in areas with heavy snowfall to monitor snow depth.

2.2.2 JMA buoys

JMA operated three Ocean Data Buoy Stations (WMO buoy nos., 21002, 21004, 22001) in the seas around Japan. Figure 2.1 shows their locations. They measure 11 meteorological and oceanic variables including wind direction and speed. In order to make the buoy winds compatible with the nutral equivalent 10-m height wind derived from scatterometers, the buoy wind speeds measured at 7.5 m above sea surface are converted to the 10-m equivalent neutral wind speed by a method proposed by Liu et al. [1979].

2.2.3 Hiratsuka Experiment Station

Since 1965, sea-surface wind vectors and surface waves have been continuously measured at the Hiratsuka Experiment station (hereafter, the Hiratsuka tower) operated by the NRIESDP of the Science and Technology Agency, Japan. The Hiratsuka tower is located 1 km offshore (See Figure 2.2(b)) at a water depth of 20 m. An anemometer is installed on the tower at 19.5 m height above the mean sea surface. Winds and waves are recorded with a sampling interval of 0.3 s. Wind data are recorded hourly as a mean over a period of 10 minutes. The systems and climatological analyses are summarized by Watabe et al. [1996 and 1997].

2.2.4 A buoy in Mutsu bay

A mooring buoy located in the centeral area of Mutsu Bay (Figure 2.2(c)) is operated by Aomori Prefetural Aquaculture Research Center and continuously observes the wind direction and speed at 4 m height every hour. Mearsuring resolutions of the buoy wind direction and speed are 1 degree and 0.1 m/s, respectively.

2.3 Reanalysis data

Surface reanalyses from NCEP/NCAR reanalysis project are used. It is using a state-of-the-art analysis/forecast system to perform data assimilation using past data from 1948 to the present. The 10 m-height wind data are used from surface flux dataset. The dataset covers the area of 88.542°N - 88.542°S, 0°E - 358.125°E with T62 Gaussian grid. It has 192 and 94 points in zonal and meridional directions. Outputs are given every 6 hours.

Table 2.1 (a) Satellite active sensors, (b) in situ measurements, and (c) reanalysis datasets used in the following chapters of the present study.

(a)

	Satellite	Sensor	Microwave Frequency	Retrieved Parameters	Chapter in the present study
SAR	JERS-1	SAR	L-band [1.27GHz]	Surface wind speed	3
	ERS-1/2	AMI	C-band [5.3GHz]	Surface wind speed	4,5
Microwave Scatterometer	ADEOS	NSCAT	Ku-band [13.995GHz]	Surface wind vector	3
	QuikSCAT	SeaWinds	Ku-band [13.4GHz]	Surface wind vector	4,5
Microwave Altimeter	ERS-2	RA	Ku-band [13.8GHz]	Significant wave height and wind speed	5
	Topex/Poseidon	Altimeter	C- and Ku-band [5.3 and 13.6 GHz]	Significant wave height and wind speed	5

(b)

	Systems	Parameters	Chapter in the present study
In situ measurements	JMA buoys	Surface wind vector	3,4
	AMeDAS	Surface wind vector	4,5
	Hiratuska Experiment Station	Surface wind vector	3,4
	Mutsu Buoy	Surface wind vector	4,5

(c)

	Dataset	Parameters	Chapter in the present study
Reanalysis data	NCEP/NCAR	Surface wind vector	4,5

Table 2.2 Main characteristics of JERS-1 SAR.

Country	Japan	
Agency	MITI/NASDA	
Spacecraft	JERS-1	
Launch site	Tanegashima Space Center,Kagoshima,Japan	
Launch date	February 11,1992	
Lifetime(design)	2 years	
End date	October 12,1998	
Orbit	Type	Sun synchronous sub-recurrent orbit
	Altitude	568km
	Inclination	97.7deg.
	Period	96min.
	Recurrent period	44days
	Local time at Descending node	A.M.10:30-11:00
	Operation time per orbit (min)	20
	Down-link data rate(MB/sec)	30(*2)
Recorder on board?	Y	
Processing	Digital	
Swath width	75km	
Range resolution	18m	
Azimuth resolusion	18m	
Looks	3,4	
Off nadir angle	35.2deg.	
Incidence angle	39deg.	
Observation frequency	1275MHz(L-band)	
Polarization	HH	
Antenna	flat	
Size(m)legth*height	11.9*2.4	
Noise equivalent NRCS(dB)	-14.5	

Table 2.3 Main characteristics of ERS-1/2 SAR.

Country	Europe	
Agency	ESA	
Spacecraft	ERS-1/2	
Launch date	16 July 1991 and 20 April 1995	
End date	31 August 1996 and the present	
Orbit	Type	Sun synchronous sub-recurrent orbit
	Altitude	780 km
	Inclination	98.5deg.
	Recurrent period	3,35,176 days
	Local time at Descending node	A.M.10:30-11:00
Swath width	100 km	
Range resolution	26 m	
Azimuth resolusion	28 m	
Incidence angle	23 deg.	
Observation frequency	5.7 GHz(C-band)	
Polarization	VV	
Noise equivalent NRCS(dB)	-24	

Table 2.4 Main characteristics of ADEOS/NSCAT and QuikSCAT/SeaWinds.

	NSCAT	SeaWinds
Launch date	August 17, 1996-June 30, 1997	June 19, 1999-
Organaization	NASA	NASA
Satellite	ADEOS	Quikscat
Mission term	August 17, 1996-June 30, 1997	June 19, 1999-
Orbit	near-polar Sun-synchronous orbit	near-polar Sun-synchronous orbit
Frequency	Ku-band(13.995 GHz)	Ku-band(13.4 GHz)
Swath width(km)	600*2	1800
Resolution(km)	50, 25	25
Scan Characteristics	two sided, double swath	a rotating dish antenna with two spot beams that sweep in a circular pattern.
Product	NSCAT 25km SWV	QuikSCAT Science Data Procucts (Level 2B)

Table 2.5 Main characteristics of Topex/Poseidon and ERS-2 Radar Altimeter.

	Topex/Poseidon	ERS-2 Radar Altimeter
Launch date	10 August 1992	20 April 1995
Organaization	NASA/CNES	ESA
Satellite	Topex/Poseidon	ERS-2
Sensors	NRA, SSALT, TMR, LRA, Doris, GPSDR	Laser, PRARE
Frequency	Ku- and C-band (13.6 and 5.3 GHz)[Topex], Ku- band(13.65 GHz)[Poseidon]	Ku-band(13.4 GHz)
Height (km)	1,336	780
Inclination (deg.)	66.039	98.5
Repeat cycle(day)	9.9156	3,35

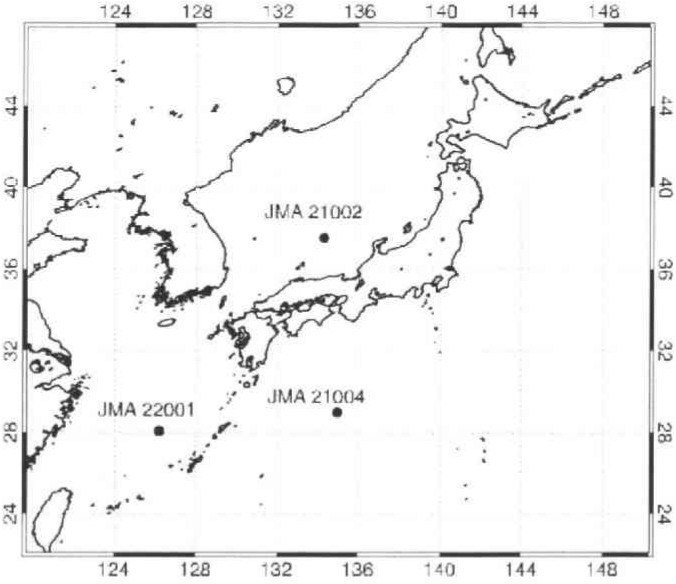

Figure 2.1 The locations of JMA buoys (WMO buoy nos., 21002, 21004, and 22001), indicated with closed circles.

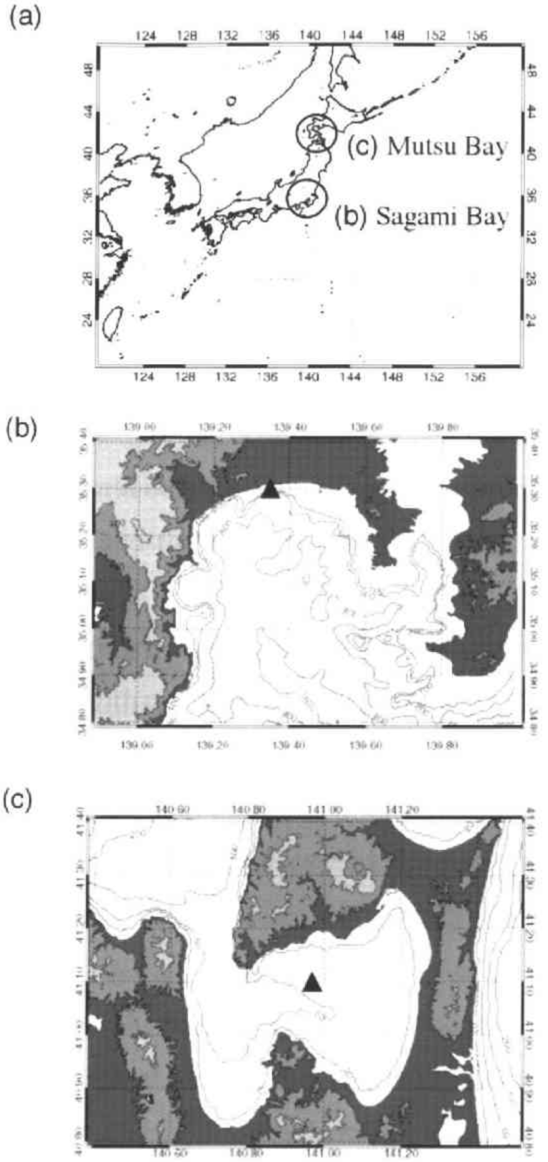

Figure 2.2 (a) Locations of (b) Sagami Bay and (c) Mutsu Bay. (b) Hiratsuka Experiment Station in Sagami Bay and (c) a buoy with anemometer in Mutsu Bay are shown by triangles. Hiratsuka Experiment Station is located 1 km offshore form the coast, and the buoy in Mutsu Bay is located at the center of the bay. Surrounding elevations and bathymetry are also shown.

3 Wind retrieval using L-band SAR of JERS-1 and its validation in the coastal seas

3.1 Introduction

Retrieval of sea surface wind speed from the SAR images has been a focus of study in the SAR research commumity for the past ten years. Contrary to many applications of C-band SAR wind retrieval from ERS-1/2 and RADARSAT, however, JERS-1 SAR data has not been used for the wind retrieval due to a lack of L-band model function.

Characteristics of L-band backscattering at the sea surface are not well understood for wide ranges of the parameters, and the relationship between L-band backscattering and wind vector is not represented as an L-band GMF. Several studies suggested that NRCS of L-band depends on both the wind speed and the wind direction [Guinard et al., 1971; Weissman et al., 1979; Keller et al., 1990]. Researches using the SEASAT SAR pointed out that an L-band SAR image could be transferred into a high-resolution wind map using the relationship between NRCS and the wind vector [Thompson et al., 1981; Gerling, 1986]. These studies are summarized in Table 3.1.

Moreover, JERS-1 SAR operation troubles prevent the applications of its ocean images. JERS-1 SAR has been operated with reduced transmitted power (325 W nominal] instead of the normal transmitted power (1300 W nominal) since September 18, 1992 in order to cope with the degradation of the azimuth antenna pattern. Hence, the sensitivity is 6 dB smaller than the original design, which has degraded the noise equivalent sigma-0 to -14.5 dB. Due to the lower S/N ratio, it is possible that the range of fluctuation of speckle noise exceeds the lower signal level. In terms of the sensor calibration, it is difficult to subtract the system noise from SAR data to prevent the received power from seeming negative. Because the noise influence on the SAR image of ocean is not negligible, we cannot consider the digital pixel values of the whole image as calibrated backscatter.

This also brings about ambiguity problem in the coastal zones of JERS-1 SAR images. It is known that there exist excessive ambiguities in JERS-1 SAR images. However, little attention has been given to the point and the qualitative evaluations of excessive ambiguities on JERS-1 SAR images are not understood exactly. So, the effects of excessive ambiguities on wind retrieval in coastal zones are also unknown.

In this chapter, we propose an L-band model function for wind retrieval from the JERS-1 SAR images, and validated the retrived surface winds. In Section 3.2, we develop the L-band geophysical model function using the JERS-1 SAR images in the open oceans.

In Section 3.3, we show evaluation of the JERS-1 SAR images and the retrieved wind speeds in the coastal zones. Discussion is devoted in Section 3.4. Summary is given in Section 3.5.

3.2 An L-band geophysical model function for SAR wind retrieval using JERS-1 SAR

3.2.1 Remarkable approaches

In order to investigate L-band backscattering characteristics, JERS-1 SAR, NSCAT on board ADEOS-I and in situ observations from the moored buoys of JMA (see Figure 2.1) are used. Surface wind vectors of the NSCAT and the JMA buoys are used as sea truth data. A unique point of the study is usage of the NSCAT vector winds for characterization of the JERS-1 SAR signals. Both ADEOS and JERS-1 had sun-synchronous orbits, whose orbital factors are close to each other. Moreover the local times at descending node of the two satellites are around 10:30 a.m. Therefore, if the observation swath of NSCAT completely or partially contain that of JERS-1 SAR and the observation times are close, many series of coincident and collocated observations along the swath path are obtained. In such a case, temporal difference between observations by two sensors is less than 30 min.

We collected 2288 scenes of its observations, which cover the seas around Japan, i.e. the Japan Sea, the East China Sea and the northwestern North Pacific Ocean. They are made up of 2101 scenes with corresponding the NSCAT observations and 187 with corresponding JMA buoy observations. Figure 3.1 shows coverage of JERS-1 SAR observations utilized in this study. Most of the JERS-1 images used in the study captured the area of the open ocean, and all the match-ups are generated in offshore regions because the corresponding NSCAT wind vectors can not be retrieved in the near-shore seas. Therefore, influence of the coastal seas on the radar backscattering, such as effects of depth fluctuations, currents, slicks and fetch on the surface waves, may not be serious. Raw SAR data is processed by the Sigma SAR Processor [Shimada, 1999] to generate slant-range images for the analysis of the present study.

3.2.2 System noise of JERS-1 SAR

Because it is quite difficult to derive absolutely calibrated NRCS of the ocean from the original JERS-1 SAR data due to the system noise, we carried out a relative calibration of the JERS-1 SAR signals for wind retrieval.

The slant-range image of JERS-1 SAR originally has 5888 pixels in the range direction and 5120 pixels in the azimuth direction. We cut off the left and bottom edges of no-signal portions of the image and used 5388×4200 pixel sized image. It is known that JERS-1 SAR system noise exists in the range direction and is higher in the either side of center and lower in the center of the scene [SED, 1995]. It suggests that the range-dependent noise remains after SAR calibration. Figure 3.2 (a) shows the azimuth-averaged profiles made from twenty SAR images. They are different from each other because the pixel value of image is the sum of the signal from the ocean and the system noise. In order to examine the noise properties, we sampled 200 scenes of JERS-1 SAR and regress the azimuth-averaged profiles with parabolic function based on the assumption that the system noise is linearly added to the ocean signals. Figure 3.2 (b) shows one example of the profile and the regression curve. They used the regression equation as

$$DN = a(x-b)^2 + c, \qquad (3.1)$$

where DN is a digital value of 16 bit image, and x is range with $x = 0$ corresponding to the far range. The regression coefficients are a, b and c. Fig. 3.3 (a) shows all profiles, whose vertexes are shifted to the same point of (2500,0). Figure 3.3 (b) shows the profile produced by averaging all the profiles in Figure 3.3 (a). Bars on the averaged profile indicate the standard deviations.

As can be seen in Figure 3.3 (a), most of the profiles are similar in shape. Actually, the standard deviation of coefficient a is very small (0.08×10^{-4}, i.e. 6% of the mean value of 1.32×10^{-4}). It can be concluded that the parabolic shape of profiles showing the JERS-1 SAR system noise is common to all the JERS-1 SAR images and that the system noise is a function of range. It is true that some profiles deviate from the regression curve, but this results from the natural phenomena captured by each scene. In Figure 3.3 (b), the variance is large on either side of center range because a small difference in coefficient a enhances the difference at both sides of the profiles.

The axis position of the parabolic function specified by the coefficient b distributes around 3270th line. The coefficient b has a standard deviation of about 290. They conclude that the location of axis is different scene by scene. Therefore, in order to express the system noise as a function of range, they need to compute the axis position for each scene through the regression. The reasons of the axis variations may be uncertainty of the JERS-1 orbital parameters and wind gradients in a scene.

We consider that the value of coefficient c depends on the wind speed, the wind direction and the other ocean parameters.

On the basis of above results, we express the system noise as a function of range. The value of coefficient a is set as the mean value 1.32×10^{-4}, which is defined as a_0. The axis position (b) of the parabolic function is estimated for each scene. We set a provisional value of c_0 at this moment. The c_0 value will be determined in the following subsection. Using these coefficients, the system noise ($DNnoise$) is expressed as

$$DNnoise = a_0(x-b_i)^2 + c_0, \quad (3.2)$$

where b_i is the axis location of each scene. By subtracting the estimated system noise from all range lines of the SAR images, we reproduce the relatively calibrated images. Hereafter these modified digital values instead of the absolutely calibrated NRCS is used and it is refered to the square of the digital value as sigma-0 (σ^0_{lin}). The speckle noise is reduced enough for digital pixel values to always be positive after removing the system noise.

3.2.3 Match-up data

In this subsection, we describe the procedure to make a match-up data set, which is composed of coincident and collocated observation variables. They are the JERS-1 SAR sigam-0 and incidence angle, and the wind speed (U) and the wind direction (ϕ) from NSCAT and the JMA buoys. The wind direction is defined as the azimuth angle between the radar-looking direction and the surface wind direcion. In this study, in order to reduce the speckle noise we define the SAR sigma-0 as a mean value of a 10-km ground square whose center is located at a geodetic position of wind vector cell of NSCAT or a buoy. In fact, sigma-0 averaged over an area larger than 10-km square varies little from a 10-km average. The10-km distance corresponds to 500-700 pixels in both the range and azimuth directions in the slant range image.

Figure 3.4 shows a scheme of match-up data generation. First, we consider the case of NSCAT. As described above, many mutch-ups are obtained when swaths of NSCAT and JERS-1 SAR overlap. An example of the overlapping swaths is shown in Figure 3.5. One vector case among the wind vectors displayed in Figure 3.4 corresponds the use of JMA buoy data. As a result, we have made 7577 match-ups, which are the sum of 7532 match-ups with NSCAT winds and 45 with JMA buoy winds. Figure 3.6 shows the histograms of match-ups for the wind speed (a) and direction (b).

Using the match-up data set, we determine the consistent level of JERS-1 SAR system noise, i.e. c_0 in (3.2). In order to produce a reasonable L-band GMF, its continuity at 0 m/s has to be guaranteed. First, we make a match-up data set using the provisional value $c_0 = 0$. Second, the match-ups are classified into bins of 1 m/s wind speed and 10° wind direction, and the outliers, which are defined as points that are more than twice of the standard deviation from the mean value of each bin, are discarded. Thus, the minimum value among wind speed bins of 0-1 m/s is 2250000 in sigma-0, which corresponds to 1500 of 16 bit digital values. We redefine c_0 as that value, i.e. $c_0 = 1500$. By using this value, sigma-0 is also redefined in order that sigma-0 is 0 when wind speed is 0 m/s. Use of this value produces positive sigma-0 from the oceans and does not cause any problems in the following analyses and results.

In order to estimate the coefficients of the L-band GMF, a simple regression (no regression weights) is used in the analysis described in the next section. This is based on the assumption that NSCAT and buoy data are error-free sea truth.

3.2.4 Characteristics of L-band backscattering at the sea surface and L-band GMF

A. Incidence angle dependence

The dependence of sigma-0 on incidence angle is examined for all the bins of wind speed and wind direction. The range of incidence angle varies from 37.0° to 42.0° within the SAR swath. Figure 3.7 (a), (c) and (e) show the examples of the incidence angle dependence for all the bin of wind direction and the bins of wind speed, 3-4 m/s, 7-8 m/s, and 12-13 m/s, respectively. Regression lines are also superimposed in the figures. The bins containing less than 10 match-ups are excluded. The level of each wind-direction bin is offset for display of all the calculated regression lines in the figures. They have no significant inclination for the range of incidence angle. Furthermore, all the regression lines shown in the Figure 3.7 (a), (c), and (e) are normalized by the sigma-0 at 39.5°, and then they are averaged over the incidence angle for each wind-speed bin. The resultant profiles with bars indicating standard deviation are shown in Figure 3.7 (b), (d) and (f), respectively. There is a slight inclination of the mean profile for the wind-speed bin of 12-13 m/s (Figure 3.7 (f)), but it should be noted that only six bins are available because of the small number of data for high wind speeds. They lie around one, which also indicates no incidence angle dependence for the range of incidence angle ($37.0° - 42.0°$). This is confirmed for the other bins, which are not shown here. Thus the dependence of incidence angle in the GMF is not considered in the follwing analyses.

B. Wind speed dependence

The dependence of sigma-0 on wind speed is investigaed using the match-ups in the wind direction bins. Figure 3.8 shows plots of sigma-0 versus the wind speed for wind directions of 0°,50°,90°,140° and 180°, which are center angles of the relative wind directions. Since the wind-speed dependences for the 180° to 360° bins are symmetric to those of 0° to 180°, we show the plots only for half of the wind-direction bins. Regression curves are also indicated in the figures. They are defined as a power law formula, which relates sigma-0 with the surface wind speed [e.g. see Wentz, 1984]:

$$\sigma^0_{lin} = 10^{\alpha} U^{\beta} \quad . \qquad (3.3)$$

The coefficient β is called "wind speed exponent", which indicates the sensitivity of sigma-0 to the wind-speed increase. The coefficients α and β are determined through regression of the equation (3.3) against the match-up points.

In each wind direction bin, sigma-0 increases with the wind speed. The coefficient β is a variable of the wind direction. For the wind direction of 0°(upwind), sigma-0 has the largest increasing rate against the wind speed. The increasing rate dcreases with increase and the minimum increasing rate is seen at $\phi = 90°$(crosswind), where sigma-0 has a tendency of saturation at the high wind speeds. Sigma-0 increases rather linearly with the wind speed for the wind direction of 180°(downwind). The wind speed exponents are 2.25, 0.50, and 1.18 at upwind, crosswind, and downwind, respectively.

C. Wind direction dependence

The dependence of sigma-0 on the wind speed is investigaed for all the wind direction bins. Figure 3.9 shows plots of sigma-0 versus the wind direction for the wind speeds from 0-1 m/s to 19-20 m/s every other bin. In order to express the dependence of wind direction, second-order cosine harmonics formulas of the wind direction have been used by several researchers [e.g. Wentz, 1984]. In the present case, difference between the wind-speed dependences for upwind and downwind is large when the wind speed exceeds 10 m/s as seen in the previous section. Therefore, conventional second-order harmonics formulas cannot express this deformed wind-direction dependence. In other words, it can not express the positions of the minimums at 90° and 270° and the large upwind/downwind asymmetry at the same time. For regression analyses, we adopt a third-order harmonic formula:

$$\sigma^0_{lin}(U,\phi) = a_0(U) + a_1(U)\cos\phi + a_2(U)\cos 2\phi + a_3(U)\cos 3\phi \quad . \qquad (3.4)$$

$a_i(i = 0,1,2,3)$ is the regression coefficients.

The signal level for the whole wind direction increases with wind speed. For wind speed below 7 m/s (Figure 3.9 (a)-(c)), it can be concluded that the significant dependence on the wind direction does not exist, though the crosswind peak is systematically higher than the upwind and downwind peak. However, for the wind speed of 7 - 8 m/s, the upwind peak starts to dominate. For the wind speed of 9 -10 m/s, the downwind peak also dominates following the upwind peak. When the wind speed becomes 11-14 m/s, the differences among the upwind peak and the downwind peak and the crosswind troughs become clearer, which continue toward higher wind speed.

For the wind-speed range of 15 - 20 m/s, because of a small number of the match-ups and their non-uniform distribution in the wind direction of each wind-speed bin, the regression analyses are less reliable. Therefore, in order to estimate better regression formula, we decide to extrapolate, toward the higher wind-speed range, the relation of wind speed dependence at $\phi = 0°, 50°, 90°$, $140°$ and $180°$ shown in Figure 3.8. Then, using the extrapolated values at these wind directions, the coefficients of harmonic formula are computed (the solid lines in Figure 3.9 (h)-(j)). The determined curves for the high wind speeds do not conflict with the match-up plots in the figures.

D. L-band GMF

We develop an L-band GMF on the basis of the regression coefficients determined in the previous subsections, (Figure 3.8 and Figure 3.9). Considering no dependence on incidence angle in its range of present study ($37.0° - 42.0°$), the model derivation is then reduced to determining the wind speed dependence of the regression coefficients in (3.3). Figure 3.10 shows the coefficients of the harmonic formulas (3.4) versus the wind speed. In Figure 3.10 (a), it is shown that the relationship between the coefficient a_0 and the wind speed changes drastically at around $U = 8$ m/s. Figure 3.10 (b) shows the relationship in a logarithmic diagram. We represent the relationship by these lines as $\log_{10} a_0 = a + b \log_{10} U$, which are connected at $U = 8.5$ m/s. On the basis of the above, the coefficient a_0 is expressed by

$$a_0 = \begin{cases} 10^{b_1} U^{b_2} (U < 8.5) \\ 10^{b_3} U^{b_4} + b_5 (U \geq 8.5) \end{cases} , \qquad (3.5)$$

where the coefficient b_5 works to connect these at $U = 8.5$ m/s.

Figure 3.10 (c), (d) and (e) indicate behaviors of the coefficients a_1, a_2 and a_3, respectively. We consider that the continuity of GMF at $U = 0$ m/s is fulfilled and that the wind-direction dependence for low wind speeds is not significant, and represent their behaviors by the following formulas;

$$a_1 = b_6\left(e^{b_7 U} - 1\right) \quad , \tag{3.6}$$

$$a_2 = b_8 U^2 + b_9 U \quad , \quad \text{and} \tag{3.7}$$

$$a_3 = b_{10}\left(e^{b_{11} U} - 1\right). \tag{3.8}$$

An L-band GMF is formulated by using the model parameters determined above. Its 3-dimensional view is shown in Figure 3.11. From the figure, we can see the sigma-0 dependence on the wind speed and the wind direction. Model formulation and its coefficients are summarized in the Appendix 2.

E. SAR wind retrieval using JERS-1 SAR

Figure 3.12 shows a comparison of the wind speed derived from JERS-1 SAR using the L-band GMF with NSCAT and JMA buoy wind direction and NSCAT and JMA buoy wind speeds. The root mean square error (RMSE) is 2.09 m/s, and the bias is negligible (-0.0006 m/s). The SAR-derived wind speeds generally agree well with the NSCAT and JMA buoy wind speeds. Though the points scatter in a wide range for the wind speeds of 5-10 m/s, their distribution ranges become smaller for the wind speeds higher and lower than these. For wind speed below 2 m/s, this GMF slightly underestimates them compared with those of NSCAT and the JMA buoys. It should be noted that NSCAT winds are noisy below 3 m/s. Some plots exhibit large scatter around the 20 m/s of SAR-derived wind speed. It is found that most of large errors are the data around crosswind directions.

Now we apply the L-band GMF to the JERS-1 SAR image to generate a high-spatial resolution wind-speed map. Figure 3.13 (a) shows one image obtained on May 18, 1997 in the Pacific. First, we subtract the estimated SAR system noise form the SAR data. Second, to reduce the speckle noise and image volume, the SAR image is averaged by 8×8 pixels, resulting in 736×640 sized pixels. Finally, they apply the L-band GMF to sigma-0 of the SAR image to convert it into the wind speed (Figure 3.13 (b)). The wind directions in the image are given by the corresponding NSCAT wind vectors, which are superimposed by arrows and wind-speed values. The SAR-derived wind speed is displayed by gray tones with the scales of wind speed. They agree well with the NSCAT wind speed at the coincident points within the RMSE range. Small-scale patterns in the wind-speed field are visible in the SAR image of 75-km square, which are not captured by NSCAT and probably related to mesoscale wind features. The range dependent pattern associated with the SAR system noise is not seen, which suggests that the ocean wind signals are successfully extracted through the present methodology.

3.3 Evaluation of JERS-1 SAR images from wind retrieval point of view

3.3.1 Excessive ambiguity of JERS-1 SAR

Here one must notice the wording of "excessive ambiguity". When the data sequence from a radar is sampled, the presence of ambiguities must be considered. Ambiguities are unwanted contributions to the image. They are always present due to pulse repetition from the radar and the resulting aliasing, which are inherent to radar systems. In most SARs under the present circumstances, the azimuth and range ambiguities should not be a source of contamination of the signal of interest, by design. However, JERS-1 SAR is an exception. For the ambiguities which originate from bright targets such as land, the contributions of them to the signals from coastal seas are so significant that they can contaminate the signal of interest. In such cases, ambiguities can not be neglected. Therefore, we use the term "excessive ambiguities" to refer to the significant ambiguities of JERS-1 SAR in order to differentiate them from ambiguities in an ordinary sense. It is verified in the sessions above that the ambiguities are not significant in open oceans because the results of wind retrieval are good. Because the intensity of backscattering from sea surface is originally weak compared with that from land, the resulting ambiguities are not significant. Note that Sigma-SAR processor uses 70 % of the bandwidth, which is centered at the doppler frequency, mainly for improving the focusing and partially for reducing the azimuth ambiguity.

Figure 3.14 shows the schemes of both range and azimuth ambiguities in the Sagami Bay. Ambiguities come from outside of the intended imaging target and are folded into the backscattering intensity of the target. Range ambiguities [Henderson and Lewis, 1998] appear to arise from scatterers at either side of about 90 km [Shimada, 1994] from the JERS-1 SAR imaging point (Figure 2 (a)). On the other hand, azimuth ambiguities [Henderson and Lewis, 1998] are due to reflections that are captured by the edges or sidelobes of the antennas along-track illumination pattern, and appear to repeat image elements in the scene at multiples of 17 km in the along-track direction of the swath. The first-order (nearest) ambiguities generally are the strongest (Figure 14 (b)). Their intensities decrease with the distance from the true imaging target [Shimada, 1994].

Figure 3.15 is an example of JERS-1 SAR image of Sagami Bay. We can see the intense azimuth ambiguity in the center part of the scene. The excessive azimuth ambiguitiy originated from bright targets such as cities are often recognized in the coastal scenes of JERS-1 SAR.

As a preliminary analysis, we compared ERS-1 SAR-derived wind-speeds at the Hiratsuka tower and the in situ wind speed measurements at the Hiratsuka tower (Figure 2.2). Wind speeds are retrieved using the CMOD IFR2 scatterometer wind model [Quifen et al., 1998] and in situ wind direction. Figure 3.16 shows the results, which are indicated by different symbols for onshore/offshore wind cases. In the onshore cases, winds are blowing from southwest and southeast, and in the offshore cases the other directions. The resulting RMSE is 2.13 m/s and bias is –0.48 m/s. In conclusion, though retrieved wind are somewhat underestimated, little dependence on the onshore/offshore wind direction is seen, and the wind-speed is generally well retrieved even at the near coast in the Sagami Bay.

3.3.2 Method

In order to investigate the JERS-1 SAR characteristics during the analyzed period, we sampled sigma-0 values from the 110 scenes of JERS-1 SAR at the Hiratsuka tower. Figure 3.17 shows a time series of the differences between sigma-0 observed at the Hiratsuka tower and estimated by the L-band model function with in situ wind speed and direction. During the term of JERS-1 initial mission check (Feb.-Aug.1992), the differences of sigma-0 are fluctuating. Since the start of JERS-1 operational mode at the end of Sep. 1992, the differences of sigma-0 are steady and deviate around a constant level (2.2×10^7). The standard deviation is 1.8×10^6 and the relative root mean square error is 0.08. In the present study, JERS-1 SAR images obtained during the operational mode period are used.

In order to estimate excessive ambiguities and investigate JERS-1 SAR-derived wind-speed, we focus on simple cases in which the wind blows from north in the Sagami Bay. The range of wind direction observed at the Hiratsuka tower is within $340° - 20°$ (See Figure 3.18). It is assumed that the wind direction is uniform over the profile line. The method we employed is as follows. First, we derive the profiles of sigma-0 along the assumed wind direction from JERS-1 SAR images. As the same way, NRCS profiles are derived from ERS-1 SAR images. Note that NRCS refers to the absolutely calibrated one.

Next, wind speed profiles are derived from the sigma-0 and NRCS profiles using the L- and C-band model functions. The wind speeds derived from JERS-1 SAR should be overestimated due to excessive ambiguities. Then, a wind speed profile derived from ERS-1 SAR is normalized by its mean wind speed. We derive common feature between them and modeled it by a simple formula. Finally, using this formula and a wind speed of Hiratsuka tower, the expected variation of wind speed with offshore distance at the JERS-1 SAR observation is derived. We convert the wind speed profile into that of sigma-0. The difference between the observed and the estimated sigma-0 profiles are derived as the excessive ambiguity.

The method is concretely described below. Figure 3.19 (a) shows the variation of wind speed with offshore distance derived from ERS-1 SAR. Each profile is normalized by its mean wind speed. The start point is the location of Hiratsuka tower. It is clearly shown that wind speed generally increases with the distance from shore and that all the profiles agree well with each other. Figure 3.19 (b) shows the mean of all the profiles, its standard deviation and the regression line. The formulation of the regression is defind as;

$$U/\overline{U} = a\ln(b(x+c)) \quad , \tag{3.9}$$

where a, b, c are coefficients, x is the offshore distance in km and $\overline{U}$ is mean wind speed. The values of coefficients are 0.2954, 0.7933 and 5.3476, respectively. The standard deviation is relatively small. It can be concluded that there exists a common feature of wind speed growth with offshore distance in the bay and that the empirically derived profile of wind speed, which is formulated by eq. (2), represents it well.

3.3.3 Comparison between ERS-1 and JERS-1 SAR-derived wind speeds and tower wind speeds

Figure 3.20 shows the comparison of SAR-derived wind speeds at the distances of (a) 20 km, (b) 32 km, (c) 44 km and (d) 55 km against the coincident tower wind speeds for both ERS-1 SAR and JERS-1 SAR. The broken line is the regression line for all the plots. Because the data were not acquired at the same time for ERS-1 and JERS-1 SAR, we can not directly compare ERS-1 and JERS-1 SAR-derived wind speeds. So, note the relations between SAR-derived wind speeds and tower observed wind speeds for ERS-1 and JERS-1. At the distance of 20 km, almost all the wind speeds derived from JERS-1 SAR are larger than 18 m/s, which is due to the excessive ambiguity in the SAR image. At the distance of 32 and 44 km, the JERS-1 SAR-derived wind speeds are much larger than in situ wind speeds. In the case of 55 km distance from shore, both JERS-1 and ERS

SAR-deived the wind speeds scatter around the regression line. It is shown that, at the distance of 55 km, the wind speeds derived from ERS-1 SAR and JERS-1 SAR have the same relationship against the tower wind speeds. The relationship is considered as the growth of wind speed with offshore distance. Wind speeds at the distance of 55 km are about twice larger than those at the tower (located 1 km off shore), which is consistent with the normalized profile of wind speed shown in Figure 3.19.

Using eq. (3.9), wind speeds at the distance of 1 km are estimated from the JERS-1 SAR-derived wind speeds at the distance of 55 km. Figure 3.21 shows the comparison between them and the Hiratsuka tower wind speeds. Profiles which do not pass over the Ooshima are used. The estimated wind speeds agree well with the in situ observations, and RMSE is 2.12 m/s and bias is 0.51 m/s. This result suggests that the normalized profile of wind speed represents the growth of wind speed with offshore distance even in the cases of JERS-1 SAR.

3.3.4 Estimate of excessive ambiguity

On the basis of above results, the excessive ambiguity is estimated. Solid line in Figure 3.22 (a) is an example of a profile of the JERS-1 SAR sigma-0. Solid line in Figure 3.22 (b) is the correoponding profile of wind speed by the L-band model function. Using eq. (3.9) and the JERS-1 SAR-deirived wind speed at the distance of 55 km, the expected profile of wind speed is derived. The corresponding profile of sigma-0, which is derived by the L-band model function, is shown by the broken line in Figure 3.22 (a). Thus, the difference between SAR-observed and estimated profiles of sigma-0 is obtained as the excessive ambiguity. These calculations are made for the selected JERS-1 SAR images. In Figure 3.22 (c), mean profile and the standard deviations of the resulting profiles are shown. It is shown that, within 20 km of offshore distance, the estimated excessive ambiguity is especially high. In the farther distances, excessive ambiguity is little but systematically positive value within 50 km from the coast.

3.4 Discussion

3.4.1 Relative calibration

The calibration factor to convert the JERS-1 SAR 16-bit digital output from the Sigma SAR Processor to the calibrated NRCS has been proposed. The calibration factor was calculated as a comparative study NASDA and the ASF (Alaska SAR Facility), and done by Dr. B. Chapman of NASA/JPL. While absolutely calibrated NRCS can be derived for bright targets, NRCS derived from dark targets like ocean goes with the errors due to the system noise. We consider that the relative calibration of JERS-1 SAR sigma-0 conducted in the present study is a practical way for the SAR wind retrieval using JERS-1 SAR. While the incidence angle dependence of sigma-0 is possibly affected by the method of the noise removal, the derived sigma-0 has a distinct dependence of wind speed and direction, which can be considered as the representative relationship among sigma-0, wind speed and wind direction only for an incidence angle of about 40°. There are few studies comparable with the whole results of the present study. Unal et al. (1991) contains the L-band backscattering characteristics at the sea surface. However, since the number of used data was small, they showed only a few features of relationships among the L-band backscatter, incidence angle, and ocean surface vector. The revealed features by Unal et al. (1991) are consistent with the results of the present study in the following points; the wind exponent for the upwind, the upwind/downwind ratio and the upwind/crosswind ratio for wind speed of 10 m/s. Phased Array type L-band Synthetic Aperture Radar (PALSAR) onboard ALOS is planed to be launched in 2004. Since it has incidence angles ranging $8^\circ - 60^\circ$, new researches are necessary to clarify the incidence-angle characteristics and derive its GMF for wind-speed retrievals on the basis of present study. It could also add value to other L-band microwave sensors such as the Soil Moisture and Ocean Salinity Mission (SMOS) and NASA Aquarius mission, which are to be flown around 2006 for sea surface salinity retrievals.

3.4.2 Global validation

It is known that the satellite scattrometers using the C-band (ERS-1/2 AMI) and Ku-band (ADEOS-1/NSCAT, QuikSCAT/SeaWinds) have functioned well and provided global surface winds. The GMFs for the C-/Ku- bands are well validated globally. In contrast, the new L-band GMF presented here is validated only in the seas around Japan. The large number of JERS-1 SAR ocean scenes is only available within the coverage of its home receiving station. However, since the NSCAT surface winds used as the sea-truth data have been validated for the global oceans [e.g., see Ebuchi, 1997] and we collected many match-ups in wide parameter ranges of the surface wind, the new L-band GMF may be reasonably applicable for the global oceans.

3.4.3 Comparison with C- and Ku-band model functions

The wind retrieval error is considered to be mainly relating to two problems. One is the wind direction problem. Though, in order to retrieve wind speed with high-spatial resolution, we also need high spatial-resolution wind direction [Portabella et al., 2002], it is very difficult to obtain reliable high-resolution in situ surface wind data. However, for the L-band wind retrieval at low wind speeds, lack of high-resolution wind direction have less influence on the wind retrieval because the dependence of wind direction is little. For cases of high wind speeds, it can be expected that the mean wind direction does not change rapidly at such a small scale that SAR can detect. The next problem is the small-scale features, which can be observed by SARs; e.g., influnces of depth fluctuations, currents, slicks and fetch influence on the surface waves and radar backscattering. These appearances are enhanced in the coastal sea. In the present study, however, the influences of these features on the GMF examination may not be significant since all the match-ups are generated using the observations in the open oceans.

3.4.4 Excessive ambiguities

We estimated the JERS-1 SAR excessive ambiguities as the differences between the observed sigma-0 and the estimated sigma-0 by the growth of wind speeds with offshore distance. It is reasonable to consider the diferrence of sigma-0 as the excessive ambiguities because the excessive ambiguities are prominent only in the coastal region. The errors due to wind retrieval and the generalized formula of wind speed growth cause the estimates of excessive ambiguity.

It is reasonable to conclude that excessive ambiguities contaminate the estimated wind speeds from the coastline up to at least 50 km, though the excessive ambiguities become weak with the offshore distance. Within 20 km of distance, excessive ambiguitiy is especially high. It is considered as the first azimuth ambiguity. It is reported in Shimada [1994] that the distance at which the first azimuth ambiguity appears is 17 km away.

Wind speeds are overestimated within 50 km from the coast. In the JERS-1 SAR image, it is suggested that not only the first azimuth ambiguity, but also higher-order ambiguities and range ambiguity, may have a significant impact on wind retrieval. The relative contributions of the range ambiguity and the higher-order azimuth ambiguites cannot be determined.

We consider the ratio of excessive ambiguity to wind signal. Signal to Ambiguity (SA) ratio is defined by Shimada et al. [1994] as this;

$$SA = 10\log_{10}\left(\frac{I_{ambiguity}^2 - I_{ocean}^2}{I_{city}^2 - I_{ocean}^2}\right) \quad , \qquad (4.1)$$

where $I_{ambiguity}$, I_{ocean} and I_{city} indicate the 16 bit image intensity of ambiguity, ocean, and wind signal component, respectively. Here, we simply consider the ratio of the excessive ambiguity to the wind signal.

It is found that, sigma-0 corresponding to wind signal component varies from 0 to 4.0×10^6 for wind speeds of 0-20 m/s from the L-band model function. On the other hand, the first ambiguity is as large as 2.3×10^6 at the distance of 5 km (Figure 3.22(c)). It can be concluded that the dynamic range of wind signal is as large as that of the first azimuth ambiguity. In other word, the first azimuth ambiguity due to urban reflections has intensities as large as sigma-0 corresponding to high wind speed more than 10 m/s. For example, the ambiguity intensity is 1.0×10^5 at the distance of 40 km even in the third azimuth ambiguity area (Figire 3.22(c)). If the wind speed is 10 m/s, sigma-0 is roughly 1.0×10^6 for the all the wind directions according to the L-band model function. In such a case, the error, which is a ratio of ambiguity component to wind signal, can be 10 % in estimating sigma-0.

It should be evident that wind speed retrieval from JERS-1 SAR is difficult within 50 km from the coast. When retrieving coastal wind speeds from JERS-1 SAR, we must take into account excessive azimuth and range ambiguities, and should not use the estimated wind speeds in those areas. However, it is important in the present study that the excessive ambiguities in the ocean of JERS-1 SAR images are qualitatively estimated. These results will be the basis for other ocean applications of JERS-1 SAR.

It may be worth mentioning, in passing, that wind signal can be occasionally derived in coastal zones. If the coast is parallel to the azimuth direction, the azmuth ambiguity that arises from coastal areas does not appear in the ocean and does not become a source of noise in estimating sigma-0. Moreover, range ambiguity is not significant compared to azimuth ambiguity. We can give an example of the east and west side of Tohoku area in Japan. If wind speeds are derived in such a case, wind speeds will have a relatively low constant bias. If, on the other hand, coastal land is covered by low-backscatter and uniformly distribution targets, wind signal can be derived even in the presence of the first azimuth ambiguity. The following is a good example. Radar backscatter of JERS-1 SAR and in situ wind measurements in the Lake Sinji, Japan are compared by Ichikawa et al. [2002]. The lake is surrounded by mountains and the ambiguities should be folded into the backscattering intensity from the lake. But, the relationship between radar backscatter and wind vectors is consistent with the L-band model function proposed in the present study.

3.4.5 Growth of wind speed with offshore distance

In the present study, we generalized the growth of wind speed with offshore distance for the northerly wind in the bay (eq. (3.9)). It is shown that the wind-speed growth profiles normalized by mean wind speed agree well and that ERS SAR wind retrieval is useful for capturing the growth of wind speed with distance from shore. In the study, wind direction in the bay is assumed to be uniform as in situ observations. But wind direction may not cause signigicant error of wind speed in the northerly wind cases because the normalized profiles agree well each other.

The growth of wind speed with offshore distance in the bay results from two factors. One is due to the evolution of marine internal atmospheric bondary layers. The aerodynamical roughness over the sea is usually much smaller than that over the land. In the coastal region, the large roughness over the land disappears, and the new internal atmospheric boundary layer starts growing over the sea along the offshore distance. Such relaxation of the internal boundary layer causes the increase of wind speed with distance. The other is due to the effect of upstream mountainous terrain on the wind. Though the effect of the upwind terrain decreases with offshore distance, a northerly wind can be influenced by it.

We compare the variation of wind speed with offshore distance derived in the study to those of the previsous studies. Several studies investigated growth of wind speed using the air-borne systems, the altimeters and the scatterometers [Taylor and Lee, 1984; Smith and MacPherson, 1987; Dobson et al., 1989; Ebuchi et al.,1992; Ebuchi, 1999]. Comparisons between the variations of wind speed in the boundary layers over land/sea in the case of offshore wind are summarized by Ebuchi et al. [1992] as shown in Figure 3.23. The original figure is adopted from Dobson et al. [1989). The relationship derived from ERS-1 SAR in the present study is also shown in Figure 24. The difference of the heights of wind measurement may not affect the results very much. When the logarithmic wind profile is assumed, the ration of wind speeds at the two heights is proportional to the root of the drag coefficient [Ebuchi et al. 1992]. The drag coefficient may change with evolution of wind wave and the atmospheric boundary layer. However, the change of the drag coefficient can be considered to be small and does not affect the results.

The result in the present study is a continuous profile because it is derived from SAR. It has smaller values than those of the other studies within 30 km distance. This suggests that the roughness of upwind city is larger than expected and that coastal wind is influenced by upwind terrain.

More studies are required for the growth of wind speed within 100-km scale. It relates the evolution of internal atmospheric boundary layer and the coupling effects of wave and wind under this transiton region. For such studies, SAR is a very useful tool.

3.5 Summary

We have developed a new L-band geophysical model function using the JERS-1 SAR images. Then, retrieved wind speeds from JERS-1 SAR in the coastal region are examined and excessive ambiguities of JERS-1 SAR are quantitatively estimated. The following results are obtained.

1) We estimated the SAR system noise, which has been a serious problem peculiar to the JERS-1 SAR. It is found that the system noise has a feature common in all the SAR images and the azimuth-averaged profile of noise can be expressed as a parabolic function of range. By subtracting the estimated system noise from the SAR images, we extracted the relatively calibrated ocean signals.

2) We investigated the sigma-0 dependence on the radar incidence angle, the wind speed, and the wind direction. Results of the present study indicated that dependence of sigma-0 on the incidence angle is negligible for its range of $37.0° - 42.0°$. Dependence of sigma-0 on the wind speed can be well expressed by the conventional power law formula. For higher wind speeds, the upwind-downwind asymmetry becomes very larger. But, for wind speeds below 8 m/s, these features are not significant.

3) We produced a new L-band-HH GMF for wind retrieval from JERS-1 SAR using third-order cosine harmonics. It enables us to convert a JERS-1 SAR image into a wind-speed map. The SAR-derived wind speed has a RMSE of 2.09 m/s with a negligible bias against the NSCAT wind speed comparison field.

4) Focusing on the cases where wind blows from shore in Sagami Bay, we investigate phenomena of wind-speed increase with offshore distance using ERS-1 SAR-derived wind speeds. The relation between wind speed and offshore distance are well formulated.

5) The excessive ambiguity is estimated as the difference between JERS-1 SAR-observed sigma-0 and the estimated sigma-0 by applying the formulation of wind speed growth with offshore distance. As a result, the dynamic range of first azimuth ambiguity is as large as that of the wind-relating signal from the ocean surface. Moreover, higher order azimuth ambiguities and range ambiguity also may have a significant impact

on near-shore wind retrieval.

Table 3.1 Previous studies of the relation of L-band radar cross section and wind vector . σ^0 is the normalized radar cross section, U is wind speed, ϕ is the relative wind direction, and a, b and k are the coefficients.

Reference	Data		Wind direction data	results	Model Function
Weissman et al.,1979	Airborne SAR NASACV-990,NOAA P-3	A comparison of L-band cross sections from hurricane with wind speed and direction from aircraft measurements	aircraft measurements	Good ageement of the wind speed multiplied by directional factor and wind speed from measurements.	$\sigma^0 \propto U^a\left[1+b\cos(2\phi)\right]$
Thompson etal,1981	SEASAT pass 1126,1169,1255	A comparison of L-band cross sections with wind speed and direction from SASS	SASS	L-band cross section is approximately proportional to the square root of wind speed.Upwind /cross wind difference is as large as ten percent int the range of wind speed.	$\sigma^0 \propto U^a\left[1+b\cos(2\phi)\right]$
Gerling,1986	SEASAT pass 1339	An extraction of wind speed and direction from SAR imagery.	SASS and NOAA P-3 aircraft	Good agreement of SAR estimates and SASS wind speed.SAR direction estimates from spectra of 6.4kmsquare image have a precision of approximately10degree.	$\sigma^0 = kU^a$
Keller et al.,1990	L-band antenna set to the tower	Little wind speed dependence	measurements at the tower	Little wind speed dependence above about 3m/s,but large dependence on wind speed	$\sigma^0 \propto 5\sqrt{U}$
Long et al.,1996	YSCAT ultrawideband scatterometer	Dependence of wind speed exponent on incidence angle and Bragg wavelength	measurements at the tower	Little dependence of wind speed exponent on incidence angle	

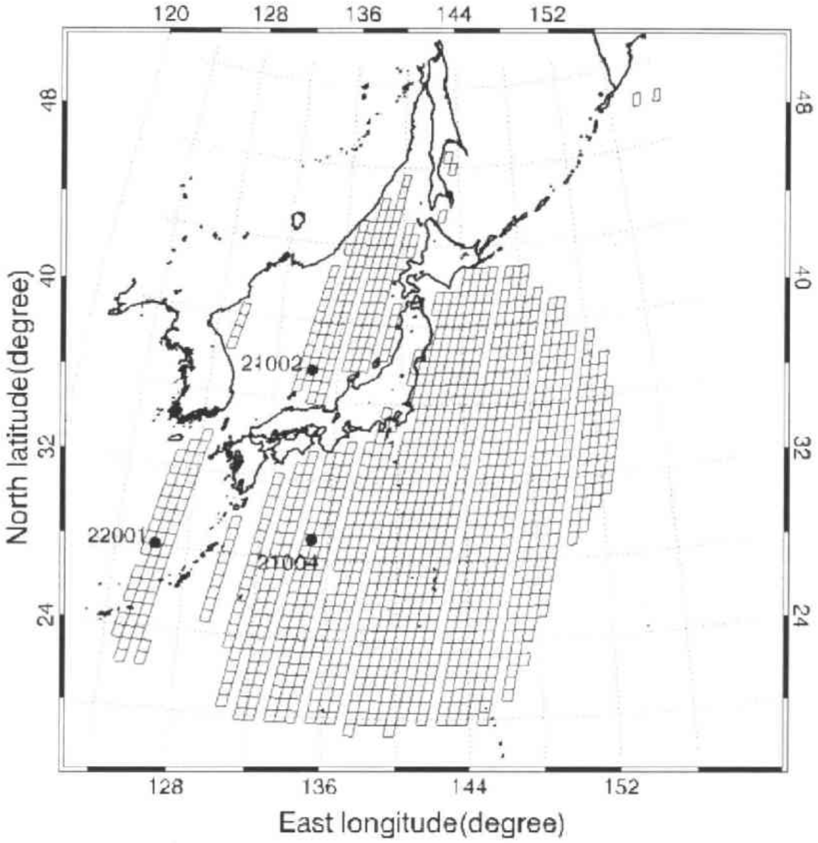

Figure 3.1 Map of coverage of JERS-1 SAR observations utilized in this study and the location of JMA buoys (WMO buoy nos., 21002, 21004, and 22001).

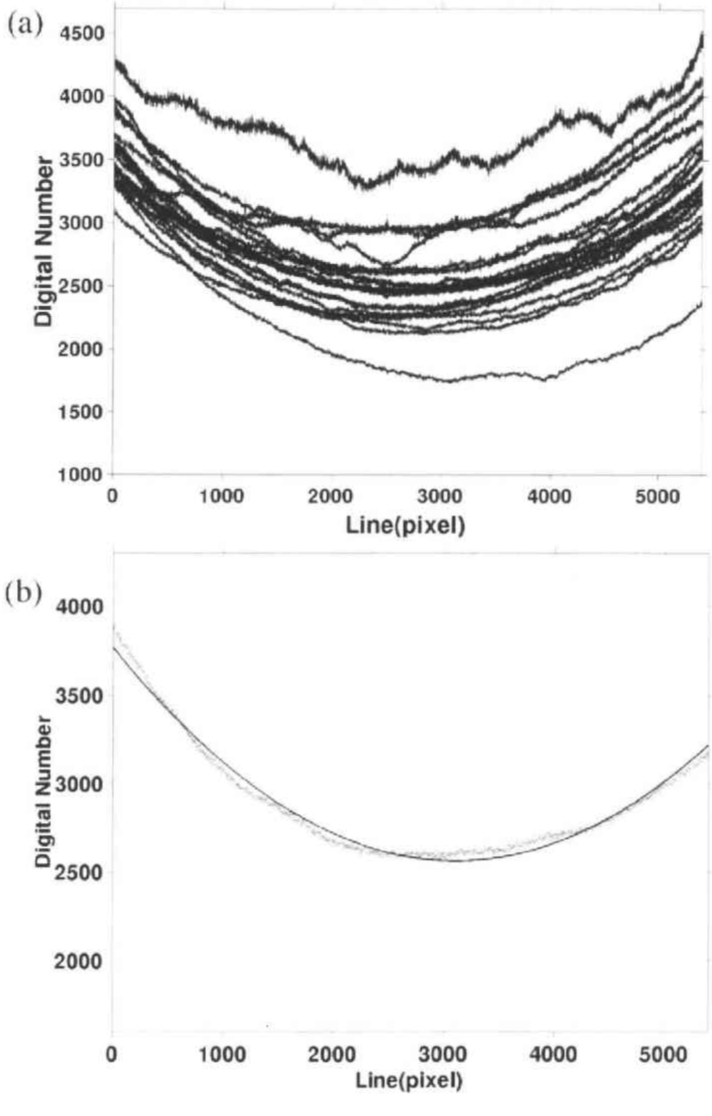

Figure 3.2 (a) Comparison of range profiles of JERS-1 SAR image, which are averaged over azimuth direction. (b) A profile averaged over azimuth direction of the slant range image (dotted line) and regression curve of parabolic function (solid line).

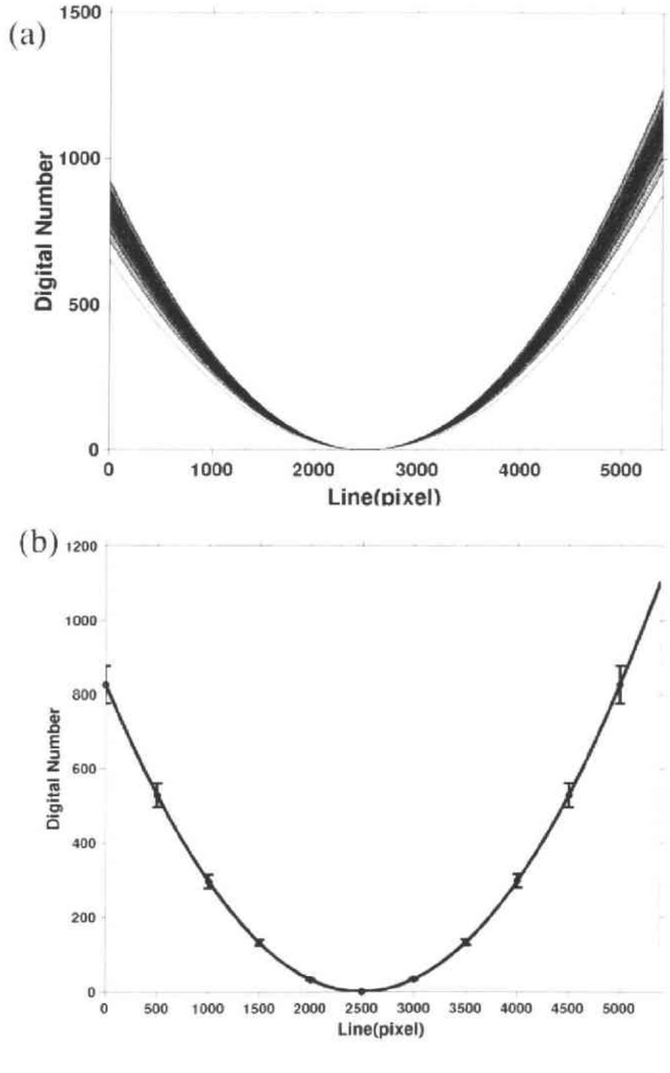

Figure 3.3 (a) Comparison of range profiles. A vertex of every profile is moved to (2500,0). (b) Mean range profile averaged over each line. Error bars show the standard deviation.

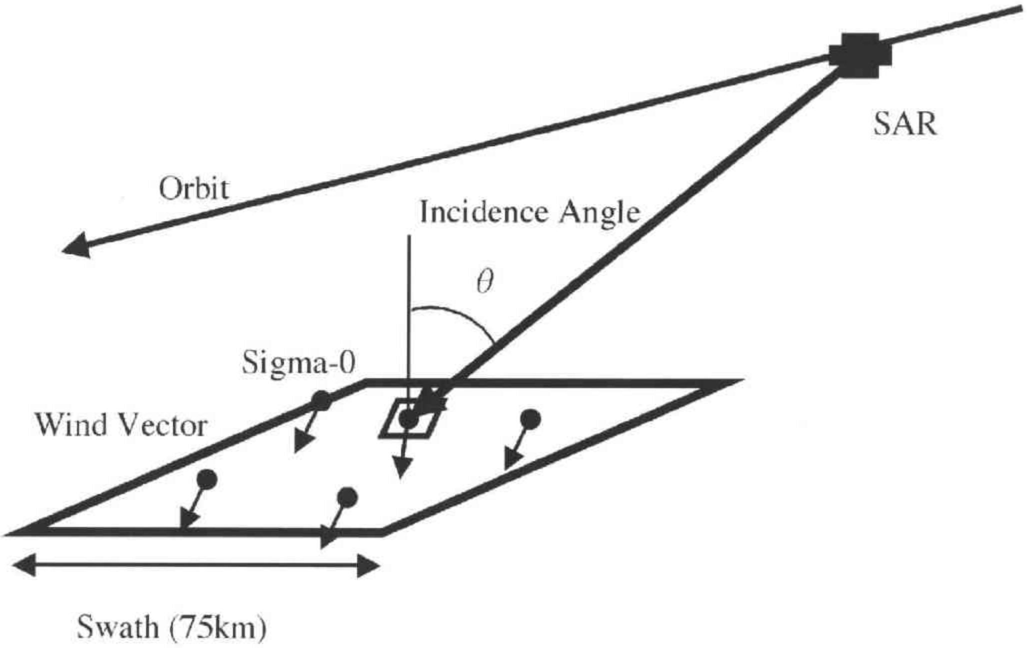

Figure 3.4 A scheme of match-up data generation using wind vectors from NSCAT and JMA Buoys.

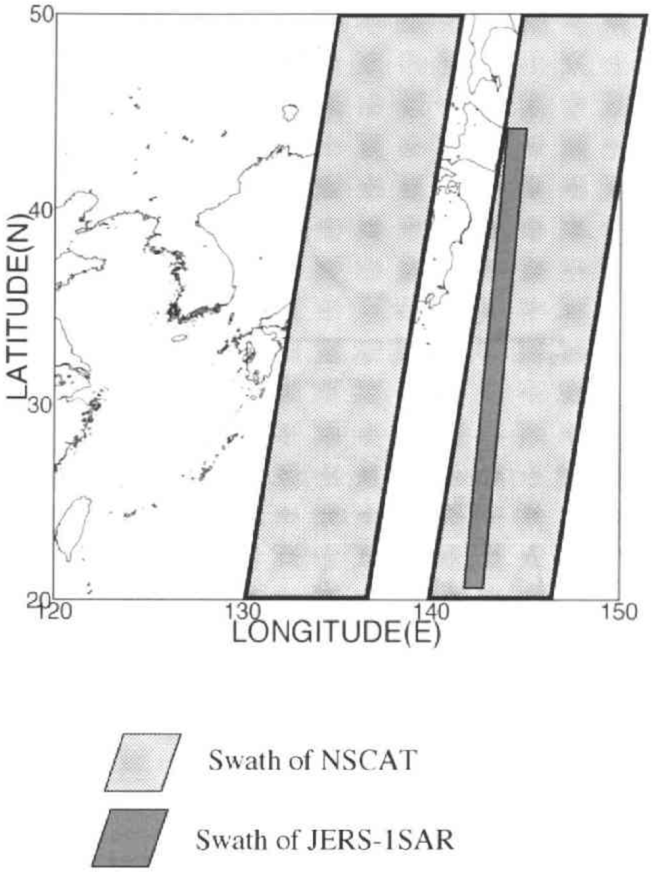

Figure 3.5 An example of overlapping swaths of NSCAT and JERS-1 SAR (October 6, 1996).

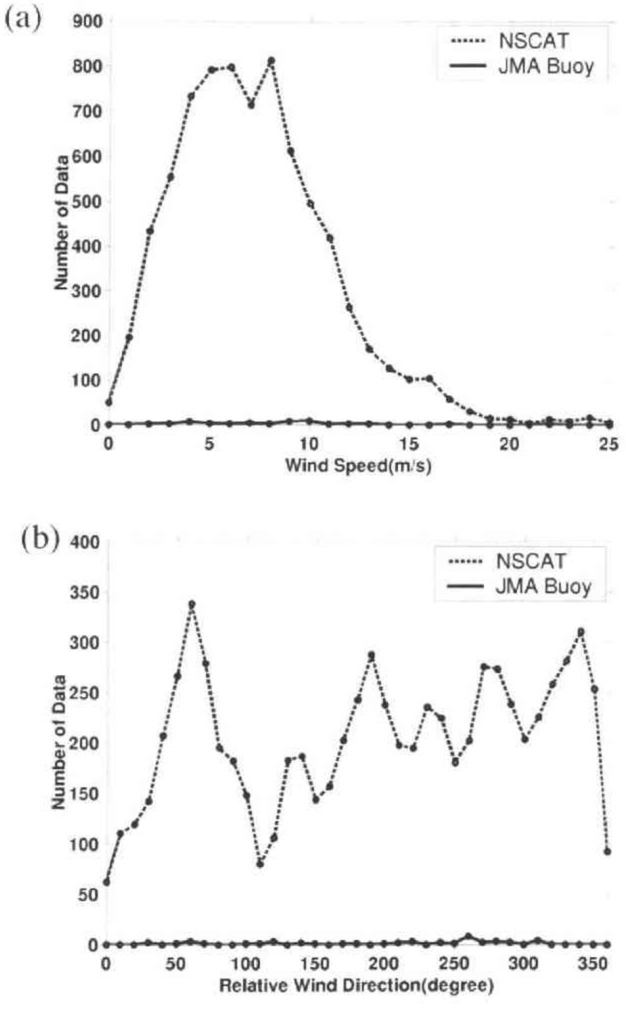

Figure 3.6 Histograms of the number of match-ups for (a) wind speed and (b) wind direction.

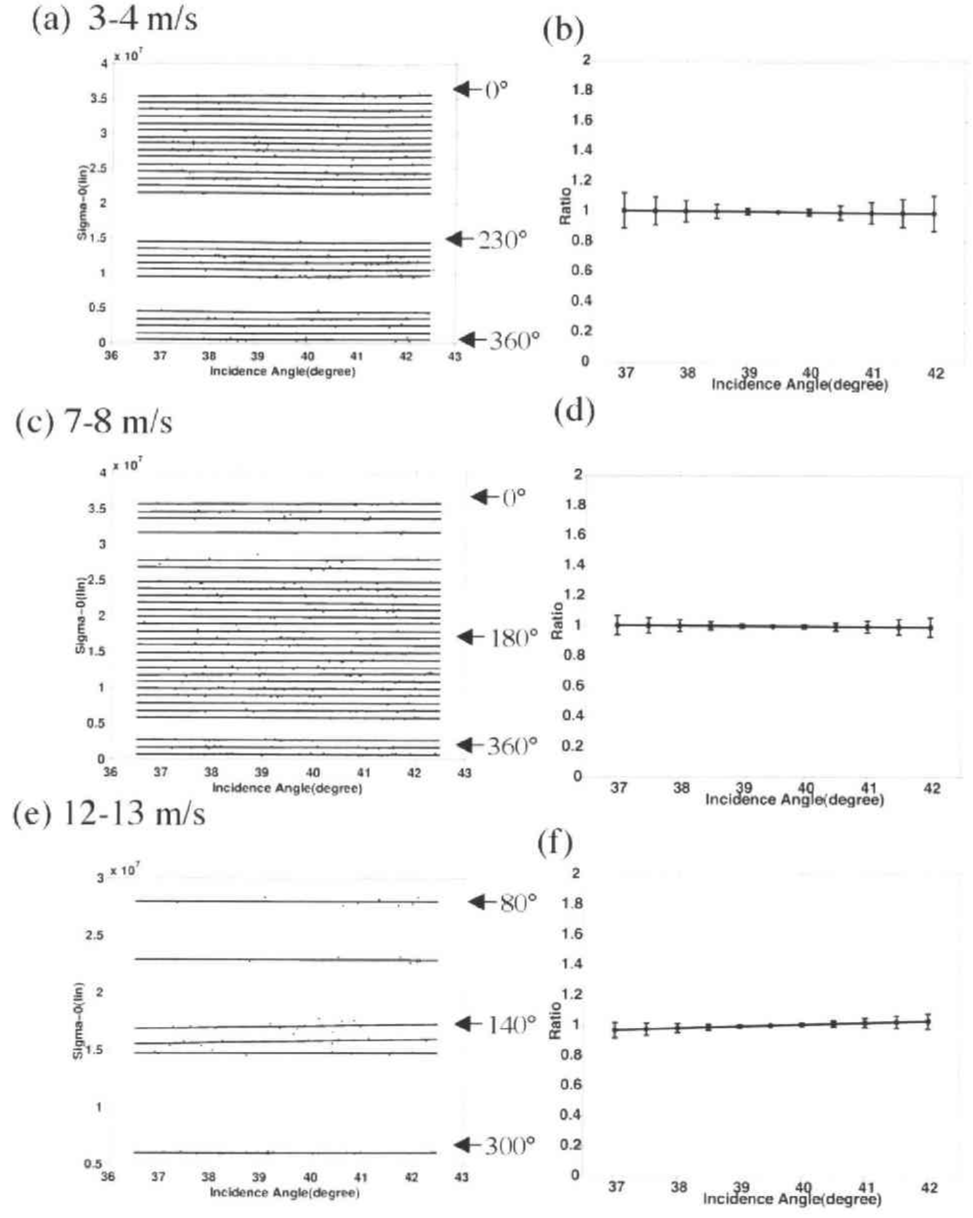

Figure 3.7 Dependence of sigma-0 on incidence angle. (a), (c) and (e) shows the incidence angle dependence for the wind-speed bins, 3-4 m/s, 7-8 m/s, and 12-13 m/s, respectively. The plots and regression line are shown for the wind-direction bins containing the match-ups more than ten. The level of each wind-direction bin is offset for display of all the calculated regression lines in the figure. (b), (d) and (f) indicate the mean profiles normalized by sigma-0 at 39.5° with standard deviation for the wind-speed bins, 3-4 m/s, 7-8 m/s, and 12-13 m/s, respectively

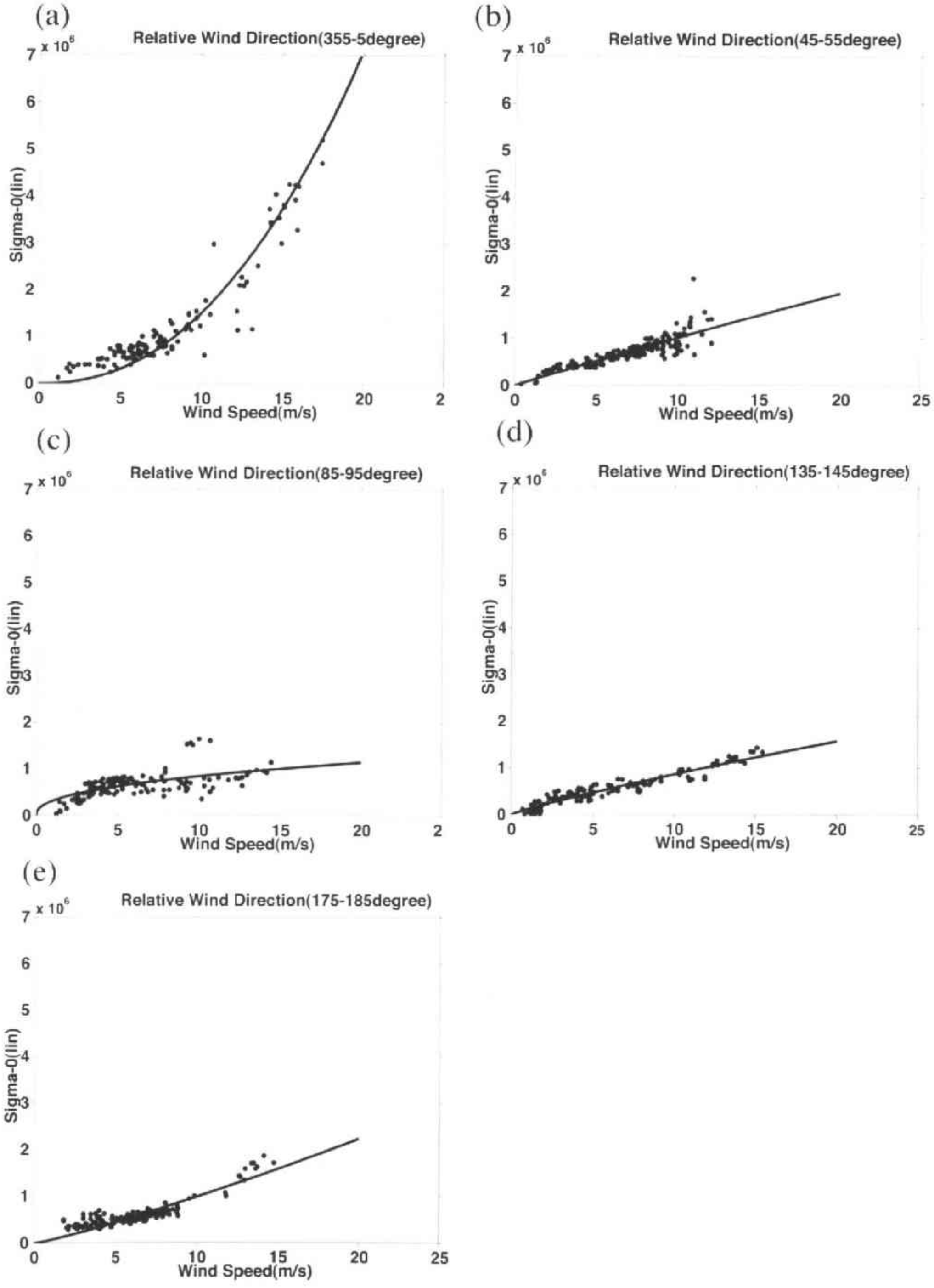

Figure 3. 8 Dependence of sigma-0 on wind speed for the relative wind direction of (a) 0°, (b) 45°, (c) 90°, (d) 135°, and (e) 180°. The regression lines are also shown.

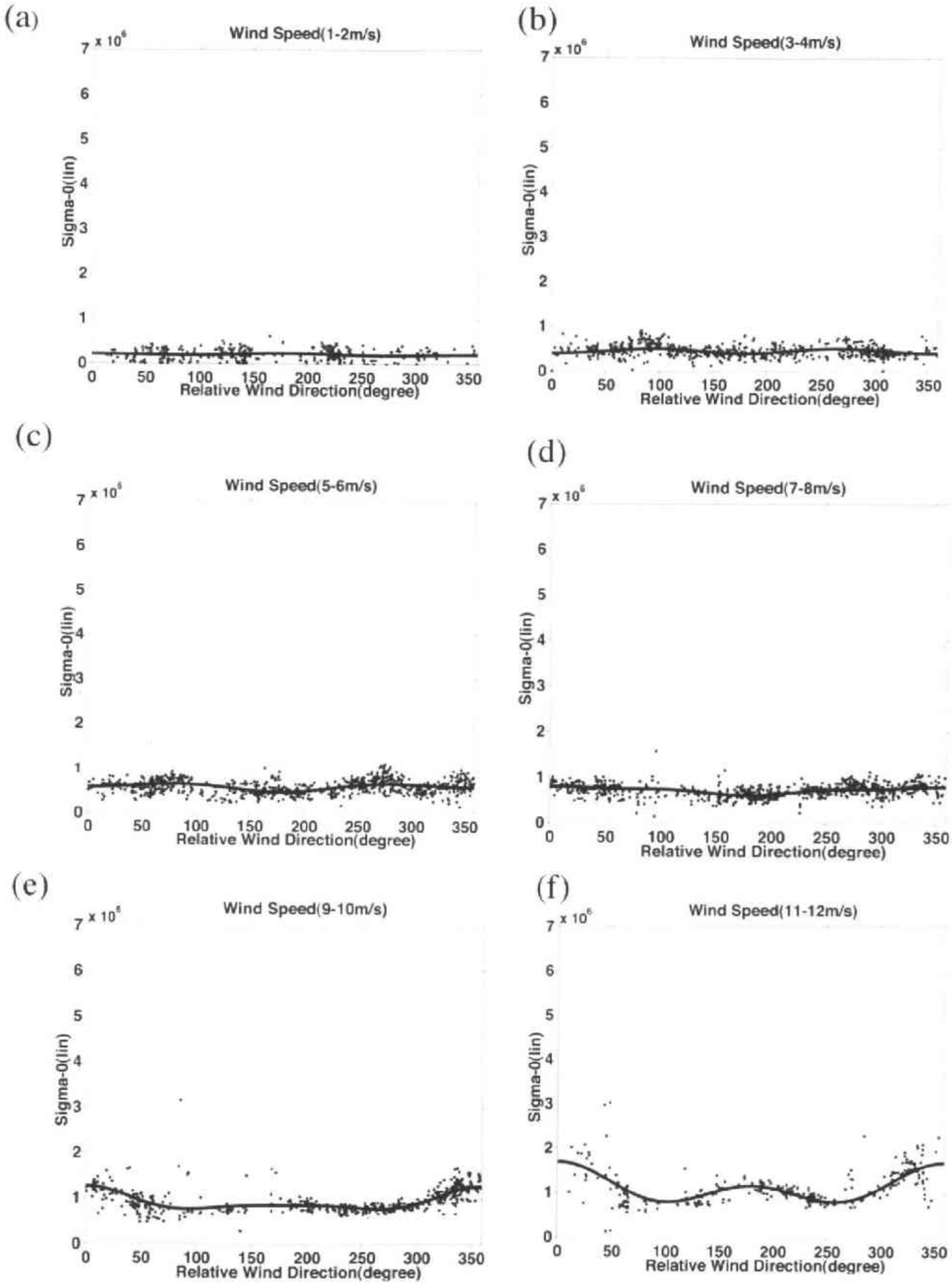

Figure 3.9 Dependence of sigma-0 on wind direction for wind-speed bins, (a) 1-2 m/s to (j) 19-20 m/s. Regression curves are also shown. For wind-speed bins of 15-20 m/s, the regression lines are computed by extrapolating wind speed dependence (see the text).

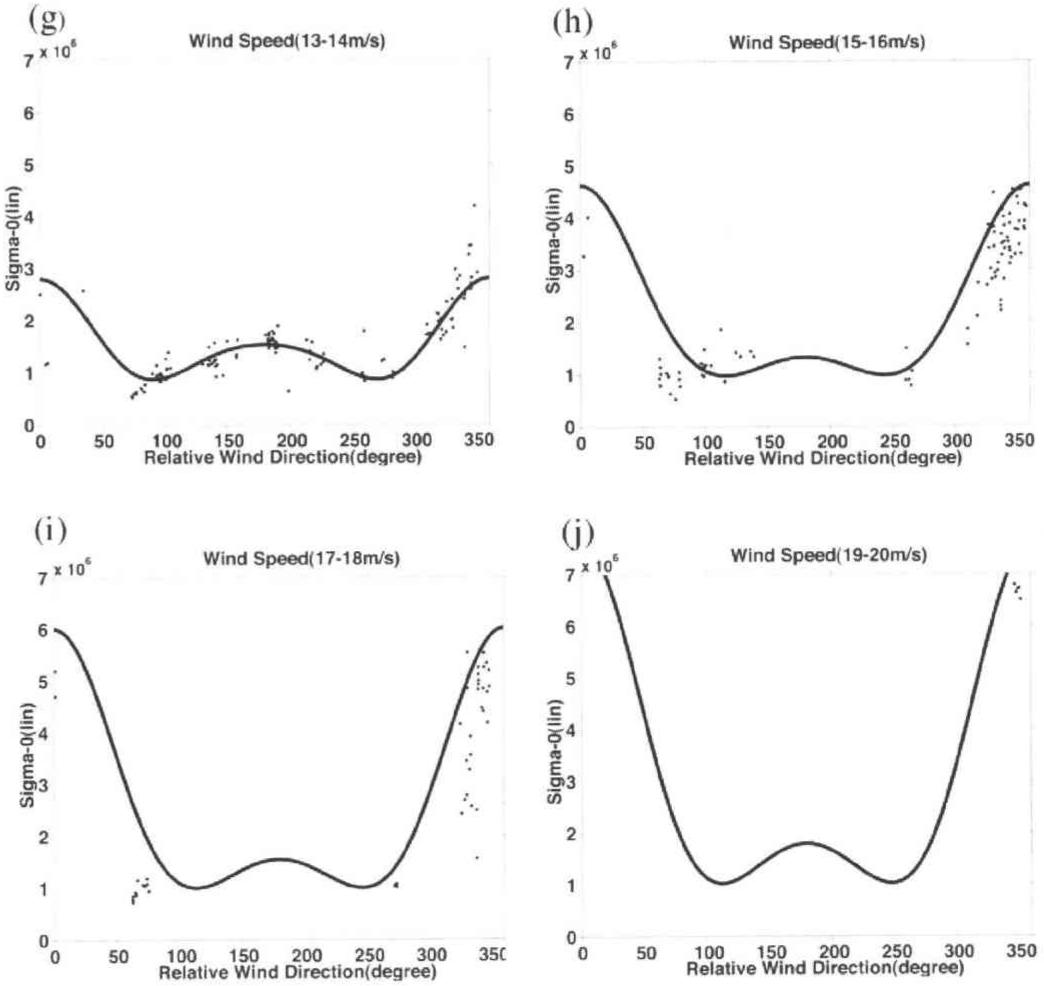

Figure 3.9 (continued)

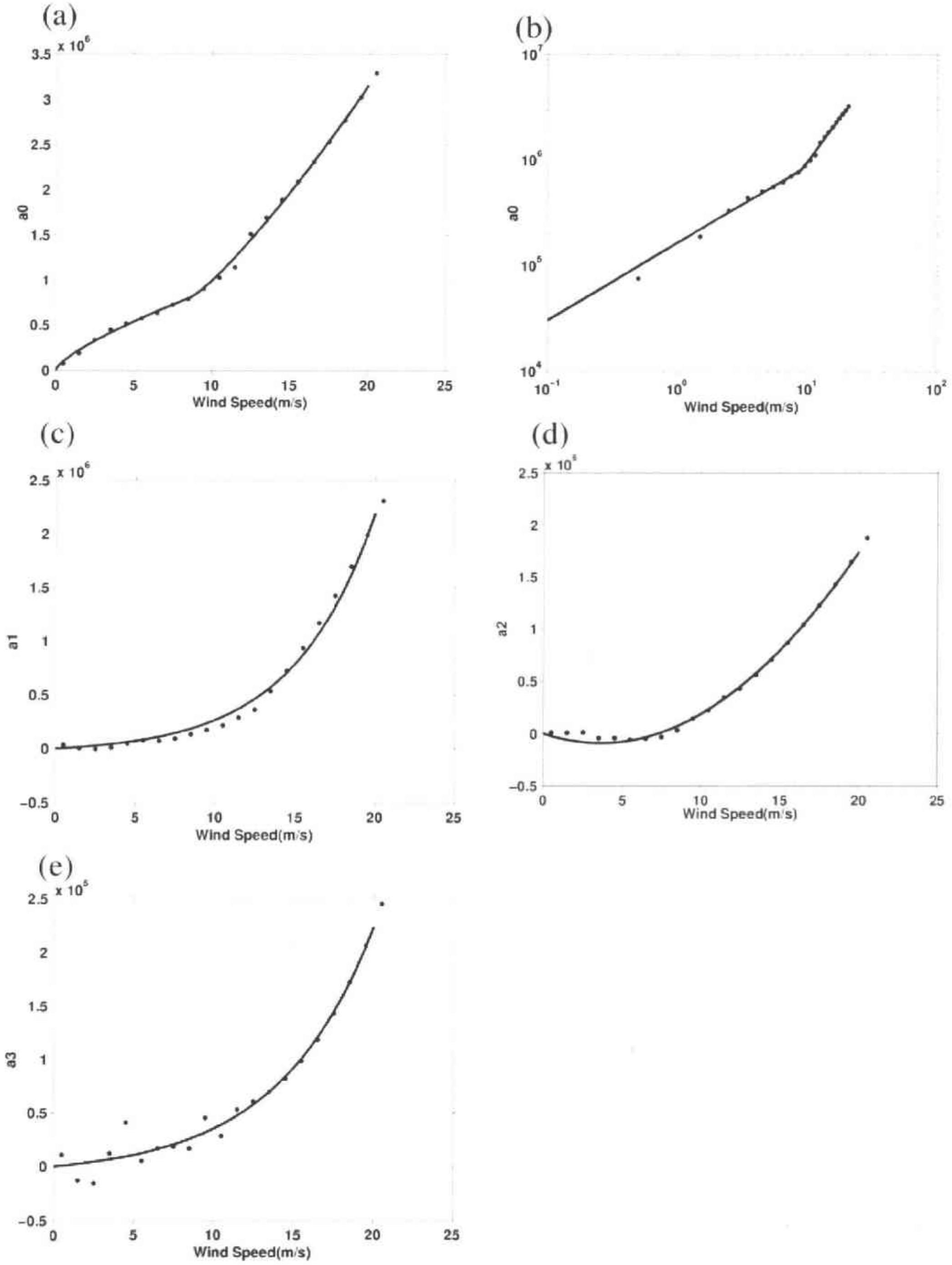

Figure 3.10 Relationships between the regression coefficients and the wind speed. (a) (b) in a logarithmic diagram, (c) , (d) and (e) . The curves representing behavior of the coefficients are also shown (see the text).

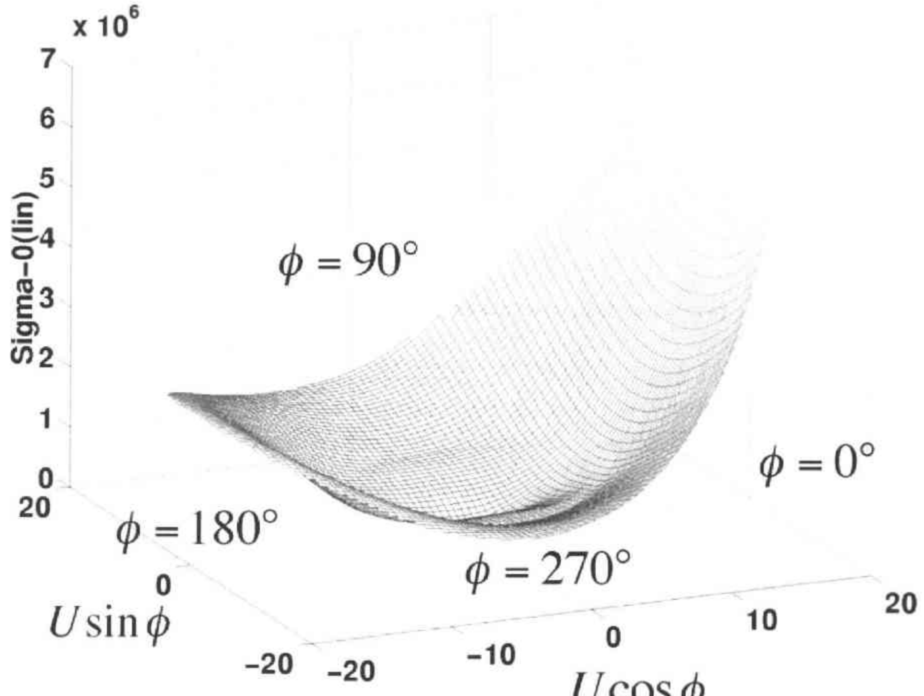

Figure 3.11 A 3-dimensional view of the L-band GMF.

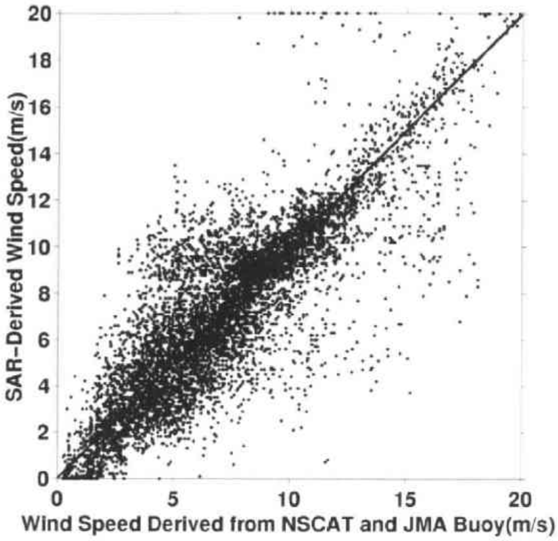

Figure 3.12 Comparison between SAR-derived wind speed and NSCAT and JMA buoy wind speeds. The root mean square error is 2.09 m/s and the bias is -0.0006 m/s.

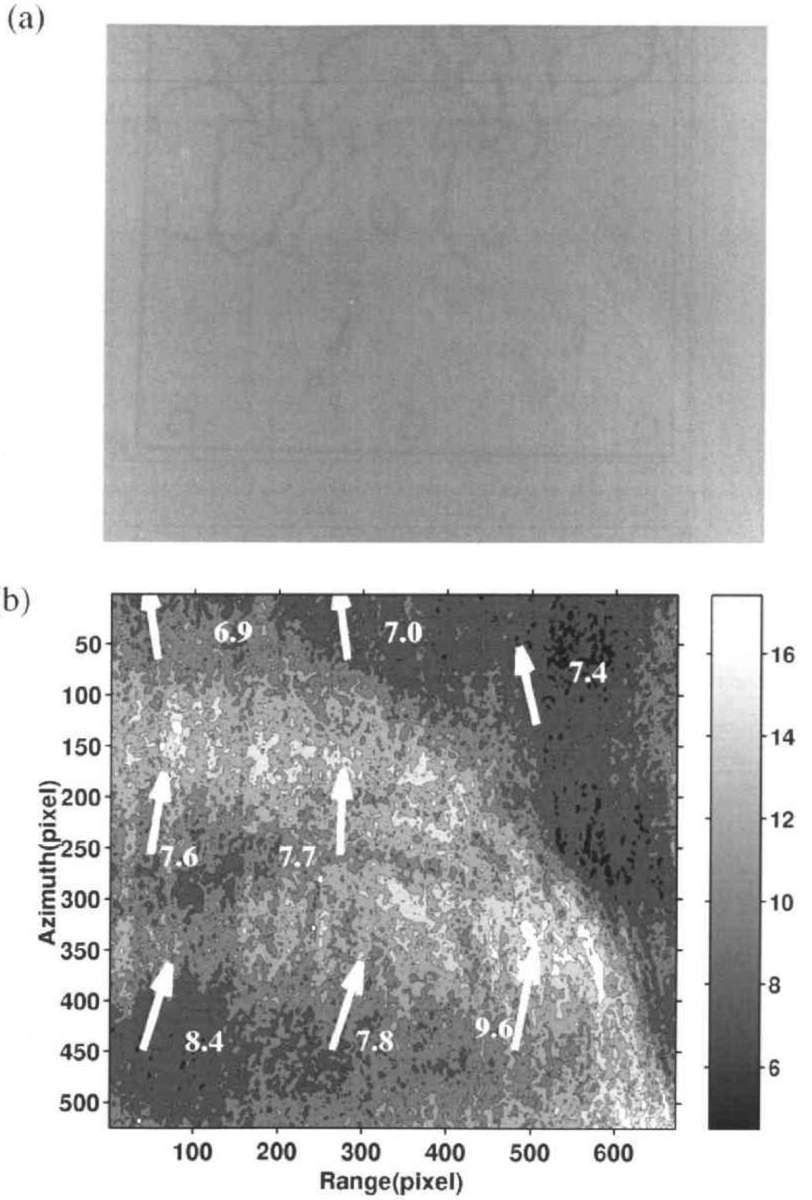

Figure 3. 13 (a) JERS-1 SAR image of the Pacific on May 18, 1997. (b) Wind map derived from the JERS-1 SAR image of (a). The arrows show the NSCAT wind vectors and the value is its wind speed.

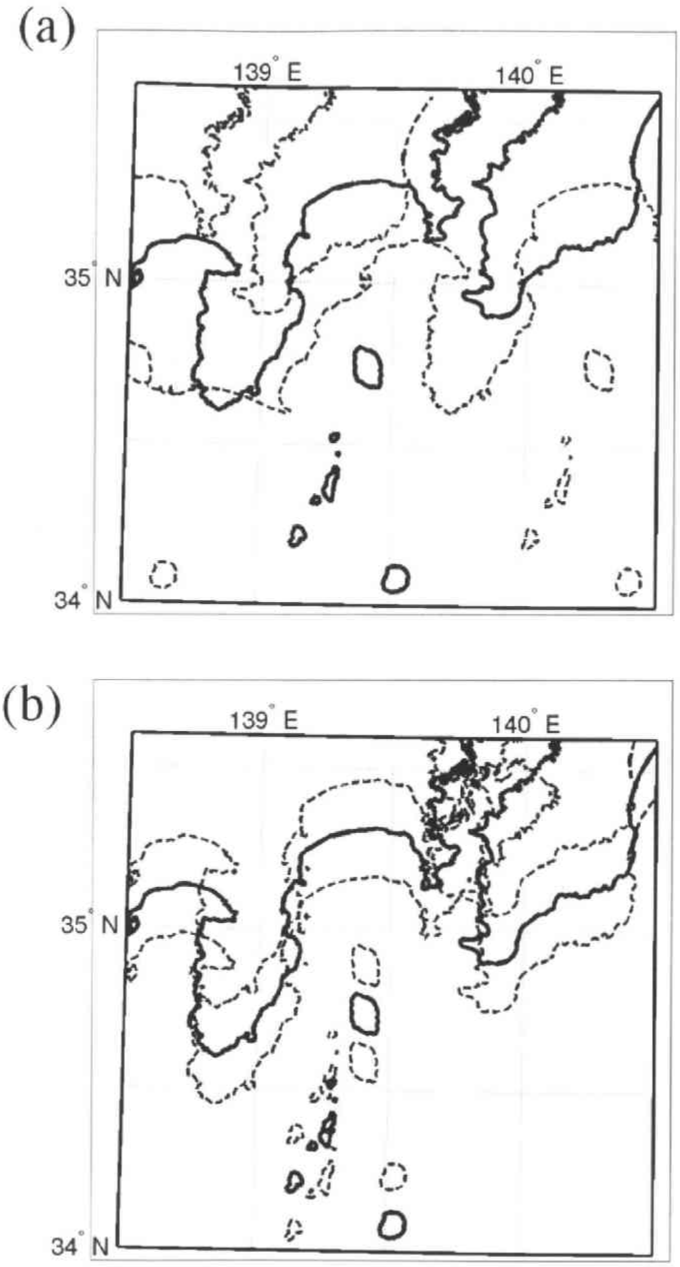

Figure 3.14 Schematic locations of (a) range and (b) the first azimuth ambiguity folded from the land around the Sagami Bay.

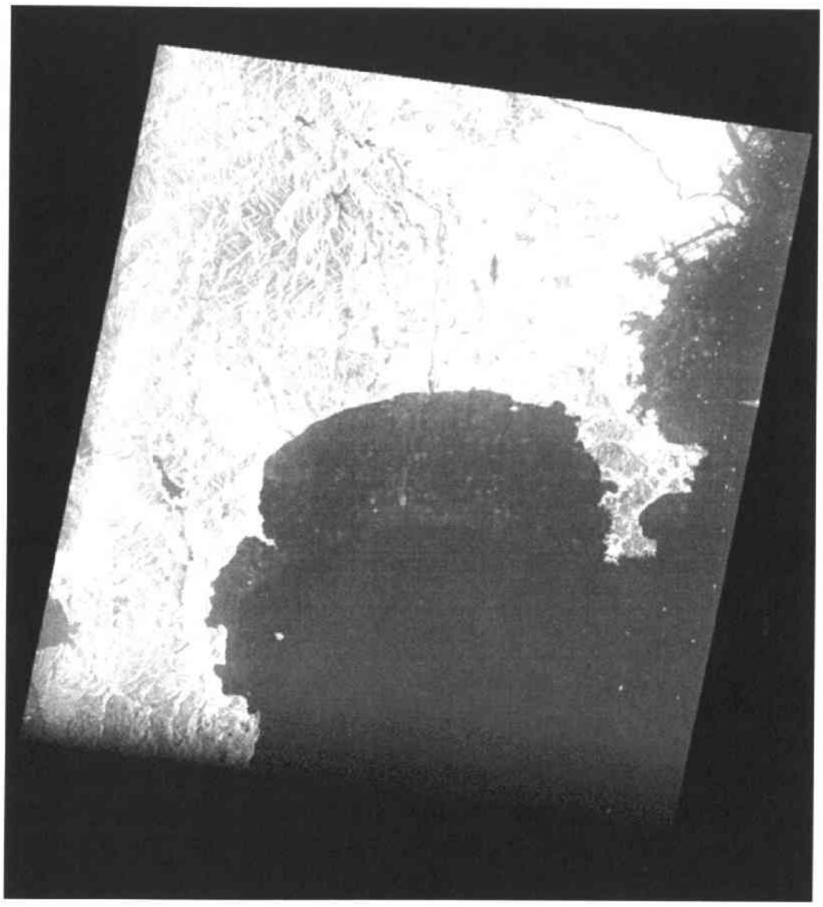

Figure 3.15 An example of JERS-1 SAR image of the Sagami Bay on 22 April, 1992.

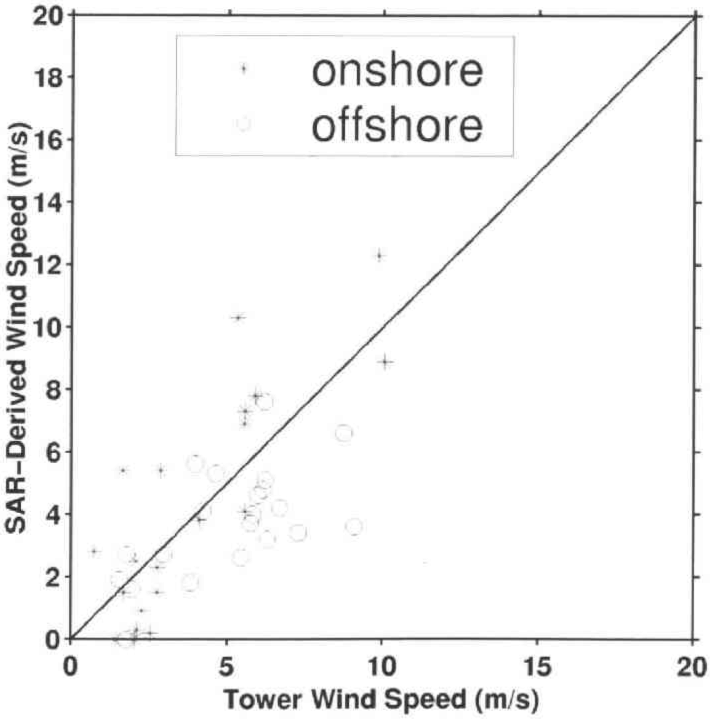

Figure 3.16 Comparison of the ERS-1 SAR-derived wind speeds with those observed by the Hiratsuka Tower 1 km off the coast.

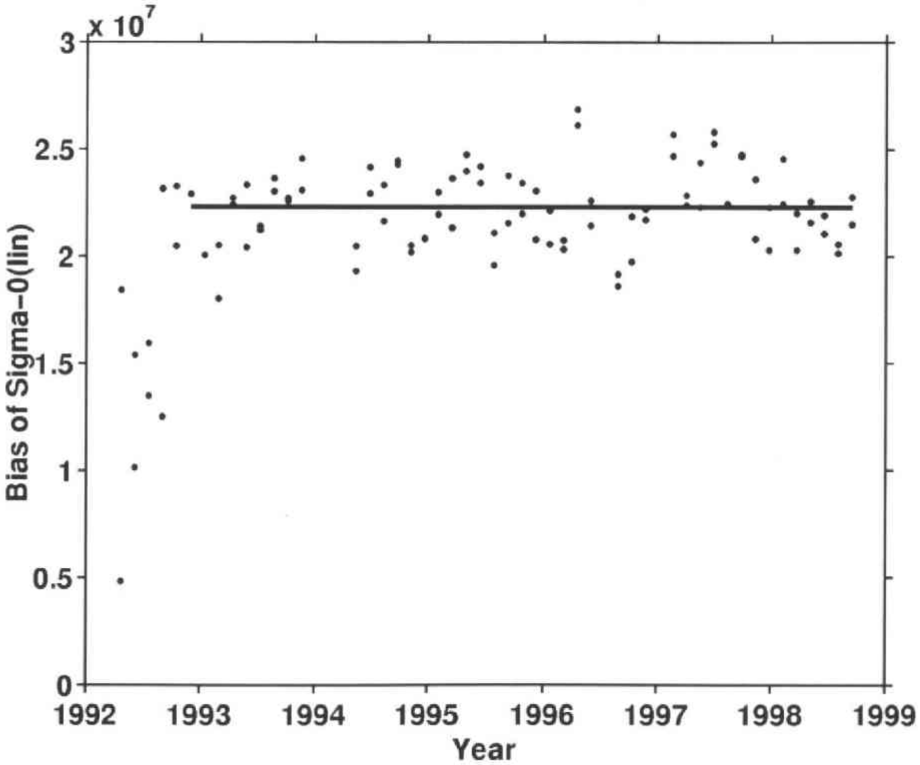

Figure 3.17 The difference of the sigma-0 at the Hirastsuka tower observed by JERS-1 SAR and estimated sigma-0 by the L-band model function using the wind speed and direction at the tower. Solid line shows the mean level of sigma-0 during the operational mode period of JERS-1 SAR.

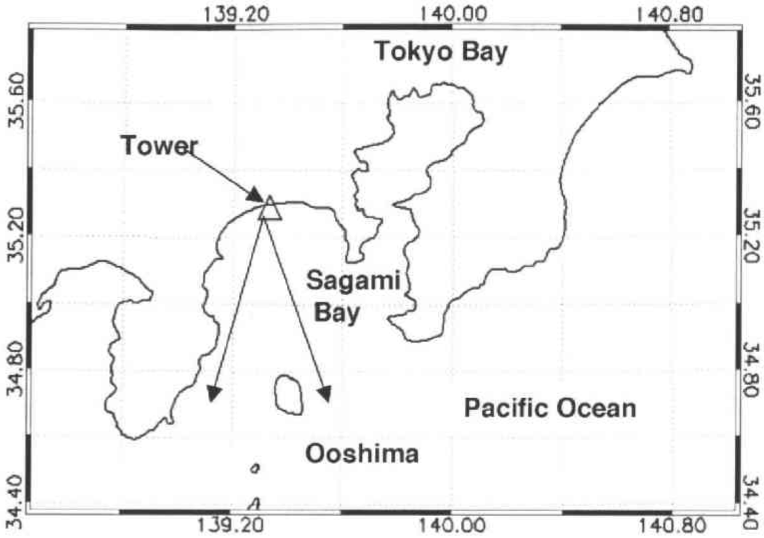

Figure 3.18 Geographycal locations of the Hiratsuka tower (triangle). In case winds are blowing from north, profiles of JERS-1 SAR sigma-0, ERS SAR NRCS, and wind speeds are obtained in the area which are indicated between two arrows.

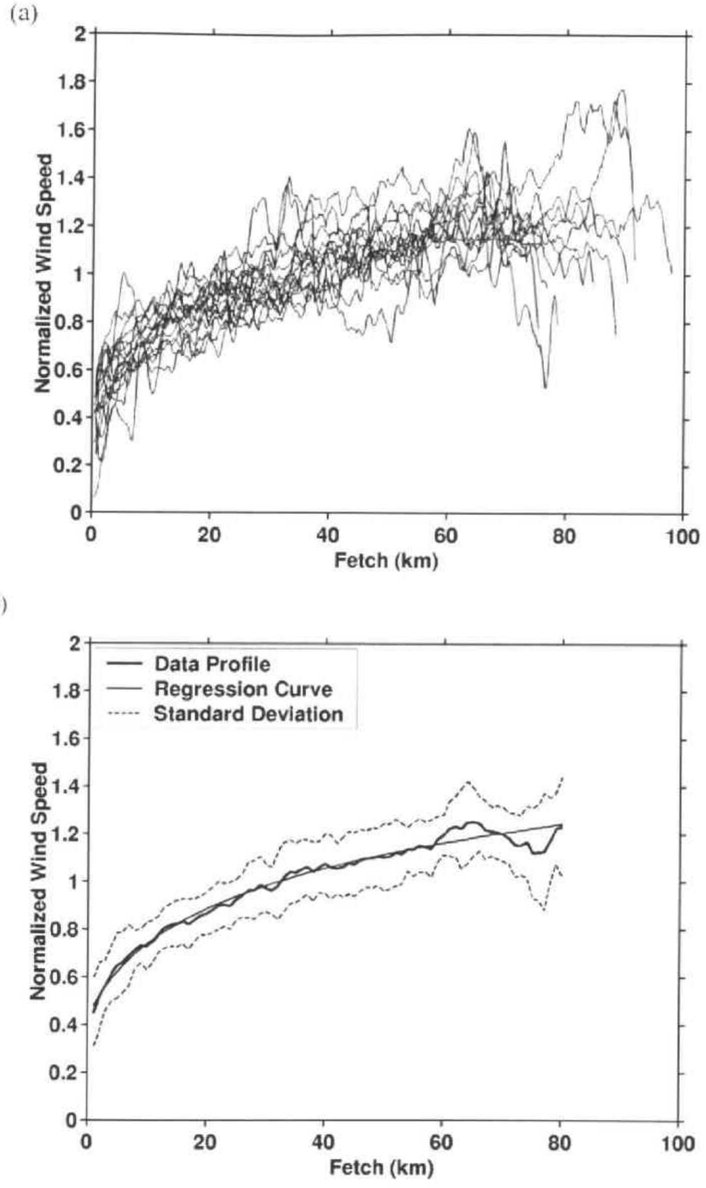

Figure 3.19 Variation of wind speed with offshore distance derived from ERS-1 SAR. (a) All profiles of wind speed in northerly wind cases. (b) The mean profile normalized by mean wind speed (thick solid line) and its standard deviations (broken lines). In the figure, the simply formulated mean normalized variation of wind speed with offshore distance (thin solid line) is also shown.

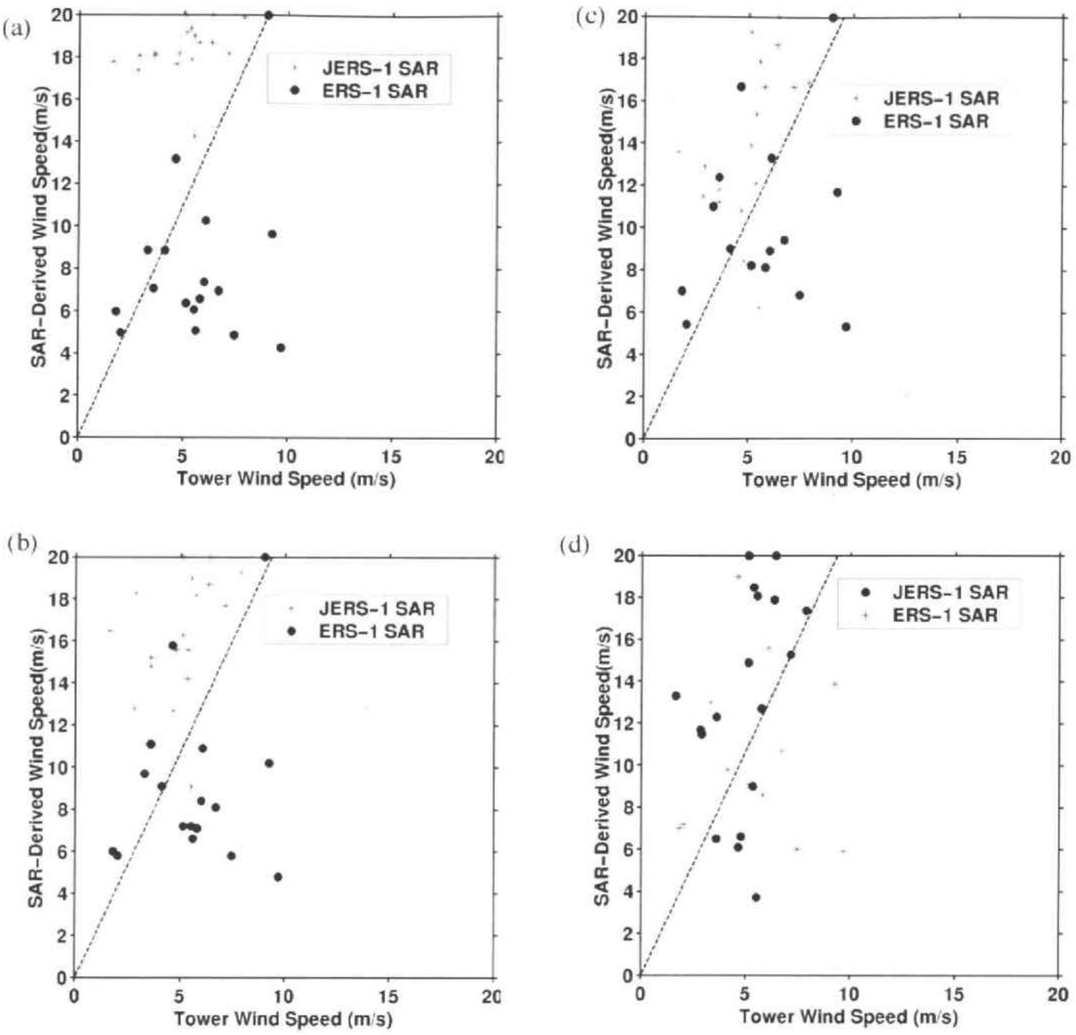

Figure 3.20 Comparison of SAR-derived wind speeds at the distance of (a) 20 km, (b) 32 km, (c) 44 km and (d) 55 km with the tower wind speeds for JERS-1 SAR and ERS-1 SAR.

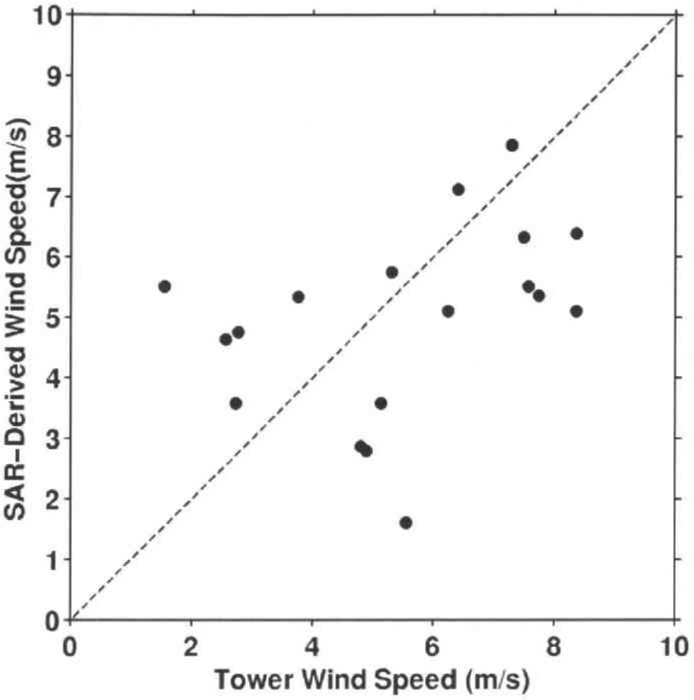

Figure 3.21 Comparison of the wind speeds estimated from the JERS-1 SAR images at the distance of 1 km with the tower wind speed. These wind speeds are derived from the wind speed growth formula and JERS-1 SAR-derived wind speeds at the distance of 55 km.

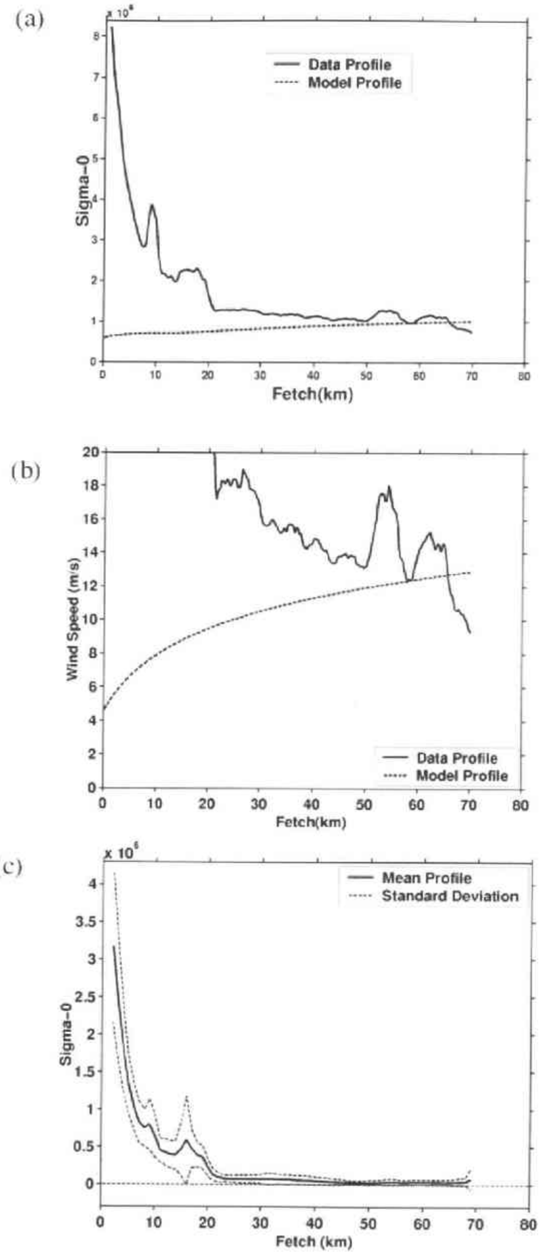

Figure 3.22 (a) Profiles of the observed sigma-0 (solid line) and the expected sigma-0 (See the text). (b) Profiles of wind speeds derived from observed sigma-0 and the wind speed profile derived from wind speed growth formula. (c) Mean difference between sigma-0 observed by the JERS-1 SAR and derived profile by the wind speed growth formula (solid line). Two broken lines of a standard deviation are also shown.

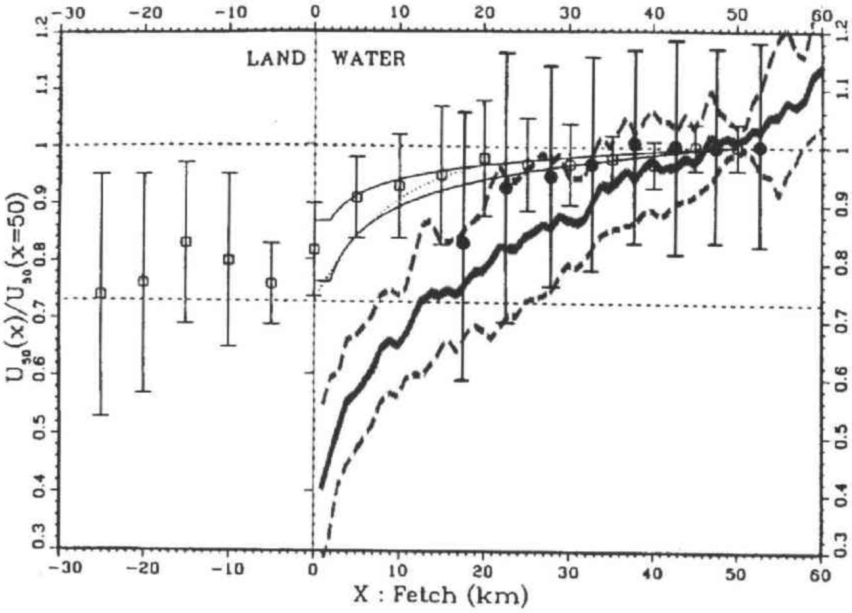

Figure 3.23 Comparison of the variation of wind speed derived from the previous studies and the present study. (black circle: [Ebuchi et al.,1992], square: Smith/Macpherson Field Data [Smith and MacPherson, 1987], thin dotted line: Smith/Macpherson Empirical Fit [Smith and MacPherson, 1987], thin solid line, Taylor/Lee Guidelines[Taylor and Lee,1984], broad solid line and broken lines are the mean and the standard deviations obtained in the present study) Original figure is sited from [Dobson et al.,1989] and [Ebuchi et al.,1992].

4 Statistics of high-resolution coastal winds derived from SAR

4.1 Introduction

Results derived from the open ocean are not generally applicable to the coastal seas [Hsu, 1988]. One of the major factors is high variability of surface coastal winds. It is quite a contrast to winds over open ocean. Coastal winds are affected by thermal contrast between land and sea, orographic forcing, and changes in surface roughness (Chapter 1). Thus, wind changes its nature drastically in coasal zones. This offers an essential key to an understanding of atmospheric and oceanic phenomena in coastal zones. However, we have not fully grasped coastal winds because of a lack of wind observation systems with high-resolution sufficient to resolve coatal winds.

In this regard, SAR is an excellent candidate instrument for capturing coastal wind fields. SAR wind retrieval by geophysical model functions enables us to convert SAR images into the high-resolution surface wind speed maps [e.g., Scoon et al. 1996]. SAR has been verified to be especially feasible because of its high resolution. In fact, only SAR can resolve local variations of coastal wind fields with high spatial resolution. However, we have just individually illustrated coastal winds from case studies [e.g., Sandvik and Furevik, 2002].

Therefore, it is worth understanding coastal winds resolved by SAR from statistical point of view. A considerable number of studies have been made on it to compose climatological charts of wind over both land and ocean [e.g. Pavia and O'Brien, 1986]. Recently, scatterometer wind observations are more available and contribute to the global/regional wind climate studies in open seas. However, little attention has been given to the point of the coastal wind climatology or statistics and wind intergradation between land and open ocean.

In this study, we present statistics of high-resolution coastal winds derived from SAR. It is possible to characterize the results of the present study as definition of "coastal" from wind distribution point of view. In order to give statistical description of wind speeds, we use, as a simple measure, the surface wind speed probability distributions as a simple measure. In the following section, datasets used in the present study are listed. The statistical features of surface wind speed probability distributions are investigated in Section 4.3. Section 4.4 further illustrates sea surface wind variability. Discussion and summary are given in Sections 4.5 and 4.6, respectively.

4.2 Surface wind datasets

We select the study area around Japan ($20° - 50°N, 120° - 160°E$, Figure 2.2 (a)). It covers the northwest Pacific Ocean, the Japan Sea, the East China Sea, the Sea of Okhotsk, and the Japanese archipelago. The Eurasia continent is checked off in the present study. The Japanese archipelago has long coastlines and the associated waterways, embayments, and estuaries. In addition, land and seas in the study area are under the same weather and climate systems.

We used the following surface wind observations in the area. They are summarized in Table 4.1. The surface winds monitored by the AMeDAS over the Japanese archipelago are used (Section 2.2.1). We use sea surface wind measurements from three JMA buoys (Section 2.2.2), a buoy in Mutsu Bay (Section 2.2.4), Hiratsuka Experimental Station (Section 2.2.3), QuikSCAT (Section 2.1.2), and ERS-1/2 SAR-derived winds. Figure 4.1 shows distributions of the ERS-1/2 SAR observation sites and the numbers of images. A total of 6, 567 scenes are used. Most of them cover the nearshore resions around Japan. There are no differences between the climatological monthly numbers of the SAR images (not shown). Wind-speed maps with 1×1 km grid size are derived from the averaged SAR images by applying SAR wind retrieval using CMOD IFR2 model function [Quilfen et al., 1998] and wind direction data from NCEP/NCA reanalyses. It is assumued that wind direction is uniform over the sea in a SAR image. Figure 4.2 shows an example of a part of an original SAR image and the SAR-derived wind speed map. An examaple of wind speed distribution of the SAR-derived wind speed map is also shown in Figure 4.2 (c).

4.3 Probability distributions of surface wind speed over land and sea

4.3.1 The Weibull distribution and its parameter derivation

We classify probability distributions of wind speed over land and sea, and examine the representative features of the categorized groups. It has been shown that Weibull distributions give good fit to observed wind speed probability distributions [e.g. Justus et al., 1976]. Therefore, we classify wind speed probability distributions in a feature space of two parameters of Weibull distribution.

The Weibull probability density function (pdf) of a random variable x is expressed as below:

$$pdf(x)=\frac{\gamma}{\phi}\left(\frac{x}{\phi}\right)^{\gamma-1}\exp\left[-\left(\frac{x}{\phi}\right)^{\gamma}\right] \quad . \tag{4.1}$$

The parameter ϕ is a scale parameter with the same dimension as x. It is a measure of the mean of a set of x. The paramter γ is the dimensionless shape parmeter. It is inversely related to the variance of a set of x. The two Weibull parameters are estimated from a histgram of x through a maximum likelihood method.

In advance, except for SAR, we construct year-round climatological wind speed distributions from time-series wind observations of in situ datasets. For QuikSCAT, we obtain a set of wind speed acquired in grid cells with $0.25° \times 0.25°$ in the study area. The datasets roughly correspond to 12 hourly time-series wind measurements at the grid cell. Then, we estimate pairs of two Weibull parameters from the wind speed distributions. Figure 4.3 shows an example of wind speed distribution from Hiratsuka tower wind measurements and the estimated Weibull distribution.

In order to compensate the lack of time-series wind measurements over the nearshore seas and to obtain a statistically significant view of the winds nearshore, we use the SAR-derived wind-speed dataset. They surely provide only spatial distributions of wind speed at a certain instant. But, we construct wind speed probability distributions from SAR-derived wind speeds based on the following concept.

The wind speed probability distribution reflect the representative wind speeds associated with slowly-varying synoptic weather systems, rather than turbulent with locally-stationary statistical properties. The winds near the coast are strongly influenced by the local thermo-dynamical effects. While the synoptic weather systems are common in the study area, the local effects on winds are quite different from region to region. However, we here consider extracting the representative characteristics of nearshore winds relative to the coastline by excluding the reginal differences of wind variability. Furthermore, we presume that wind valiabilities perpendicular to the coastline is more predominant and representative than alongshore wind valiabilities and regional difference. That is to say, we assume that coastal zones are commonly described using a unique 1D coordinate system with an axis perpendcular to the virtual straight coastline.

Based on the assumption mentioned above, we define virtual zones every 5-km from shore to offshore distance up to 100 km (20 zones in all). We construct a wind speed distribiton using all the SAR-derived wind speeds assigned to each zone according to the offshore distance. Two Weibull parameters are estimated from the wind speed distributions.

4.3.2 Data plot distribution in a feature space of two Weibull parameters

Figure 4.4 shows data plot distribution in a feature space of two Weibull parameters. Plots indicate pairs of two Weibull parameters estimated from different wind datasets. Black solid contours indicate mode wind speeds of the wind speed distributions calculated from a pair of parameters. They helps us guess rough sketch of the pdf.

For AMeDAS, we can find a distinct cluster. The center is at 2.0 of the scale parameter and 1.5 of the shape parameter. Most plots have the scale paramter between 1.0 and 3.0 m/s and the shape parameter between 1.1 and 1.9. These parameters produce wind speed distribution with mode wind speed around 1.0 m/s. A small number of plots has higher values of both parameters. The plots of QuikSCAT also form a distinct cluster in spite of the large areal coverage. The scale paramters range from 6.5 to 11.5 m/s and the shape parameters range from 1.6 to 3.0. The mode wind speed of the distribution ranges from 4.5 to 9.0 m/s. The plots of JMA buoys and a buoy in Mutsu Bay are located in a left lower part of the QuikSCAT cluster. A plot form HES is close to plots of AMeDAS. The SAR plots are located in an area different from the cluster areas of AMeDAS and QuickSCAT. They headed from a plot with the smallest shape parameter to the QuikSCAT cluster with offshore distance.

4.3.3 Mahalanobis distance classifier

In order to give an indication of class (cluster) decision boundaries, we employ Mahalanobis distance (MD) classifier. It is a Euclidean distance normalized by the variance and covariance of the class and defined as:

$$\text{Mahalanobis distance} = \left(X - M_c^T\right)V^{-1}\left(X - M_c\right) \tag{4.2}$$

where:

c is a particular class,
X is the measurement vector of a candidate data plot,
M_c is the mean vector of the parameters of class c,
V is the covariance matrix of the parameters of class c, and
T is transposition function.

Here we tentatively classify the plots in the Weibull parameter feature space into three clusters: Land cluster (AMeDAS plots), Open Ocean cluster (QuikSCAT plots and JMA buoy plots) and Coastal Sea cluster (plots of SAR, Hiratsuka Experiment Station and Mutsu buoy). In Figure 4.4, the dashed contours with different colors indicate the MDs from each cluster centers. All two clusters boarder on with the same value MD isolines from outside of them each other. This means that the tentative classification is reasonable. Moreover, considering two contacts of Land and Coastal Sea clusters and Land and Open Ocean clusters, we can delimit the area over land and sea surface with a gray line.

4.3.4 Typical wind speed distributions assigned to Land, Open Ocean, and Coastal Sea clusters

In Figure 4.5, we show typical wind-speed distributions using the mean Weibull parameters assigned to three clusters. The parameters correspond to the values at the centers of MD cotours. The Land distribution (Green) has high frequencies in lower wind speeds and quite low frequencies in the range higher than about 6 m/s. The Open Ocean distribution (Bule) has high frequencies in the wind-speed range around 8 m/s and extend up to 20 m/s. The Coastal Sea distribution (orange) has the peak frequency at around 3 m/s though the peak value is lower than that of the Land one. It has frequencies in a wide wind-speed range up to 20 m/s as well as the Open Ocean distribution has.

In order to examine the transition of wind in the coastal zones, we reproduce wind speed distributions by mixing the typical wind speed distributions assigned to Land and Open Ocean at a given rate. The two distributions are shown in Figure 4.5. First, we generate random numbers from the two Weibull distributions, and mix them at given rates. Then, we estimate two Weibull parameters from the mixed distribution. They are shown by a pinck curve in Figure 4.6 together with mixing ratios. It is shown that the SAR plots are located close to the pink line, and that the the plots near the central part of the Coastal Sea cluster are reproduced by mixing of the typical Land and Open Ocean wind speed distributions at a ratio of 3 to 7.

4.4 Statistics of spatial wind variability

We investigate the spatial valiability of wind speed using SAR-derived wind speed maps. The method is as follows. First, we divide each SAR-derived wind speed map into subregions. They are 10-km squares, which are chosen through traials as the wind speed distribution becomes close to Gaussian distribution. Then, we derive the offshore distance from the nearest coast to the center of each subregion. Standard deviation and skewness of wind speed in the subregions are caluculated. They are defiend as;

$$\text{Standard Deviation} = \sqrt{\frac{1}{N}\sum_{j=0}^{N-1}\left(x_j - \bar{x}\right)^2} \tag{4.3}$$

$$\text{Skewness} = \frac{1}{N}\sum_{j=0}^{N-1}\left(\frac{x_j - \bar{x}}{\text{Standard Deviation}}\right)^3 \tag{4.4}$$

where N is the number of samples, x_j is wind speed, and $\bar{x}$ is mean wind speed. We tested several scales from 5 to 20 km but general tendencies are almost the same. We consider that these statistical parameters are representative of wind variability according to offshore distance.

Figure 4.7 (a) and (b) show frequency distributions of standard deviations in bins of 0.1 m/s and 1 km and skewness in bins of 0.1 and 1 km, respectively. Note that the plots with the offshore distance beyond 150 km are projected on the axis of 150 km, and that the number of data with offshore distance around 100 km is small because most images of ERS-1/2 SAR with 100 km swath are acquired around nearshore region. In every wind speed range, the same characteristics as described below are seen.

As shown in Figrue 4.7(a), the distribution of standard deviation ranges widely up to 4 m/s within the distance of 20 km. However, upper bound of standard deviation decreases with offshore distance. Beyond the distance of 100 km, it becomes constant. Its value is less than 1.5 m/s and smallr than the root mean square error of the SAR-derived wind speeds.

For the skewness (Figrue 4.7(b)), within the distance of 10 km, the distribution is widely spread and ranges from –3.0 to 4.0. The whole distribution deviates to the positive side, and it means that the wind speeds are rather concenterated in the lower wind speeds. Upper and lower bounds of the skewness distribution decrease with the offshore distance. Beyond the distance of 50 km, the positive deviation of distribution disappears. Beyond the distance of 100 km, the upper and lower envelopes have constant values.

4.5 Discussion

4.5.1 Characteristics of wind speed probability distributions

In Figure 4.4, some of the AMeDAS plots deviate away from the Land cluster center. They have the larger scale parameters. Through cearful investigation, we confirm that most of them are in near coast plains. In such regions, winds over land come under influence of that over the nearshore seas. Therefore, it might be true that we should define coastal zone as extending areas to either side of the coastaline from the wind speed distribution point of view. It also is shown in [Watebe et al., 1996] that the surface winds observed at the HES is highly correlated with that in the neighboring land.

The QuikSCAT plots seem to form several different clusters, and it may reflect the regionality of seas. It must be interesting to consider the reagionality of sea surface wind. This is left for future studies.

Wind speed distributions assigned to Coastal Sea cluster have two features (Figure 4.5). One is that the frequencies of lower wind speeds are high. The followings contribute to this characteristic: evolutions of the internal boundary layer under offshore wind; wind shadows with different scale; and a deceleration of wind flow blowing toward high land topography. Another important feature is that it has frequencies in a wide wind-speed range up to 20m/s. It can be considered mainly due to the sea surface roughness smaller than the land surface roughness. Furthermore, locally formed strong surface winds under the orograhic influences, such as downslop lee winds, gap winds and barrier jets (Table 1.1) may play important rules to widen the histogram to the higher wind-speed range.

4.5.2 The boundary between the coastal sea and open ocean

Note that upper bounds of standard deviation and skewness are function as offshore distance (Figure 4.7). These results show that large variations of wind speed can occur in the small regions of 10-km square in nearcoast seas. Of course, orografically modified winds are observed by scatterometer with a scale up to several hundred kilometers. When comparing with them, the gradient of wind will be one of the important factors. Based on the above results, we may conclude that, from wind speed variability point of view, the distance of 100 km forms the division between coastal seas and open ocean. In other word, locally strong and lower wind regions are subject to be produced in the area within the distance of 100 km from the coast.

4.5.3 Wind speed probability distributions using SAR-derived wind speeds

SAR wind retrival using the CMOD wind retrieval algorithm has a reported operational range of 2-24 m/s [Carswell et al., 1999]. It is generally said that the lower threshold is abount 2 m/s. Though SAR wind retrieval under wind speed of 2 /ms is open to question, it is an indisputable fact that the wind speeds lie between 0 and 2 m/s. In the present study, we deal with histogram of wind speed with a 1-m/s interval class. Therefore, it does not affect the shape of the histogram very much.

4.6 Summary

We statistically investigate characteristics of winds over land and sea. High-resolution winds derived from SAR give a new picture of coastal winds.

1) We construct wind speed probability distribution from different wind datasets including SAR, and estimate the Weibull parametes. In a feature space of the Weibull parameters, we can identify three representative clusters assigned to Land, Open Ocean, and Coastal Sea.

2) The typical distribution of wind speed assigned to Land cluster has high frequencies in lower wind speeds and quite low frequencies in the range higher than about 6 m/s. The typical distribution of wind speed assigned to Open Ocean cluster has high frequencies in the wind speed range around 8 m/s and extend up to 20 m/s. The typical wind speed distribution of wind speed assigned to Coastal Sea cluster has the peak frequency at around 3 m/s though the peak value is lower than that of the Land one. It has frequencies in a wide wind-speed range up to 20 m/s.

3) Wind speed distributions assigned to Coastal Sea cluster are can be reproduced by mixing the typical wind speed distributions assigned to Land and Open Ocean clusters at a given rate. The mixing ratio to reproduce the typical wind speed distribution of Coastal Sea cluster is 3 to 7.

4) We investigated spatial wind valiability using standard deviation and skewness estimated from the SAR-derived high-resolution wind-speed maps. Their distribution ranges decrease with offshore distance from the coast to 100 km offshore. This suggests that the offshore distance of 100 km can be a measure of separation scale between the coastal sea and open sea.

Table 4.1 Surface wind observations used in the present study.

Data	Horizontal resolution	Temporal resolution	Data period	Site	Climatology
AMeDAS			1990-2000	840 stations in Japan	10-year climatology
JMA buoys	a fixed point	1	1994-1999	3 buoys around Japan (Figure 2.2)	5-year climatology
Hiratsuka Experiment Station	a fixed point	3	1990-2000	Sagami Bay (Figure 2.2)	10-year climatology
Mutsu buoy	a fixed point	1	1990-2000		10-year climatology
QuikSCAT	0.25 deg.	1	2000-2002	13,758 cells (20-50° N, 120-160° E)	3-year climatology
ERS-1/2 SAR	1.0 km	-	1991-2001	(Refer to Figure 2.2 and text)	See text for details

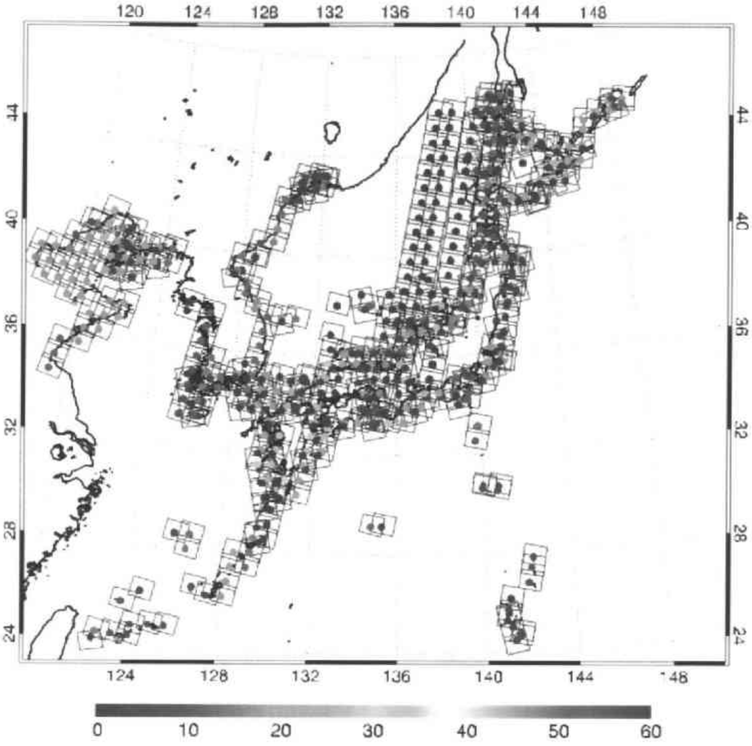

Figure 4.1 Observation sites and numbers of SAR images. Frames show SAR observation areas. The numbers of SAR images at the sites are indicated with color circles in the frames.

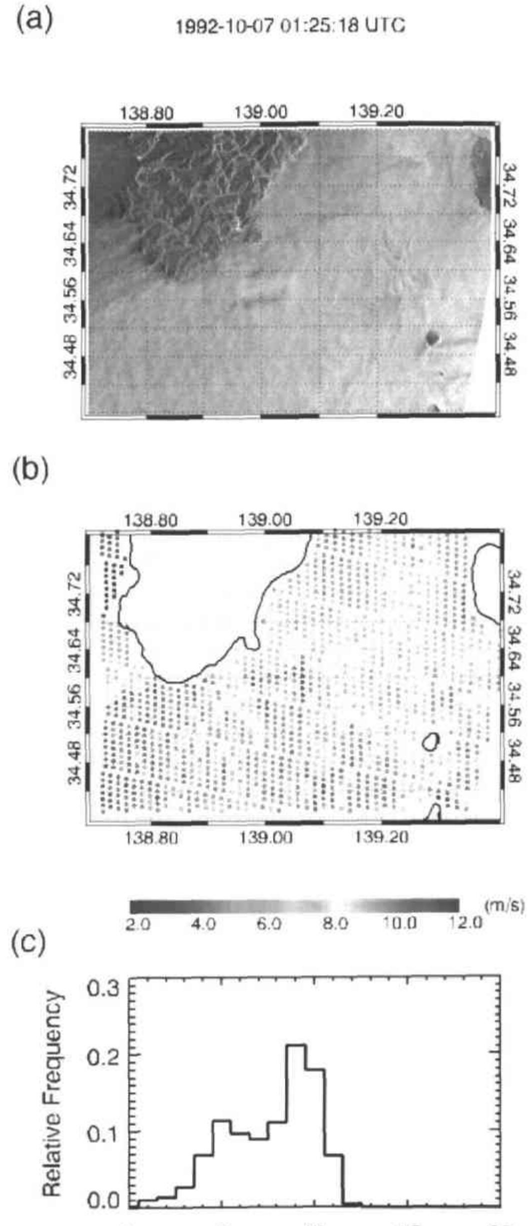

Figure 4.2 An example of SAR-derived wind fields. (a) A part of SAR image acquired at 01:25 UT, October, 7, 1992. (b) Wind speeds with 1-km grid retrieved from the image shown in (a). (c) Wind speed histogram of the SAR-derived wind speeds in (b).

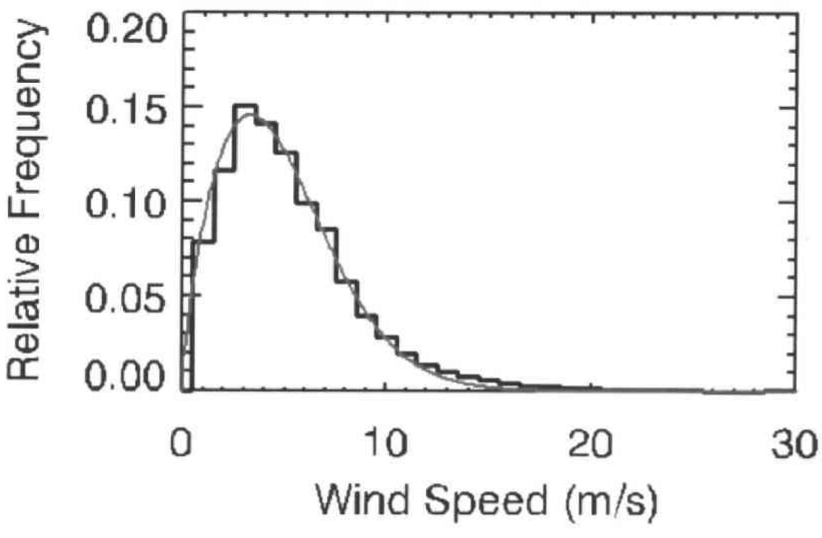

Figure 4.3 An example of wind speed distribution (black line) and the estimated Weibull distribution (red line). The wind data is from Hiratuska Experimental Station observations.

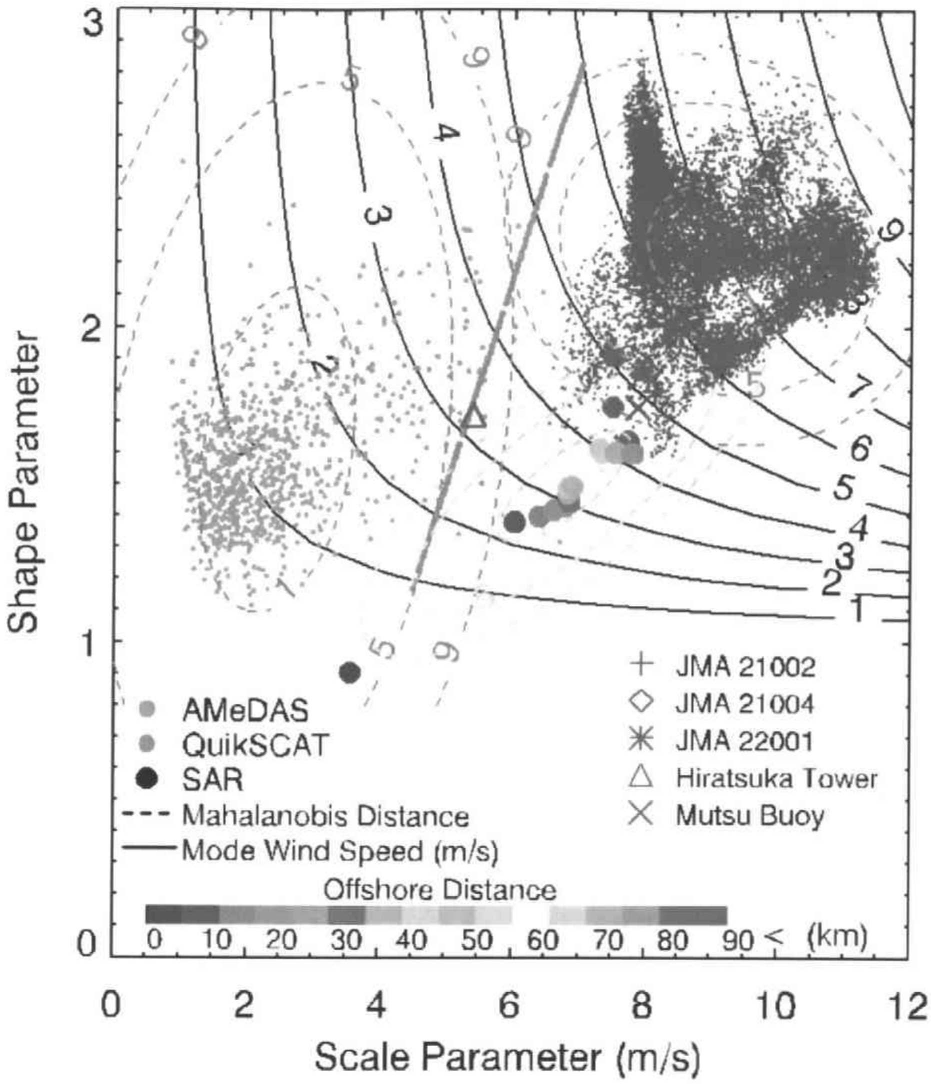

Figure 4.4 A feature space of two Weibull parameters. Plots are sets of Weibull parameters derived from different wind datasets. They are plotted by different symbols and colors. Solid contours indicate mode wind speeds derived from a pair of two Weibull parameters. Three dashed countours for each clusters are isolines of Mahalanobis distances. Green and blue isolines of Mahalanobis distance are derived from AMeDAS and QuikSCAT plots, respectively. Orange isolines are from plots of SAR, Hiratsuka Experiment Station, and a buoy in Mutsu Bay. Gray line shows the boundary of wind speed distributions on land and sea (see text).

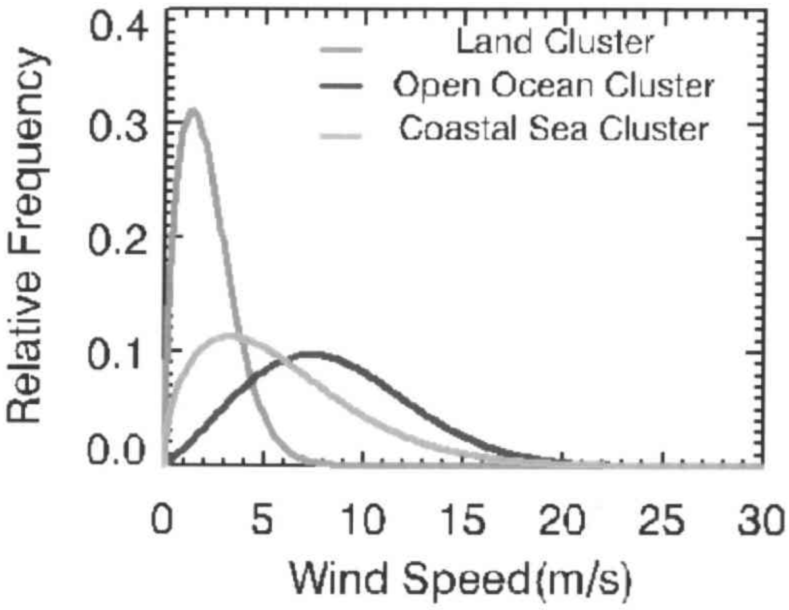

Figure 4.5 Typical wind speed distributions assigned to three clusters: Land cluster (green); Open ocean cluster (blue); and Coastal cluster (Orange).

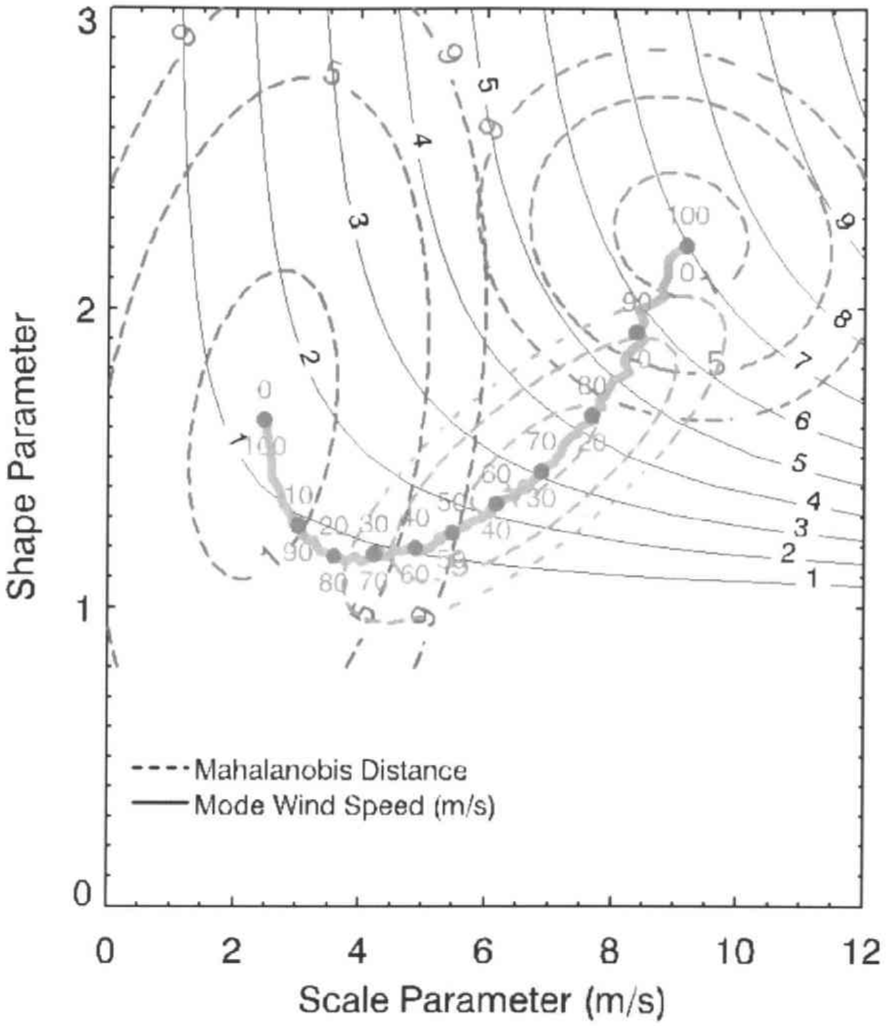

Figure 4.6 A feature space of two Weibull parameters. As well as Figure 4.3, solid black contours of mode wind speeds, and three dashed isolines of Mahalanobis distances for three specified clusters defined in Figure 4.3 are depicted. A pink curve indicates a pair of two Weibull parameters estimated from a mixed wind speed distribution, which is made from typical wind speed distributions assigned to Land and Open Ocean clusters. Green and blue numbers indicate the mixing percentages of Land and Open Ocean, respectively.

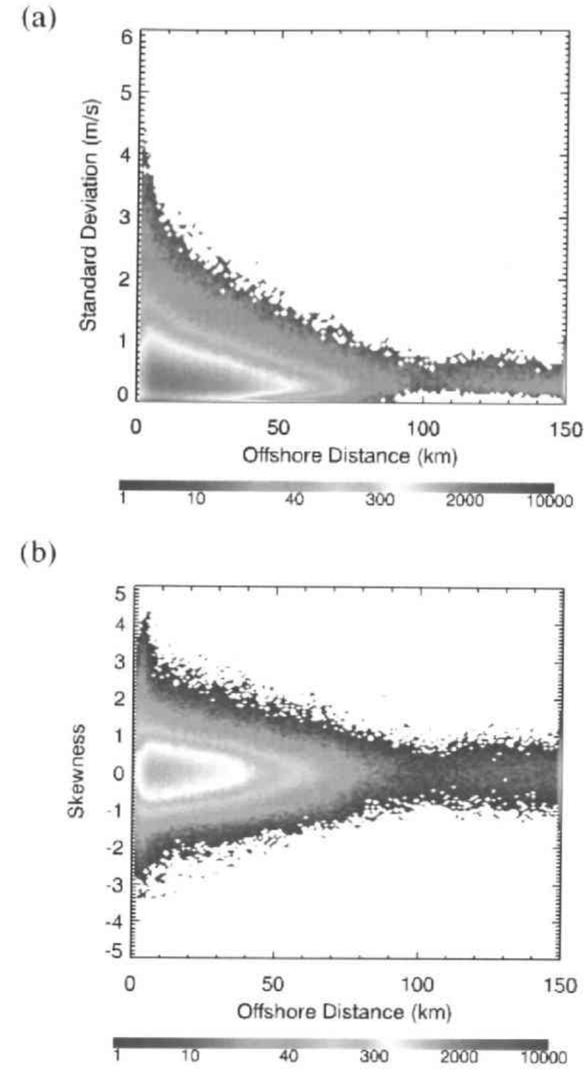

Figure 4.7 (a) Standard deviation and (b) skewness of SAR-derived wind fields in a 10-km square as a function of offshore distance. The number of samples in a bin of 0.1 m/s and 1 km for standard deviation and in a bin of 0.1 and 1 km for skewness is indicated by color.

5 Coastal winds and wind waves observed by active satellite sensors

5.1 Introduction

SAR has revealed finer structures and higher variability of coastal winds in many studies [e.g., Sandvik and Furevik, 2002] and the peculiarily of coastal winds are statistically shown in Chapter 4. In turn, wind waves are directly affected by such ocean surface winds. However, the detailed air-sea-land interaction processes involved in coastal zones are not well understood largely because of a lack of accurate, high-resolution, extensive wind and wave measurements. In concrete term, it is not well understood how finer-scale wind variations are related with offshore wind, and how such wind affect the development of wind waves and wave spatial distributions.

In order to capture such complex wind and wind wave fields in coastal zones, high-resolution data of both wind and wave are required. Satellite scatterometers (Section 2.1.2) provide us with surface vector winds over a wide coverage with spatial resolution of 25 km. They have visualized the orographically modified winds like gap winds. They allowed us to examine the extensity of the winds, the formation mechanisms, and oceanic responses [e.g., Kawamura and Wu, 1998; Luis and Kawamura, 2000; Chelton et al., 2000a and 2000b; Hu and Liu, 2003]. On the other hand, SAR can resolve high-resolution wind fields by applying SAR wind retrieval algorithms (Section 1.3.2) to SAR images (Section 2.1.1). They reveal complex wind distributions in coastal zones and provide us a unique picture of coastal winds [e.g., Sandvik and Furevik, 2002; Pan and Smith, 1999]. SAR-derived wind fields are especially valuable in near-coastal areas where observational data often are too sparse to give a representative picture of the local winds. SAR allows us to examine the details of coastal winds, from shore to the offshore where scatterometer data are available.

Satellite radar altimeters can provide us with spatial profiles of significant wave heights (hearafter SWHs) along their ground tracks with spatial resoluition of about 7 km. The altimeter-derived wave heights have been utilized in various sturdies of wind waves including wave climate [e.g., Bauer and Staabs, 1998], validation of wave models [e.g. Romeiser, 1993; Hwang et al., 1998], and assimilation into the models [Bauer et al., 1992]. Additionally, snapshot altimeter wave height observations are effectively used for investigating fetch growth of wind wave in combination with scatterometer wind measurements in Ebuchi et al. [1992] and Ebuchi [1999].

In this study, we present two case studies of air-sea-land interaction under winter monsoon in order to demonstrate a great impact of coastal winds on wave distributions. The synergetic use of high-resolution satellite observations allows us to examin winds and waves in coastal zones and to reveal actual wind and wave distribution. This study will also give a new perspective of studying air-sea-land interaction in coastal zones using high-resolution satellite observations.

In Section 5.2, we present complete and close-up wind fields by a combined use of scatterometer and SAR. Then, we compare the wind fields with wave height observations from altimeters. Section 5.3 is devoted for discusiion, and conclusions are given in Section 5.4.

5.2 Combined satellite observations of the coastal winds and waves – Two case studies

5.2.1 Case selection and analysis methods

In this section, we illustrate the relation between wind and wave distribution from two representative time periods of satellite observations. We focus on the Pacific side of Tohoku and Hokkaido distincts under the outbreaks of the East Asian winter monsoon. During the winter monsoon, strong winds blow constantly over the Sea of Japan from Siveria towards the west coast of Japan. Then, they pass through the Japanese archipelago and blast out toward the northwestern Pacific. Figure 5.1 shows a map of topography in the region. There exist some orographic gaps, such as Tsugaru Straits, the Bays of Uchiura and Mutsu. The outbreaks usually persist for periods longer than one day. Under such conditions, it is verified that situations may be simplifid as a fetch-limited, one-dimensional, time-independent [Ebuchi et al., 1992; Ebuchi, 1999]. Therefore, wind distributions are directly reflected in wave distributions because the swell energy is a much smaller contribution to the total wave height.

Table 5.1 summarizes observational conditions of two case studies on 25 February 2000 (Case 1) and 4 December 2000 (Case 2). In the following case studies, we start with a discussion of the synoptic situation. Figure 5.2 is the hourly wind speed and direction recorded from a buoy in Mutsu Bay (Figure 2.2). The time-series wind observations can be representative examples of synoptic wind variations. As will hereinafter be described in detail, we can identify steady-state wind periods on 25th February and 4th December 2000. The arrows in the figures indicate passing times of QuikSCAT, ERS-2 SAR, T/P and ERS-2 altimeters. Observation time differences between satellite sensors are unimportant to grasp representative views under the steady winter monsoon outbreaks.

Then, ocean and land surface winds measured by QuikSCAT, ERS-2 SAR, and AMeDAS are jointly imvestigated. They are shown in Figure 5.3 and 5.5. Figure 5.4 and 5.6 are enlarged views of Figure 5.3 and 5.5 with a centeral focus on SAR observation areas. SAR images are converted into wind speed maps by applying SAR wind retrieval methods (Section 1.3.2). Wind direction data are obtained from NCEP/NCAR reanalysis data. Under high wind situations, wind directions can reasonably be extracted from images themselves. The wind directions of NCEP/NCAR reanalysis data are consistent with the wind-direction information obtained from the SAR images.

Finally, using SWH data from T/P and ERS altimeters, we investigate the relation between wind and wave distributions. SWHs along altimeter tracks are plotted in Figure 5.3-5.5. Wind-speed and SWH variations are also compared along the altimeter ground tracks and arbitrarily defined lines. For comparison with the high-resolution surface winds from SAR and altimeter, the low-resolution surface vector winds of QuikSCAT are linearly interporated onto the defined lines.

5.2.2 Case 1: February 25, 2000

According to the synoptic weather charts at 00:00 UT, February 25, 2000 (not shown), a low-pressure system had passed through the southern part of Japan, and areas around Japan were under wintery pressure pattern favorable to the monsoon outbreak. In Figure 5.2 (a), wind speed rapidly increases at 18:00 UT February 24, 2000, and higher and steady wind around 10 m/s lasted the entire one day. During the period, the wind direction is almost constant at 280° (Figure 5.2 (b)). The observation time of ERS-2 SAR corresponds to the onset of winter monsoon outbreak and observations of the other sensors follow within twelve hours (Table 5.1).

At 09:06 UT, QuikSCAT observed wind around Japan (Figure 5.3(a)). In the northweastern Pacific, two distinguished wind jets with speeds above 12 m/s are seen to extend from the proximity of Tsugaru Straits and the south of Kitakami highland (See also Figure 5.1). The strongest winds with speeds more than 16 m/s are observed in the jets. Local maximum wind speeds are located at (40°N, 143°E), (39°N,147°E), and (37°N, 145°E). Between the two jets, we can see a lower wind region extending toward the offshore about 500 km from the coast, and reach at least 146°E.

Wind speeds are retrieved from SAR images acquired at 01:15 UT (Figure 5.3(a) and 5.4(a)). In the northeastern part of SAR images, a part of northern wind jet with speeds of

12 m/s is captured. The wind speeds are lower than 8 m/s in the coastal area within 50 km from the coastline. In the region, we can see alternative high/low wind regions, which can be considered as extensions of the terrestrial wind patterns affected by the upstream land topography. We identify two distinguished lower wind regions less than 6 m/s. They consistently connect to offshore low-wind regions observed by QuikSCAT. According to AMeDAS observations, wind speeds are much lower (2-5m/s) than those observed over the surrounding seas by QuikSCAT, which is a quite contrast (Figure 5.4(a)). It is true to both upstream and downstream sides of Japan (Figure 5.3(a)). From the SAR-derived wind fields, it is shown that wind speed transition occurs at around 50 – 100 km distances from the coastline, which is consistent with the statistical features of coastal winds shown in Chapter 4.

SWH data are obtained from T/P track 60 and ERS track 905 at 10:04 UT and 12:23 UT, respectively. They are plotted in Figure 5.3(a) and 5.4(a). The T/P track intersects between the coasts of Hokkaido and the Tohoku distinct. The SWHs are higher at the center of the track (Figure 5.3(b)). This is due to longer fetches from the head of Uchiura Bay and larger wind speeds in the jet (Figure 5.3(b)). The ERS ascending track pass near the eastern coast of North Japan pass through the SAR observation area. When passing through the southern jet, local maximum wave height above 3.0 m is observed at around 37.5°N (Figure 5.3(c)). In south of 37.5°N, SWHs are higher than 2.5 m, which may be mainly due to the larger fetch. The SWHs and the QuikSCAT wind speed along the ERS track have local minimums at around 39.5°N, where the low-wind region extends from the coast. At the latitude, SWHs are 1.0 m lower than those in neighboring jets. In the northern wind jets, ERS altimeter observes SWH higher than 2.0 m. These local maximums and minimums of SWH well correspond to those of QuikSCAT wind speeds along the ERS ground track (Figure 5.3(c)).

Figure 5.4(b) shows wind speed profiles along a defined black line indicated in Figure 5.4(a). It is perpendicular to the streamlines derived from surface wind vectors. In the SAR area, the QuikSCAT wind speeds are generally higher than SAR-derived wind speeds. Smaller-scale variations corresponding the alternative high/low wind regions are observed only in the SAR profile.

Figure 5.4(c) shows wind speed profiles of QuikSCAT, SAR and ERS altimeter along the ERS ground track. Smaller-scale wind speed variations are seen in the SAR and altimeter wind-speed profiles, and they agree well each other. The QuikSCAT wind-speed profile overestimates wind speed in the region of wind minimum at around 39 – 39.5°N. The SWH profile observed by ERS altimeter is also shown in the figure. The local SWH maximums and minimums well correspond to those of the SAR and altimeter wind speeds.

5.2.3 Case 2: December 4, 2000

According to the synoptic weather charts at the 00:00 UT, December 3, 2000 (not shown), the area around Japan was under wintery pressure pattern as well as Case 1. Figure 5.2 (c) shows that the buoy-observed wind speed higher than 10 m/s lasted almost two days from 00:00 UT, December 3. Wind direction (Figure 5.2 (d)) is almost constant of 280° during the period. From 18:00 UT on 4th, a low-pressure system had started to pass through Japan, and southerly and lower wind were observed until 03:00 UT on 5th. The observations of ERS-2 SAR and altimeter are on the same orbit, and the observation time corresponds to the midpoint of winter monsoon outbreak. QuikSCAT and T/P observations are obtained in a latter half of the outbreak period.

At 08:42 UT, QuikSCAT observed a strong wind jet off the southern Hokkaido (Figure 5.5(a) and 5.6(a)). The wind jet extends more than 600 km from the vicinity of Tsugaru Straits. In the jet, with speeds are as great as 16 m/s and the local maximum wind speed is observed in the south of Cape Erimo. In the both sides of the jets, lower wind regions extend along the jet from southeastern side of Hokkaido and Kitakami Highland, respectively. Their minimum wind speed is less than 8 m/s.

The wind-speed map is retrieved from SAR images acquired at 1:20 UT on Dec. 4, 2000 (Figure 5.5(a) and 5.6(a)). It is obviously shown that there exist three distinguished wind jets in the SAR observation areas. These wind jets over ocean correspond to topographical features of the upstream area. The northern and middle jets have local maximum wind speeds at the mouth of the Bay of Uchiura, and the exit of the Tsugaru Straits, respectively. The southern jet is seen from the centeral area of Mutsu Bay to the Pacific across the Shimokita Peninsula. In its lee side near the coast, wind speeds are lower, but increase rapidly to form the southern jet. While these jets have wind speed as great as 14 m/s, the lower wind-speed regions between jets have them less than 8 m/s. The jets broaden toward the offshore region and merge into one large jet flow as seen in QuikSCAT surface vector wind field (Figure 5.5(a)). According to AMeDAS observations, wind speeds are much lower (2-5m/s) than observed over the surrounding seas as seen in Case 1.

The SWHs are obtained from T/P track 253 and ERS track 978 at 15:44 UT and 01:23, respectively. They are superimposed in Figure 5. 5(a). The T/P and ERS tracks pass the Pacific Ocean off eastern coast of Japan. Local SWH maximums about 4 m at around 41°N along both altimeter tracks are observed in the jet region (Figure 5. 5 (b) and (c)). The altimeter track segments with SWHs larger than 3.0 m correspond to the regions where QuikSCAT-derived wind speeds are greater than 12.0 m/s (Figure 5. 4 (b) and (c)). In the jet area, the longer fetches from the Uchiura Bay and Tsugaru Straits contribute to the generation of the higher SWHs. High SWHs are also observed at around 45°N along the ERS track and at around 44°N along the T/P track, respectively. These are also corresponding a strong wind region blowing through the Souya Straits between Hokkaido and Sakhalin.

Figure 5.6(b) shows wind speed profiles along the defined black line indicated in Figure 5.6 (a). It crosses the three wind jets. The SAR-derived wind speeds represent three local maximums of wind speed associated with three wind jets.

5.3 Discussion

Figure 5.7 (a) shows a comparison between QuikSCAT- and SAR-derived wind speeds in the overlapping area from both case studies. Bars indicate a tenfold relative root mean square of SAR-derived wind speeds contained in a QuikSCAT observation cell. Totally, the root mean square error is 1.86 m/s and the bias is –1.23 m/s. While they generally agree well in higher wind speed than 12 m/s, QuikSCAT overestimates wind speeds in lower wind speed range than 12 m/s. Overestimated wind speeds are all observed in the wind wake of Case 1. They also have larger error bars.

On the other hand, Figure 5.7 (b) shows a comparison between ERS altimer- and SAR-derived wind speeds along the ERS ground track on February 25, 2000. The root mean square error is 1.05 m/s and the bias is 0.05 m/s. They agree well each other. This means that high-resolution wind observations are essential in coastal zones.

The QuickSCAT overestimate in Figure 5.7 (a) may be attributed to its wind retrieval algorithm. First, NRCS observed in the same wind vector cell (WVC) are assembled. The SeaWinds swath is divided into equidistant across-track WVCs. The nominal WVC size is $25\text{km} \times 25\text{km}$, and all backscatter measurements centered in a WVC are used to derive the WVC wind solutions through a maximum likelihood estimate (MLE) method. Then, a GMF is applied to the set of backscatter measurements in each WVC. Using the NRCS values, NRCS measurement variance, the azimuth angle, the incidence angle, the polarization and the model function, the processor generates a MLE value for each element in a set of wind vector solutions. The measurement variance of backscatter is used in wind retrieval to weight the backscatter measurements in the MLE method.

The MLE indicates how well the backscatter measurements used in the retrieval of a particular wind vector fit the GMF, which is derived for fair weather wind conditions. In addition, GMFs are tuned against open ocean wind conditions. A large inconsistency with the GMF results in a large MLE, which indicates geophysical conditions other than those modeled by the GMF, such as rain, confused sea state, or ice.

In the present case, NRCS measurement variance in a WVC due to coastal wind variability results in a large MLE. This produce wind speed overestimates of QuikSCAT. As shown in Chapter 4, it is essential that coastal winds have large valiability. This is quite a contrast to offshore wind variabilities.

5.4 Conclusions

Using high-resolution satellite observations, we presented case studies to focus on studying wind wave distribution under East Asian winter monsoon in the northeast of Japan. A combined use of QuikSCAT and ERS-2 SAR-derived winds allow us to examine the orographically modified winds detail from shore to offshore. Then, we investigated wave height variations under the wind fields using SWHs observed by T/P and ERS-2 altimeters. The following conclusions are given.

1) QuikSCAT observes wind jets and the nighboring lower wind regions extending more than several hundred kilometers downwind.
2) SAR-derived wind fields reveal smaller-scale coasal wind jets and lower wind regions. They can be considered as extensions from terrestrial wind jets such as Uchiura Bay and Tsugaru Straits.
3) Smaller-scale wind variations revealed by SAR extend and broaden downwind, and consisitently connect to the larger-scale wind jets and lower wind regions observed by QuikSCAT.
4) QuikSCAT- and SAR-derived wind speeds generally agree well each other. But in the coastal seas with high wind variability, QuikSCAT overestimates wind speeds.
5) SWHs along altimeter ground tracks intersecting strong and weak wind regions vary with wind speeds revealed by QuikSCAT and SAR. The locations of SWH local maximums and minimums agree well with those of wind speeds derived from QuikSCAT and SAR. This means that terrestrial gaps produce the orographically

modified winds, which broaden and extend several hundred kilometers downwind, and, in turn, such wind fields determine wind sea.

This study demonstrates the capabilities of scatterometer and SAR-derived winds for monitoring coastal winds, and the potential of multi-sensor approaches for studying air-sea-land interaction in coasal zones. High-resolution wind fields are essential to study the oceanic responses in open seas as well as in coastal zones. We point out that high-resolution wind fields revealed by SARs will direct the numerical model approach of coastal winds. They will be also responsible for further understanding of wind-wave coupling. Moreover, this study promotes an improvement to examine the capability of high-resolution wave forecast models for capturing the essential characteristics of wind impact on wind wave.

Table 5.1 Observational conditions of two case studies. Wind speed and direction are obtained from a buoy observation in Mutsu Bay.

				Time UTC			
Case	Date	Wind Direction	Wind Speed	ERS-2 SAR	QuikSCAT	T/P	ERS RA
1	25,Feb. 00	North-West	11 m/s	0115	0906	0121	1252
2	4,Dec. 00	North-West	12 m/s	0120	0842	1544	0123

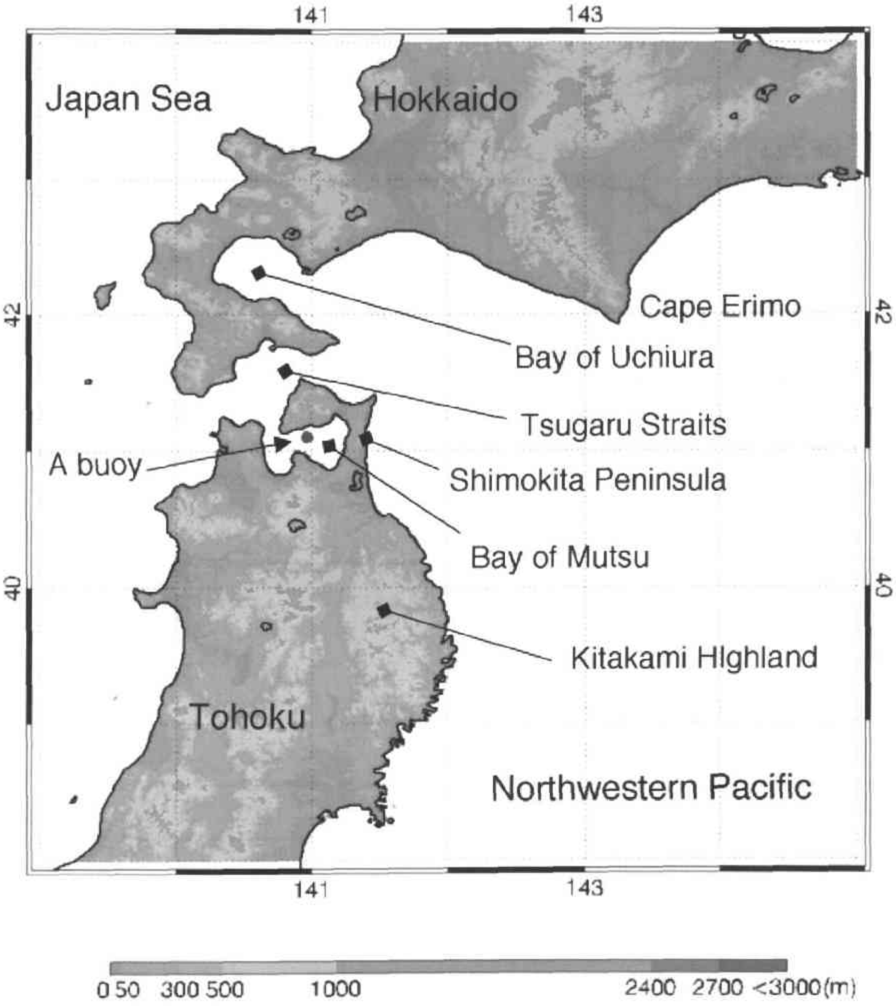

Figure 5.1 Map of the topography and geographical locations referred to in this paper. The color scale indicates the elevation. A blue plot indicates the location of a buoy in Mutsu Bay.

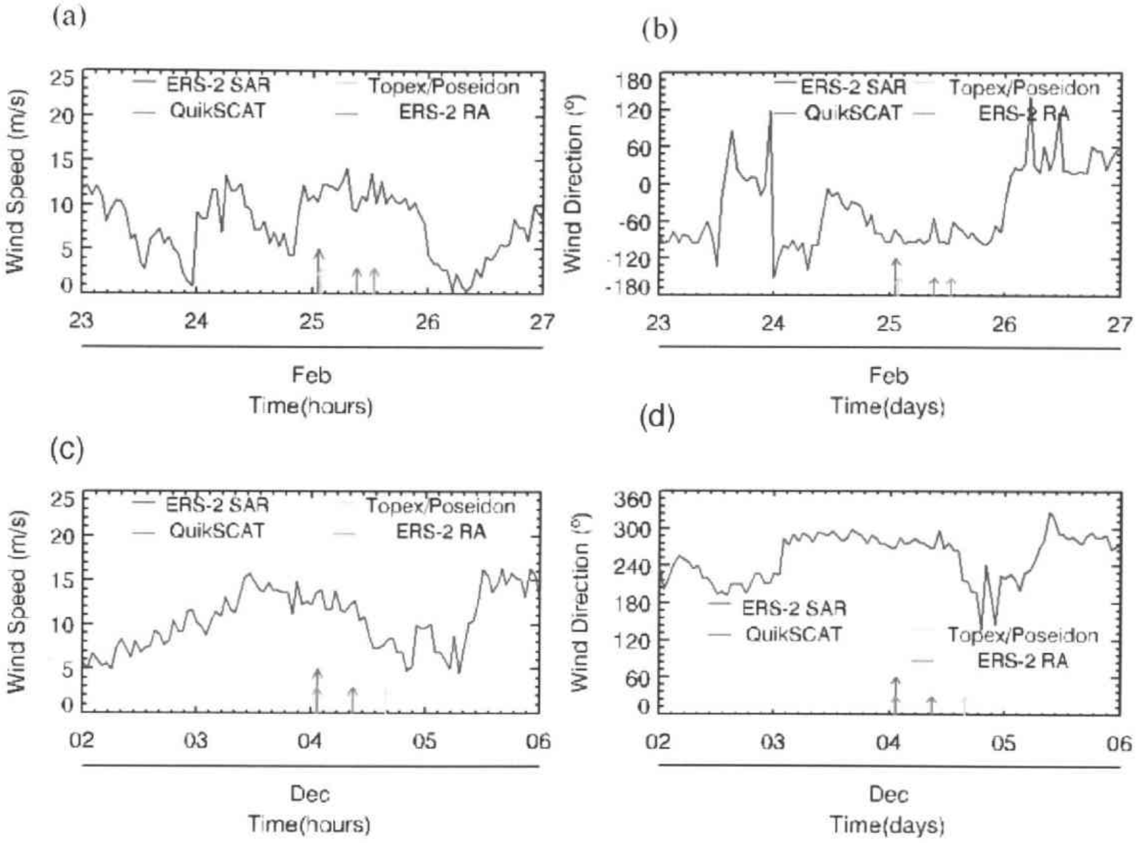

Figure 5.2 Hourly wind observations recorded at an buoy in the Mutsu Bay. Top and bottom figures are obtained from February 23 to 26 and December 2 to 5, 2000. Left and right figures show wind speed and wind direction. The arrows indicate the time when ERS-2 SAR, QuikSCAT, Topex/Poseidon, ERS-2 altimeter pass through the study area.

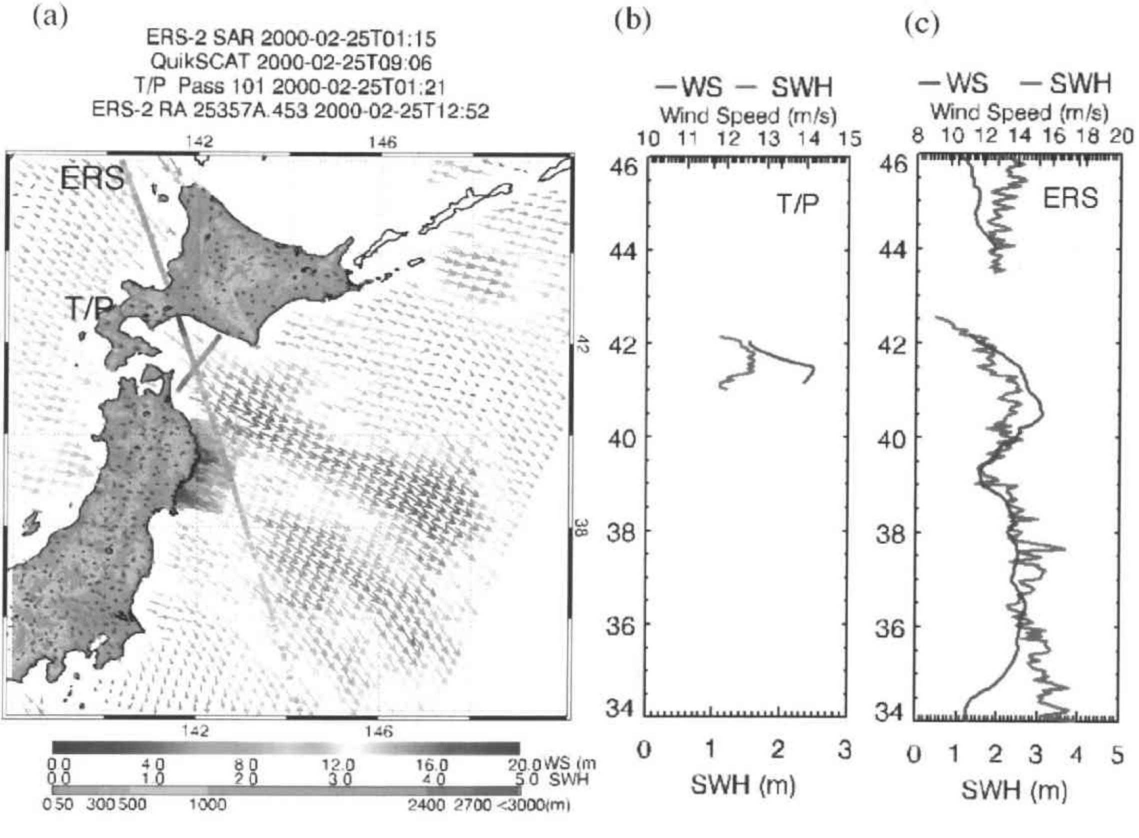

Figure 5.3 (a) Ocean and land surface winds measured by QuikSCAT, SAR, and AMeDAS. Winds are measured by QuikSCAT, ERS-2 SAR, and AMeDAS at 09:06 UT, 01:15 UT, 01:00 UT, February 25, 2000, respectively. SWHs measured by T/P and ERS altimeters are also plotted. They are obtained at 01:21 UT and 12:52 UT, February 25, 2000, respectively. The color scales indicate the magnitude of wind speed, SWH, and the elevation. (b) (c) SWH along the tracks of (b) T/P and (c) ERS altimeters and QuikSCAT wind speed.

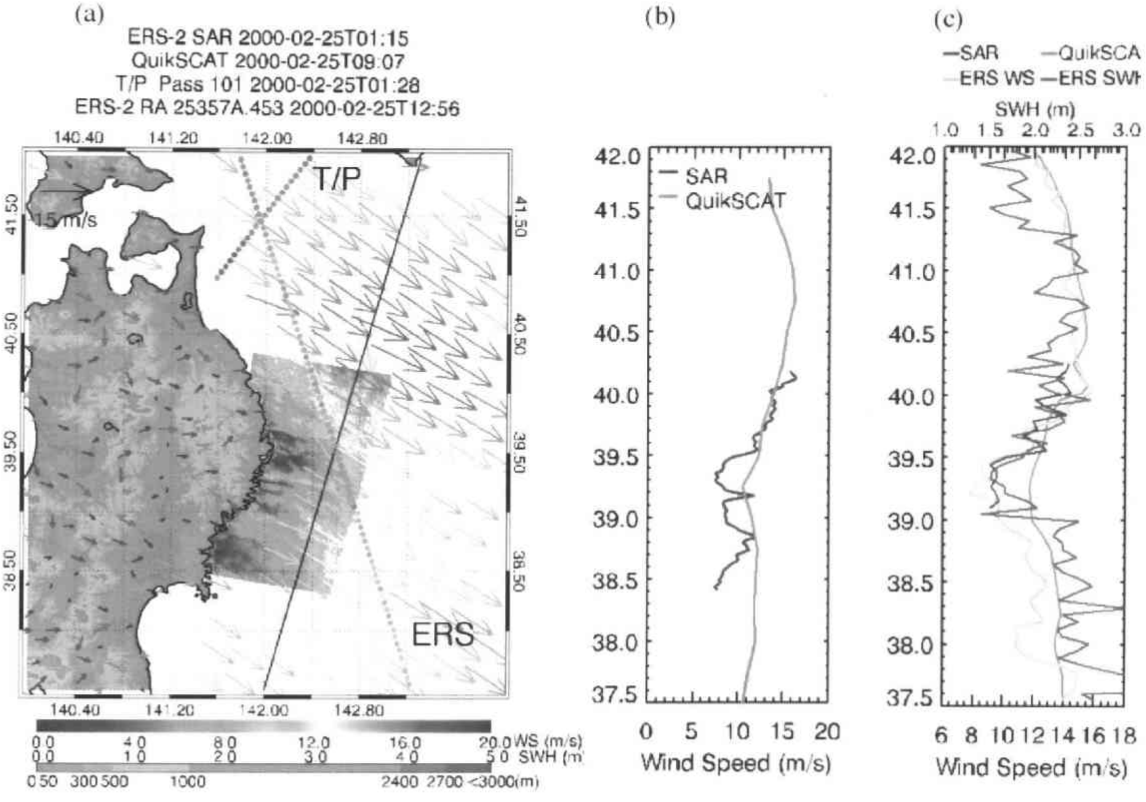

Figure 5.4 (a) Close-up view of Fig.5.3 (a) with a focus on SAR observations. The black line are profiles of wind speed. (b) Wind speeds derived from SAR, QuikSCAT and model along the black line in (a). (c) Wind speeds derived from SAR, QuikSCAT and ERS altimeter along the ERS ground track. ERS altimeter SWHs are also plotted.

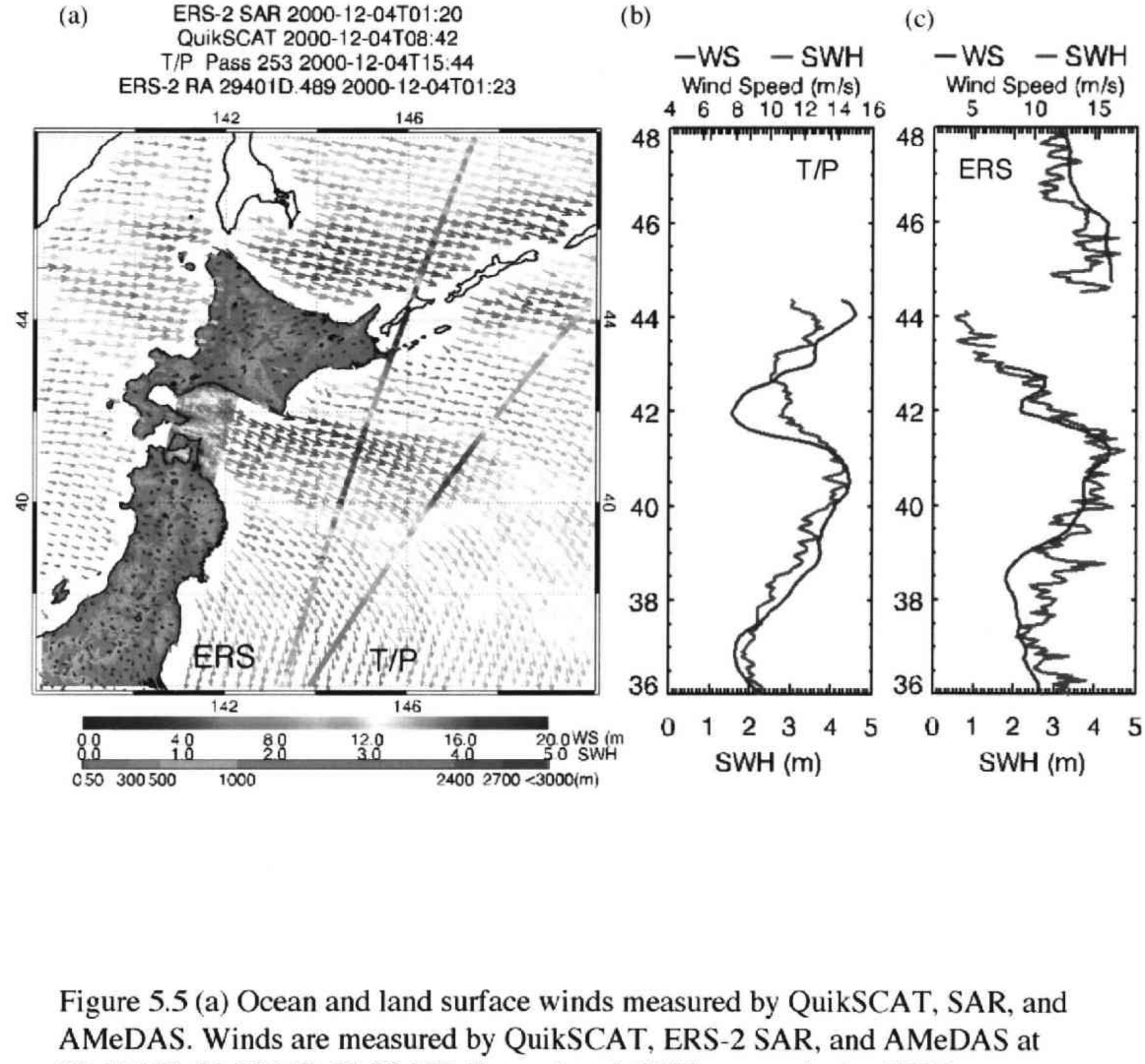

Figure 5.5 (a) Ocean and land surface winds measured by QuikSCAT, SAR, and AMeDAS. Winds are measured by QuikSCAT, ERS-2 SAR, and AMeDAS at 08:42 UT, 01:20 UT, 01:00 UT, December 4, 2000, respectively. SWHs measured by T/P and ERS altimeters are also plotted. They are obtained at 15:44 UT and 01:23 UT, December 4, 2000, respectively. The color scales indicate the magnitude of wind speed, SWH, and the elevation. (b) (c) SWHs along the tracks of (b) T/P and (c) ERS altimeters and QuikSCAT wind speed.

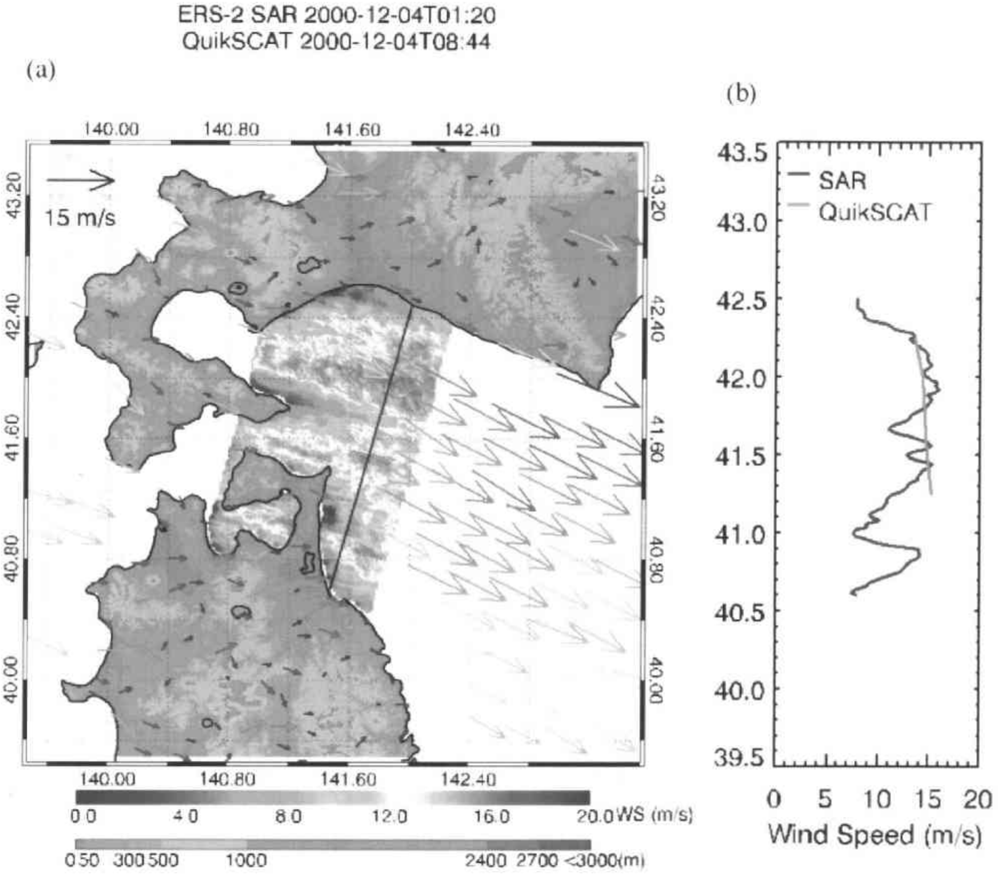

Figure 5.6 (a) Close-up view of Fig.5.4 (a) with a focus on SAR observations. The black line are profiles of wind speed. (b) Wind speeds derived from SAR, QuikSCAT and model along the black line in (a).

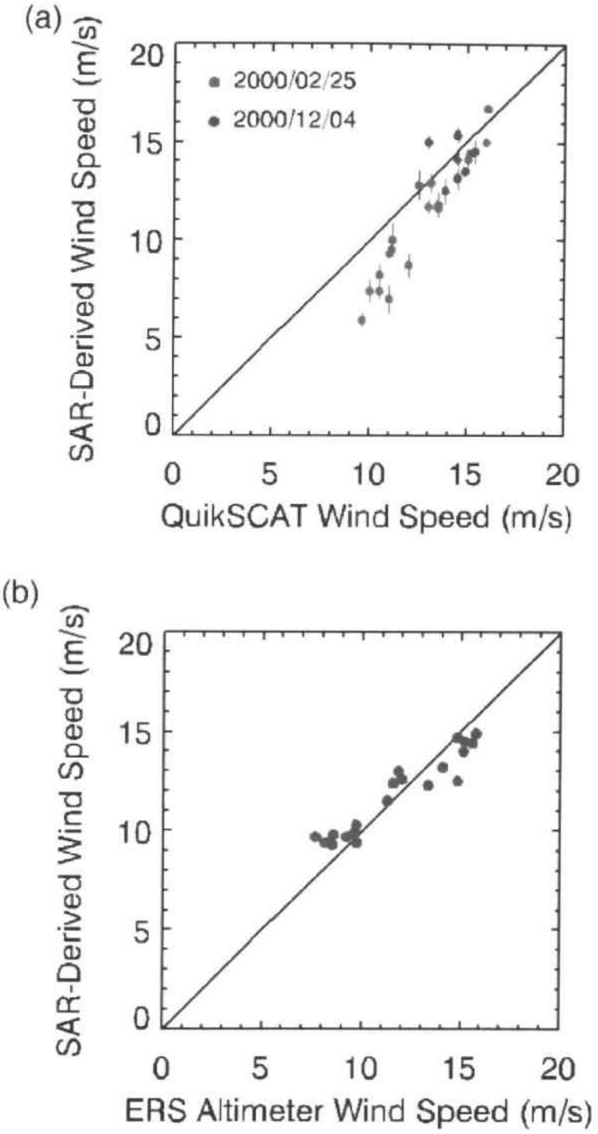

Figure 5.7 (a) Comparison of SAR-derived wind speeds with QuikSCAT wind speeds. Red and blue plots are from observations on 25 February and on 4 December, 2000, respectively. Bars indicate a tenfold relative root mean square of SAR-derived wind speeds contained in a QuikSCAT observation cell. (b) Comparison of SAR-derived wind speeds with wind speeds derived from ERS-2 altimeter on 25 February, 2000.

6 Conclusions

In the present study, we have investigated coastal surface winds resoleved by the high-resolution SAR images. The wind-retrieval methodology of L-band SAR is established and applied to coastal researches. A large amount of SAR images enable us to reveal new statistical features of the coastal wind. Their synagetic use of other active satellite sensors and in situ observations provide new views of the surface wind fields from shore to offshore.

Main conclusions derived in Chapters 3, 4 and 5 are summarized as follows.

In Chapter 3, we have developed a new L-band geophysical model function using the JERS-1 SAR images. Then, retrieved wind speeds from JERS-1 SAR in the coastal region are examined and excessive ambiguities of JERS-1 SAR are quantitatively estimated.

1) We expressed the system noise peculiar to JERS-1 SAR as a parabolic function of range the SAR system noise. By subtracting the estimated system noise from the SAR images, we extracted the relative calibrated ocean signals from JERS-1 SAR images.

2) We investigated sigma-0 dependence on the radar incidence angle, the wind speed, and the wind direction. Results of the present study indicated that dependence of sigma-0 on the incidence angle is negligible for its range of $37.0° - 42.0°$. Dependence of sigma-0 on the wind speed can be well expressed by the conventional power law formula. For higher wind speeds, the upwind-downwind asymmetry becomes very larger. But, for wind speeds below 8 m/s, these features are not significant.

4) Using third-cosine harmonics, we represented the relationships a new L-band-HH GMF for SAR wind retrieval. It enables us to convert a JERS-1 SAR image into a wind-speed map. The SAR-derived wind speed has a RMSE of 2.09 m/s with a negligible bias against the wind speeds used for deriving the model function.

5) We investigated wind speed growth with offshore distance in Sagami Bay using ERS-1 SAR derived wind fields, and formulated the relationship.

6) Not only the first azimuth ambiguity but also higher order azimuth ambiguities and range ambiguity have a significant influence on near-shore wind retrieval.

In Chapter 4, we investigated the statistics of high-resolution coastal winds derived from SAR.

1) We investigated wind-speed histgrams by applying the Weibull distribution and classifying them using the two parameters of Weibull distribution. Wind data are obtained on and around Japan and off a part of the Eurasian continent. In the Weibull parameter feature space, the wind-speed histgrams are classified into three clusters: Land cluster, Open Ocean cluster and Coastal Sea cluster.

2) The typical wind-speed histgram derived from each cluster center have the following features: the Land histogram has high frequencies in a range of lower wind speeds and quite low frequencies in the range higher than about 6 m/s. The Open Ocean histogram has high frequencies in the wind-speed range around 8 m/s and extends up to 20 m/s. The Coastal Sea histogram has the peak frequency at around 3 m/s though the peak value is higher than that of the Land histogram. It has frequencies in a wide wind-speed range up to 20 m/s as the Open Ocean histogram has.

3) Using the Open Ocean and Land histgrams, the Coastal Sea histogram is reproduced by ramdom sampling of the open ocean and land wind-speeds. The reproduced histgrams indicate the same features as those obtained from the SAR-derived wind speed. The histograms at around the Coastal Sea cluster center are reproduced at the mixing ratio of about 30 % of the Land histgram and about 70% of the Open Ocean histgram.

4) Standard deviation and skewness estimated from the SAR-derived high-resolution wind-speed maps have wider distribution ranges in the near-coast seas and the ranges decrease with distance from the coast to 100 km offshore, which suggest that the offshore distance of 100 km can be a separation scale of the coastal sea and open sea.

In Chapter 5, using high-resolution satellite observations, we presented case studies to focus on studying wind wave distribution under the orographically modified winds of East Asian winter monsoon off Tohoku and Hokkaido, Japan.

1) The QuikSCAT observervations present wind jets and the nighboring lower wind regions extending more than several hundred kilometers downwind from the coasts.

2) The SAR-derived wind fields reveal smaller-scale coasal wind jets and lower wind regions. The coastal jets can be considered as extensions from terrestrial gap winds formed in Uchiura and Mutsu Bay and the Tsugaru Straits.

3) Smaller-scale wind variations revealed by the SAR images extend and broaden with the distance from the coasts, and consisitently connect to the larger-scale wind jets and

lower wind regions observed by QuikSCAT.

4) The QuikSCAT- and SAR-derived wind speeds generally agree well each other. But in the seas near the coast with large wind variability, the QuikSCAT tends to overestimate wind speeds.

5) Singificant wave heights (SWHs) along altimeter ground tracks intersecting strong and weak wind regions vary with wind speeds revealed by QuikSCAT and SAR. The locations of SWH local maximums and minimums well agree with those of QuikSCAT wind speed. This means that terrestrial gaps produce the orographically modified winds, which broaden and extend several hundred kilometers downwind, and in turn, the wind fields determine the conditions of wind sea.

This study has given new views of the coastal surface wind by the high-resolution SAR images. The high-resolution capability of surface wind measurements is essential to study and monitor the coastal winds because of their natural features. Based on the accomplishments of the present study, it is desired that the understanding of coastal wind will be grown by more studies and that the results will be reflected in understanding of meteorological and oceanic phenomena in coastal zones and improvements of numerical model approaches.

Appendix 1 Acronyms

ADEOS	Advanced Earth Observing Satellite
ALOS	Advanced Land Observing Satellite
AMeDAS	Automated Meteorological Data Acquisition System
AMI	Active Microwave intrument
CMOD-4	C-band scatterometer model functions
CMOD-5	C-band scatterometer model functions
CSA	Canada Space Agency
DLR	German Aerospace Research Establishment
ERS OPR	ERS Ocean PRoduct
ERS-1	European Remote Sensing Satellite 1
ERS-2	European Remote Sensing Satellite 2
ESA	European Space Agency
GMF	Geophysical Model Function
GMT	Greenwich Mean Time
HH	horizontal polarized transmission, horizontally polarized reception
JERS-1	Japanese Earth Remote-Sensing Satellite
JMA	Japan Meteorological Agency
JPL	Jet Propulsion Laboratory
JWA	Japan Weather Association
MITI	Ministry of International Trade and Industry
NASA	National Aeronautics and Space Administration
NASDA	National Space Development Agency (Japan)
NCEP/NCAR	National Centers for Environmental Predition/ National Center for Atmospheric Research
NRCS	Normalised Radar Cross Section
NRIESDP	National Research Institute for Earth Science and Disaster Prevention
NSCAT	NASA scatterometer
PALSAR	Phased Array type L-band Synthetic Aperture Radar
PO.DAAC	Physical Oceanography Deistributed Active Archive Center
RADARSAT	Radar Satellite
S/N	Signal to Noise Ratio
SAR	synthetic aperture radar
SASS2	Seasat-A Scatterometer System model function
SEASAT	Sea Satellite
SIR-A	Shuttle Imaging Radar-A
SIR-B	Shuttle Imaging Radar-B
SIR-C	Spaceborne Imaging Radar-C
SIR-C/X-SAR	Spaceborne Imaging Radar-C/X-Band Synthetic Aperture Radar
SMOS	Soil Moisture and Ocean Salinity Mission
T/P	Topex/Poseidon
VV	vertical polarized transmission, vertically polarized reception

Appendix 2 An L-band geophysical model function and its coefficients

The form of the L-band geophysical model function is:

$$\sigma_{lin}^{0} = a_0 + a_1\cos\phi + a_2\cos 2\phi + a_3\cos 3\phi$$,

where ϕ is the relative wind direction. Coefficients a_0, a_1, a_2 and a_3 are function of wind speed. They are expressed as follows:

$$a_0 = 10^{b_1}U^{b_2}(U < 8.5)$$

$$a_0 = 10^{b_3}(U - U_0)^{b_4} + b_5(U \geq 8.5)$$

$$a_1 = b_6(\exp(b_7 U) - 1)$$

$$a_2 = b_8 U^2 + b_9 U$$

$$a_3 = b_{10}(\exp(b_{11}U) - 1)$$

The threshold value is set as $U_0 = 8.5$. The coefficients $b_i(i = 1,2,3..11)$ are summarized below.

$b_1 = 5.2194296$

$b_2 = 0.7343264$

$b_3 = 5.0711371$

$b_4 = 1.2282002$

$b_5 = 797859.7$

$b_6 = 41869.28$

$b_7 = 0.1988929$

$b_8 = 6862.769$

$b_9 = \text{-}49958.58$

$b_{10} = 8107.274$

$b_{11} = 0.1677051$

Acknowledgements

I express my deepest gratitude to Prof. Hiroshi Kawamura. He has continuously encouraged me and given me full support throughout the course of the studies. I am deeply grateful to Dr. Toshio Suga, Dr. Shoichi Kizu, and Dr. Futoki Sakaida, and especially to Prof. Kimio Hanawa for their helpful discussions and suggestions. I also appreciate useful comments from Prof. Naoto Ebuchi of Hokkaido University.

I would like to sincerely thank Dr. Masanobu Shimada of Earth Observation Research and application Center (EORC), Japan Aerospace Exploration Agency. He guided me toward a use of SAR data and provided us with Sigma SAR Processor.

Thanks are due to all the members of Ocean Environmental Group of Center for Atmospheric and Oceanic Studies and Physical Oceanography Group of Tohoku University. Thanks are extended to elder members of two groupes for their help and beneficence from their accomplishments. Researchers from foreign countries always inspired me to further studies. Above all, I have received support from Dr. Osamu Isoguchi, Dr. Fumiaki Kobashi, Mr. Takuya Oonishi, and Mr. Satoshi Yamaguchi.

Both JERS-1 and ERS-1/2 SAR data were provided from National Space Development Agency of Japan. NSCAT, SeaWinds/QuikSCAT, and T/P data were obtained from NASA Physical Oceanography Distributed Active Archive Center at the Jet Propulsion Laboratory. ERS OPR data were obtained from CERSAT, at IFREMER, Plouzané (France). NCEP Reanalysis data are downloaded from the web site of the NOAA-CIRES Climate Diagnostics Center, Boulder, Colorado, USA. The buoy and AMeDAS data were provided by the Japan Meteorological Agency. Hiratsuka Experiment Station data were provided by National Research Institute for Earth Science and Disaster Prevention of Japan. Buoy observations in Mustu Bay were provided by Aomori Prefectural Aquaculture Research Center.

References

Alpers, W., and B. Brümmer, "Atmospheric boundary layer rolls observed by the synthetic aperture radar aboard the ERS-1 satellite", J. Geophys. Res., vol. 99, 12613-13621, 1994.

Alpers, W., U. Pahl, and G. Gross, "Katabatic wind fields in coastal areas studied by ERS-1 synthetic aperture radar imagery and numerical modeling", J. Geophys. Res., vol. 103, pp. 7875-7886, 1998.

Alpers, W. and I. Hennings, "A theory of the imaging mechanism of underwater bottom topography by real and synthetic aperture radar", J. Geophys. Res., 89(C6), 10,529-10,546, 1996.

Alpers, W., "Theory of radar imaging of internal waves", Nature, 314, 245-247, 1985.

Alpers, W. and G. Stilke,"Observation of a nonlinear wave disturbance in the marine atomosphere by the synthetic aperture radar aboard the ERS1 satellite", J. Geophys. Res., 103, 6513-6525, 1996.

Alpers, W., U Pahl, and G. Gross, "Katabatic wind fields in coastal areas studied by ERS-1 synthetic perture radar imagery and numerical modeling", J. Geophys. Res., 103, 7875-7886, 1998.

Barthelmie, R. J. and S. C. Pryor, "Can satellite sampling of offshore wind speeds realistically represent wind speed distributions?", J. Appl. Meteorol., 42, 83-94, 2003.

Barton, E. D., G. Basterretxea, P. Flament, E. G. Mitchelson-Jacob, B. Jones, J. Arìstegui, and F. Herrera, "Lee region of Gran Canaria", J. Geophys. Res., 105(C7), 17,173-17,193, 2000.

Bauer, E., S. Hasselmann, and K. Hasselmann, "Validation and assimilation of Seasat altimeter wave heights using WAM wave model", J. Geophys. Res., 97, 12,671-12,682, 1992.

Bauer, E. and C.Staabs, "Statistical properties of global significant wave heights and their use for validation", J. Geophys. Res., 103, 1153-1166, 1998.

Bayley, G.V., and J. M. Hammersley, "The 'effective' number of independent observations in an autocorrelated time series", J. Roy. Stat. Soc., B8, 184-197, 1946.

Carswell, J. R., W. J. Donnelly, R. McIntosh, M. A. Donelan, and D. C. Vandemark, "Analysis of C and Ku-band ocean backscatter measurements under low-wind conditions", J. Geophys. Res., 104, 20,687-20,701, 1999.

Chelton, D. B., M. H. Freilich, and S. K. Esbensen, "Satellite observation of the wind jets off the Pacific coast of central America. Part I: Case studies and statistical characteristics", Mon. Wea. Rev., 128, 1993-2018, 2000a.

Chelton, D. B., M. H. Freilich, and S. K. Esbensen, "Satellite observation of the wind jets off the Pacific coast of central America. Part II: Regional relationships and dynamical consideration", Mon. Wea. Rev., 128, 2019-2043, 2000b.

Clemente- Colòn, P., and X.-H. Yan, "Lower-backscatter ocean features in synthetic aperture radar" , Johns Hopkins APL Technical Digest, 21(1), 116-121, 2000.

Clemente-Colòn, P. and X.-H. Yan, "Observations of East coast upwelling conditions in synthetic aperture radar imagery", IEEE Trans. Geosci. Remote Sensing, vol. 37(5), 2239-2248, 1999.

Conradsen, K, L. B. Nielsen, and L. P. Prahm, "Review of Weibull statistics for estimation of wind speed distributions", J. Climate Appl. Meteorol, 23, 1173-1183, 1984.

DiGiacomo, P. M. and B. Holt, "Satellite observations of small coastal ocean eddies in the Southern California Bight", J. Geophys. Res., 106, 22,521-22,543, 2001.

Dobson, F., W. Perrie, and B. Toulany, "On the deep-water fetch laws for wind-generated surface gravity waves", Atmos. Ocean, 27, 210-236, 1989.

Donelan, M.A., and W. J. Pierson, Jr., "Radar scattering and equilibrium ranges in wind-generated waves with application to scatterometry", J. Geophys. Res., vol. 92, pp. 4971-5029, 1987.

Ebuchi, N., "Statistical distribution of wind speed and direction contained the Preliminary NSCAT Science Data Products", J. Adv. Mar. Sci. Tech. Soci. vol. 3., No.2, pp.141-156, 1997.

Ebuchi, N., "Growth of wind waves with fetch in the Sea of Japan under winter monsoon investigated using data from satellite altimeter and scatterometer", J. Oceanogr., 55, 575-584, 1999.

Ebuchi, N., H. Kawamura, and Y. Toba, "Growth of wind waves with fetch observed by the Geosat Altimeter in the Japan Sea under winter monsoon", J. Geophys. Res., 97, C1, 809-819, 1992.

Etling, D. and Brown, R. A., "Roll vortices in the planetary boundary layer: A review", Boundary Layer Meteorol., 65, 215-248, 1993.

Fichaux. N. and T. Ranchin, "Combined extraction of high spatial resolution wind speed and wind direction from SAR images: A new approach using wavelet transform", Can.J.Remote Sensing, Vol. 28, No. 3, pp. 510-516, 2002

Furevik, B. and E. Korsbakken, "Comparison of derived wind speed from SAR and Scatterometer during the ERS Tandem phase", IEEE Trans. Geosci. Remote Sensing, vol. 38, no. 2, pp. 1113-1121, 2000.

Gerling, T. W., "Structure of the surface wind field from the Seasat SAR", J.Geophys.Res., vol. 91, pp. 2308-2320, 1986.

Guinard, N. W., J. T. Ransone, Jr., and J. C. Daley, "Variation of the NRCS of the sea with increasing roughness", J. Geophys. Res., vol. 76, pp. 1525-1538, 1971.

Hasselmann, K., and S. Hasselmann, "On the nonlinear mapping of an ocean wave spectrum into a synthetic aperture radar image spectrum and its inversion", J. Geophys. Res., 96, 10,713-10,729, 1991.

Henderson, F. M. and A. J. Lewis, "Manual of Remote Sensing, Volume 2, Principles and Applications of Imaging Radar", 896 pp., John Wiley & Sons, 1998.

Hessner, K., A. Rubino, P. Brandt, and W. Alpers, "The Rhine outflow plume studied by the analysis of synthetic aperture radar data and numerica simulations", J. Phys. Oceanogr., 31, 3030-3044, 2001.

Hsu, "Coastal Meteorology", Academic Press, New York, pp. 260, 1988.

Hu, H. and W. T. Liu, "Oceanic thermal and biological responses to Santa Ana winds", Geophys. Res. Lett., 30(11), 1596, doi:10.1029/2003GL017208, 2003.

Hwang, P. A., E. J. Walsh, W. B. Krabill, R. N. Swift, S. S. Manizade, J. F. Scott, and M. D. Earle, "Airborne remote sensing applications to coastal wave research", J. Geophys. Res., 103, 18,791-18,800, 1998.

Ichikawa, K., T.Kozu, T. Shimoyama, Y.Sakuno, T.Matsunaga, K. Takayasu, "Feasibility of spaceborne SAR monitoring of coastal lagoon environments", 23rd International Symposium on Space Technology and Science, Matsue, Japan May 26-June 2, 2000.

Johannessn, J. A., R. A. Shuchman, G. Digranes, R. Lyzenga, C. Wackerman, O. M. Johannnessn and P. W. Vachon, "Coastal ocean fronts and eddies imaged with ERS1 synthetic aperture radar", J. Geophys. Res., 101, 6651-6667, 1996.

Justus, C. G., W. R. Hargraves, and A. Yalcin, "Naionwide assesment of potential output from wind-powered generation", J. Appl. Meteorol., 15(7), 673-678, 1976.

Kawamura, H. and P.Wu, “Formation mechanism of Japan Sea Proper Water in the flux center off Vladivostok”, J. Geophys. Res., 103, 21,611-21,622, 1998.

Keller, W. C. and W. J. Plant, “Cross sections and modulation transfer functions at L and Ku bands mesured during the tower ocean wave and radar dependence experiment”, J. Geophys. Res., vol. 95, pp. 16, 277-16, 289, 1990.

Kerbaol, V., B. Chapron and P.W. Vachon, “Analysis of ERS-1/2 synthetic aperture radar wave mode imagettes”, J. Geophys. Res., vol. 103, No. C4, pp. 7833- 7846, 1998.

Korsbakken, E., J. A. Johannessen, and O.M.Johannessen, “Coastal wind field retrievals from ERS synthetic aperture radar images”, J. Geophys. Res., 103, 7857-7874, 1998.

Laing, A. K. and E. Brenstrum, “Scatterometer observations of low-level jets over New Zealand coastal waters”, Weather and Forecasting, 11, 458-475, 1996.

Lehner, S., J. Horstmann, W. Koch, and W. Rosenthal, “Mesoscale wind measurement using recalibrated ERS SAR images”, J. Geophys. Res., 103, 7847-7856, 1998.

Li, X., W. G. Pichel, M. He, S. Y. Wu, K. S. Friedman, P. C. -Colòn, and C. Zhao, “Observation of Hurricane-Generated Ocean Swell Refraction at the Gulf Stream North Wall With the RADARSAT-1 Synthetic Aperture Radar”, IEEE Trans. Geosci. Remote Sensing, vol. 40(10), 2131-2142, 2002.

Li, X., P. C.-Colòn, and W. G. Pichel, “Atmospheric vortex streets on a RADARSAT SAR image”, Geophys. Res. Lett., 27(11), 1655-1658, 2000.

Liu, W. T., K. B. Katsaros and J. A. Businger, “Bulk parameterization of air-sea exchanges in heat and water vapor including the molecular constraints at the interface”, J.Atmos. Sci., 36, 1722-1735, 1979.

Liu, W. T., “Progress in scatterometer application”, J. Oceanogr., 58, 121-136, 2002.

Long, D. G., R. S. Collyer, R. Reed, and D. V. Arnold, “Dependence of the normalized radar cross section of water waves on bragg wavelength-wind speed sensitivity”, IEEE Trans. Geosci. Remote Sensing, vol. 34, pp. 656-666, 1996.

Lu, J., ”Marine oil spill detection, statistics and mapping with ERS SAR imagery in south-east Asia”, Int. J. Remote Sens., 24(15), 3013-3032, 2003.

Luis, A. J., and H. Kawamura, “Wintertime wind forcing and sea surface cooling near the South Indiand tip Observed using NSCAT and AVHRR”, Rem. Sens. Envir., 73, 55-64, 2000.

Lumley, J. L. and Panofsky, H. A., “The Structure of Atmospheric Turbulence”, Interscience Publishers, John Wiley and Sons, 1964.

Lyden, J. D., R. R. Hammond, D. R. Lyzenga, and R. A. Shuchman, "Synthtic aperture radar imaging of surface ship wakes", J. Geophys. Res., 93, 12,293-12,303, 1988.

Melsheimer, C., W. Alpers, and M. Gade, "Investigation of multifrequency/multipolarization radar signatures of rain cells over the ocean using SIR-C/X-SAR data", J. Geophys. Res., 103, 18,867-18,884, 1998.

Monaldo, F. M, D. R. Thompson, R. C. Beal, W. G. Pichel, and P. Clemente-Colòn, "Comparison of SAR-derived wind speed with model predictions and ocean buoy measurements", IEEE Trans. Geosci. Remote Sensing, vol. 39, pp. 2587-2600, 2001.

Moore, R. K. and A. K. Fung, "Radar Determination of Winds at Sea", Pro. IEEE, 67, pp. 1504-1521, 1979.

Müller, G. and B. Brümmer, "Roll convecton within an Arctic cold-air outbreak: Interpretation of in situ aircraft measurements and spaceborne SAR imagery by a three-dimensional atmospheic model", Mon. Wea. Rev., 127, 363-380, 1999.

Overland, J. E., "Scale analysis of marine winds in straits and along mountainous coasts", Mon. Wea. Rev., 112, 2530-2534, 1984.

Pavia, E. G. and J. J. O'Brien, "Weibull statistics of wind speed over the ocean", J. Climate Appl. Meteorol, 25, 324-332, 1986.

Pierrehumbert and Wyman, "Upstream effects of mesoscale mountains", J. Atmos. Sci., 42, 977-1003, 1985.

Portabella, M., A. Stoffelen, and J. A. Johannessen, "Toward an optimal inversion method for synthetic aperture radar wind retrieval", J. Geophys. Res., 107, 10.1029/2001JC000925, 2002.

Quifen, Y., B. Chapron, T. Elfouhaily, K. Katsaros and J. Tournadre, "Observation of tropical cyclones by high-resolution scatterometry", J. Geophys. Res., 103, 7767-7786, 1998.

Romeiser, R., "Global varidation of the wave model WAM over a one-year period using Geosat wave height data", J. Geophys. Res., 96, 4713-4726, 1993.

Rotunno, R., "On the linear theory of land and sea breeze", J. Atmos. Sci., 40, 1999-2009, 1983.

Sandvik, A. D. and B. R. Furevik, "Case study of a coastal jet at Spitsbergen-Comparison of SAR- and Model-estimated wind", Mon. Wea. Rev., 130, 1040-1051, 2002.

Schröter, J., F. Feindt, W. Alpers, and W. C. Keller, "Measurement of the ocean wave-radar modulation transfer function at 4.3 GHz", J. Geophys. Res., vol. 91, pp. 923-932, 1986.

Scoon, A., I. S. Robinson, and P. J. Meadow, "Demonstration of an improved calibration scheme for ERS-1 SAR imagery using scatterometer wind model", Int. J. Remote Sens., vol. 17, pp. 413-418, 1996.

Shimada, M., "Calibration and image quality of JERS-1's SAR Products", J. Remote Sensing Society of Japan, vol. 14, No. 2, 35-46, 1994.

Shimada, M., "Verification processor for SAR calibration and interferometry", Adv. Space Res. vol. 23, No. 8, pp. 1477-1486, 1999.

Sikora, T. D., G. S. Young, H. N. Shirer, and R. D. Chapman, "Estimating convective atmospheric boundary layer depth from microwave radar imagery of the Sea surface", J. Appl. Meteorol., 36, 833-845, 1997.

Small, C., and R. J. Nicholls, "A global analysis of human settlement in coastal zones", J. Coastal Res., 19(3), 2003.

Smith, P. C., and J. I. MacPherson, "Cross-shore variation of near-surface wind velocity and atmospheric turbulence at the land-sea boundary during CASP", Atmos. Ocean, 25, 279-303, 1987.

Smith, R. B. and V. Grubisic, "Aerial observations of Hawaii's wake", J. Atmos. Sci., 50(22), 3728-3750, 1993.

Smith, R. B., "Aerial observations of the Yugoslavian bora", J. Atmos. Sci., 44(2), 269-297, 1987.

Space Engineering Development Co., Ltd., "Evaluation of JERS-1 SAR Data (No. 4)", company report 1995.

Stoffelen, A., and D. Anderson, "Scatterometer data interpretation: Estimation and validation of the transfer function CMOD4", J. Geophys. Res., vol. 102, pp. 5767-5780, 1997.

Stoffelen, Ad, 1998, Scatterometry, Available: http://www.library.uu.nl/digiarchief/dip/diss/01840669/inhoud.htm

Stull, R. B., "An Introduction to Boundary Layer Meteorology", Kluwer Academic, 666 pp, 1988.

Taylor, P. A., and R. J. Lee, "Simple guide-lines for estimating wind speed variations due to small-scale topographic features", Climatol. Bull., 18, 3-32, 1984.

Thompson, T. W., D. E. Weissman, and F. I. Gonzalez, "SEASAT SAR cross-section modulation by surface winds: GOASEX observations", Geophys. Res. Lett., vol. 8, pp. 159-162, 1981.

Thompson, D. R. and R. C. Beal, "Mapping high-resolution wind fields using synthetic aperture radar", The Johns Hopkins Univ. Tech. Dig., vol., 21, pp. 58-67, Jan. 2000.

Ufermann, S., I. S. Robinson, and J. C. B. Da Sliva, "Synergy between synthetic aperture radar and other sensors for the remote sensing of the ocean", Ann.Te'le'commun., 56, n.11-12, pp. 672-681, 2001.

Unal, C. M. H., P. Snoeij, and P. J. F. Swart, "The polarisation-dependent relation between radar backscatter from the ocean surface and surface wind vector at frequencies between 1 and 18 GHz", IEEE Trans. Geosci. Remote Sensing, vol. 29 (4), pp. 621-626, 1986.

Vachon, P. W. and F. W. Dobson, "Validation of wind vector retrieval from ERS-1 SAR images over the ocean", The Global Atmospheric and Ocean System, Vol. 5, pp. 177-187, 1996.

Vachon, P. W., O. M. Johannessen, and J. A. Johannessen, "An ERS-1 synthetic aperture radar image of atomospheric lee waves", J. Geophys. Res., vol. 99, pp. 22, 483-22, 490, 1994.

Vachon, P. W. and F. W. Dobson, "Validation of wind vector retrieval from ERS-1 SAR images over the ocean", The Global Atmospheric and Ocean System, Vol.5, pp. 177-187, 1996.

Vachon, P. W., J. A. Johannessen, and D. P. Brown, "ERS-1 SAR Images of Atomospheric Gravity Waves", IEEE Trans. Geosci. Remote Sensing, vol.33, pp.1014-1025, 1994.

Vacon, T. W., O. M. Johannessen, and J. A. Johannessen, "An ERS-1 synthetic aperture radar image of atmospheric lee waves", J. Geophys. Res., vol. 99, pp. 22, 483-22, 490, 1994.

Van Der Hoven, I., "Power Spectrum of Horizontal Wind Speed in the Frequency Range From 0.007 to 900 Cycles Per Hour", J. Meteorol., Vol. 14, 1957.

Wackerman, C. C., C. L. Rufenach, R. A. Shuchman, J. A. Johannessen, and K. L. Davidson, "Wind Vector Retrieval Using ERS-1 Synthetic Aperture Radar Imagery", IEEE Trans. Geosci. Remote Sensing, vol.34, pp.1343-1352, 1996.

Watabe, I., Y. Fujinawa, S. Iwata, H. Ishidoya, and I. Isozaki, "Oceanographical and meteorological structure of Sagami Bay (Part 1)", Techical note of the national research institute for earth science and disaster prevention, No.170, 1996.

Watabe, I., Y. Fujinawa, S. Iwata, H. Ishidoya, and I. Isozaki, "Oceanographical and meteorological structure of Sagami Bay (Part 2)", Techical note of the national research institute for earth science and disaster prevention, No.177, 1997.

Weissman, D. E., D. B. King, T. W. Thompson, "Relationship between hurricane surface wind and L-band radar backscatter from the sea surface", J. Appl. Meteorol., vol. 18, pp. 1023-1034, 1979.

Wentz, F. J., S. Peteherych, and L. A. Thomas, "A model function for ocean radar cross sections at 14.6 GHz", J. Geophys. Res., vol. 89, pp. 3689-3704, 1984.

Wentz, F. J. and D. K. Smith, "A model function for the ocean-normalized radar cross section at 14 GHz derived from NSCAT observation", J. Geophys. Res., 86, 11,499-11,514, 1999.

Yeh, H.-C., and Y.-L. Chen, "Numerical simulations of the barrier jet over northwestern Taiwan during the Mei-Yu season", Mon. Wea. Rev., 131, 1396-1407, 2003.

Zheng, Q., X.-H. Yan, V. Klemas, C.-R. Ho, N.-J. Kuo, and Z. Wang, "Coastal lee waves on ERS-1 SAR images", J. Geophys. Res., 103, 7979-7993, 1998.